The Superconducting Properties of Niobium-Titanium Alloy Multilayers

A Dissertation
Presented to the Faculty of the Graduate School
of
Yale University
in candidacy for the degree of
Doctor of Philosophy

by
James Drury McCambridge
December, 1995

Disertation Director: Prof. D. E. Prober

Abstract

The Superconducting Properties of Niobium-Titanium Alloy Multilayers

James Drury McCambridge

1995

We fabricated and measured thin film $Nb_{0.37}Ti_{0.63}$/Nb multilayers to examine the roles of composition and geometry in determining the technologically important properties of superconductors: the critical current density and the upper critical field. Some $Nb_{0.37}Ti_{0.63}$/Ti samples were made as well. Individual layer thicknesses were of order the superconducting coherence lengths in NbTi and Nb. The samples were characterized by DC and A C electrical transport between 4.2 K and the critical temperature in magnetic fields up to 6 T. We present the superconducting properties as functions of the device geometry and the angle the applied magnetic field makes with the layers. Samples were also characterized by x-ray diffraction, transmission and scanning electron microscopy, and atomic force microscopy.

For applied fields near parallel with the layers, the upper critical fields showed quasi-two dimensional behavior associated with the well-known 3D-to-2D dimensional crossover of the superconducting order parameter. At these same angles, the critical current densities of many of the multilayers showed strong peak effects versus field in the range 0.2 - 0.5 $H_{c2}(T)$. These peak critical current densities are among the highest achieved in the NbTi system, being 3 - 5 times the magnitude of J_c for conventional heat-processed NbTi wire across the entire field range. We present a model of the competition between the vortex-vortex and vortex-pin interactions which accounts for the qualitative features of this peak effect.

Table of Contents

Acknowledgments

Begin at the beginning...and go on till you come to the end: then stop.
-The Red Queen, Alice's Adventures in Wonderland

I would like to thank the academy...oops, wrong notes. There are so many people who made my journey through graduate school enjoyable and fruitful (uh oh, this is degenerating into cliche), I don't think I can give all the credit where credit is due—I suppose I should begin at the beginning...

Prof. Dan Prober has always encouraged me (and shown the way) to become a better scientist and a clearer thinker (a bit redundant, I admit), as he does all his students. I am deeply indebted to him for the many lessons in the communication of ideas; I hope that someday I'll be able to pass on the knowledge I've gained from him. All the members of ProberLab, past and present, have contributed to this thesis—four stand out as coworkers, teachers, and friends: Rich Steinberg introduced me to the worlds of cryostat construction, sputter deposition, and the Carpenters (for which I'll probably never forgive him). Dr. Sean Ling taught me about vortex dynamics, thermometry, and editing. (He can't be blamed entirely—all opinions expressed in this work are mine.) Nick Rizzo provided moral support. Dr. Jian Wang helped shape my thinking on vortex-pin interactions and the nature of Zen (which is mostly about the cleanliness of one's shirts, apparently). Oh, OK: Nick Rizzo provided much more than moral support. He helped me out every step of the way through sample fabrication and measurement and has consistently given key insights (on demand) into Life, reactive ion etching, and cryostat repair. What am I going to do without Nick to prop me up?

This thesis couldn't have been started (much less completed) without the support and expertise of Dr. Lesh Motowidlo and Bruce Zeitlin at IGC Advanced Superconductors. It was their work and interest which provided the impetus for ours. The help and friendship of the people of Prof. Mark Reed's lab was invaluable: Rachel

Lombardi went out of her way to oxidize Si wafers for me—a favor I will not soon forget. Jeff Sleight and Mandar Deshpande took SEM photos for me and never complained! I also benefited from the considerable AFM skills of Dr. Mark Amman. I am indebted to Dr. Dan Dietderich of LBL and Kenny Faase of OSU who both took their valuable time and skill to prepare TEM photos of a number of multilayer samples. Dr. John Talvacchio of Westinghouse and Yu Lu of Brown made XRD measurements on multilayer samples. I also has the pleasure to work with Preeti Chalsani and Ben Weiss, who wrote the software for the measurement setup. Sam Hess performed above and beyond the call of his Senior Thesis by making a number of measurements for me.

A large number of people conspired to keep me sane during my time at Yale and during the writing of this thesis. There is no particular order to the list which follows.

I shared an office with Curt Richter and Mike Gaidis for almost five years. Curt introduced me to beautiful music I'd never heard before: Frank Zappa, the Mentors, the Residents. Mike provided the rest: good advice on fabrication and a willingness to be the Lesker master. Hodge Worsham and George Ugras taught me everything I know about SIS mixers and Turkish culture. In fact, I was so impressed by Hodge that I am modeling my life on his. (So far, so good.) Stephan Friedrich taught me how to make Manhattans, which certainly make long train rides more bearable. Anurag Mittal always was willing to go out for lunch or lend me helium and usually offered to get me a cup of joe from Willoughby's, even though I don't drink coffee. Peter Burke (a fellow Chicagoan) was always ready to lend DMMs or computer advice, for which I've been very grateful. Finally, Ken Segall had the courage to take over the Lesker. Mazel tov, Ken!

Outside the lab, I had the chemistry department soccer team and the various musical "projects" I was involved in (who can forget the worst bands in New Haven? Rogue Elephant! Log! The Sissies (or was it Bucket?)! Flat Rabbit!) to take my mind off laboratory setbacks. Why the chemistry dept. soccer team? I had to meet the chemistry women! Kitty Howard, in particular, kept me well fed during the writing of this thesis. I

made many good friends playing soccer and bass. Between time out for lost teeth and hearing, I hope Dan wasn't too worried about me.

Before I began this thesis, I spent almost a year working with Drs. John Talvacchio and Martin Forrester at Westinghouse. They served as mentors, advisors, and friends while I was in Pittsburgh learning about High T_c Josephson junctions. Wow, deja vu!

Finally, I would like to thank my parents and family for their love, encouragement, and support (monetary not the least). And not just during graduate school. This thesis is dedicated to the memory of my father, C. Paul McCambridge, Jr.

List of Figures

List of Tables

List of Abbreviations

a	vortex lattice spacing
A	the magnetic vector potential
AC	alternating current
Al	Aluminum
Ag	Silver
a_{Nb}	Nb lattice constant
a_{NbTi}	NbTi lattice constant
APC	artificial pinning center
Ar	Argon
b	reduced magnetic field = B/H_{c2}
	local microscopic field
B	magnetic field
bcc	body-centered cubic crystal structure
BCS	Bardeen-Cooper-Schreiffer
B_{max}	field at maximum pinning force density
B_{min}	onset field of the peak effect
CG	carbon glass resistance thermometer
CPU	central processing unit
Cu	Copper
D_S	electron diffusion constant in a "dirty" superconductor
D_N	electron diffusion constant in a "clean" superconductor
DC	direct current
	District of Columbia
DI	deionized (water)
DMM	digital multimeter

d_{Nb}	Nb layer thickness
d_{NbTi}	$Nb_{0.37}Ti_{0.63}$ layer thickness
d_{Ti}	Ti layer thickness
e	free electron charge
f	elementary pinning force
	free energy density
f_L	elementary pinning force per unit length
F_p	global pinning force density
FSU	former Soviet Union
G	reciprocal lattice vector of crystal
GL	Ginzburg-Landau
H_c	thermodynamic critical field
H_{c2}	upper critical magnetic field
H_{c2D}	critical magnetic field for quasi-2D superconductor
H_{c3}	critical field for surface superconductivity
He	Helium
H^{max}	field at maximum critical current density $\neq B_{max}$
I_c	critical current
I-V	current-voltage characteristic
J_c	critical current density
k	wavevector
k_{BZ}	radius of the circularized Brillouin zone of the vortex lattice
K	normal metal coherence length
KJL	Kurt J. Lesker Company SuperSystem III
ℓ	mean free path
L	vortex length
L_c	longitudinal dimension of the collective volume

LO	Larkin-Ovchinnikov
m	GL effective mass of superconducting condensate parallel to planes
	free electron mass
M	GL effective mass perpendicular to planes
MFF	cleanroom
n	number density of pinners
n_Λ	linear density of pinners of a multilayer = $1/\Lambda$
N	Nitrogen
	number of pinners in collective volume
Nb	Niobium
O	oxygen
OD	outer diameter
Pa	pascal
PID	proportional-integral-differential feedback
PR	photoresist
q	reciprocal lattice vector of ML structure
Q	reciprocal lattice vector
R	resistance
	pinner radius
R_c	transverse dimension of the collective volume
RIE	reactive ion etching
RF	radio frequency
RMS	root mean square
R_n	normal state resistance just above T_c
	i.e. the residual lattice resistance
$\mathbf{r}_\nu$	displaced position of νth vortex core
$\mathbf{R}_\nu$	equilibrium position of νth vortex core

r_p	range of the pinning force
	size of a pinner
rpm	rotations per minute
R_{S-H}	thermal resistance between the sample and the heater
R_{S-T}	thermal resistance between the sample and thermometer
RRR	residual resistance (resistivity) ratio = R(~ 300 K)/R_n
R_{WG}	thermal resistance between the sample and the He bath, through the worm gear mechanism
R_{WL}	thermal resistance between the sample and the He bath, through the weak link
s	magnitude of Bragg scattering vector
SAD	small area electron diffractometry
s_v	displacement of vth vortex from equilibrium position
sccm	standard cubic centimeters per minute
SEM	scanning electron microscopy
SF_6	Sulfur Hexaflouride
SiO_2	Silicon Dioxide
SSC	superconducting supercollider
SVL	stepwise vortex lattice
t	thickness
T	tesla
	temperature
Ta	Tantalum
T_c	critical temperature
TC	thermocouple gauge, vacuum or temperature
TCA	1,1,1-Trichloroethane
TEM	transmission electron microscopy

Ti	Titanium
T_{set}	thermocouple temperature setpoint
T_{sub}	true substrate temperature
TT	Takahashi-Tachiki
TTS	Takahashi-Tachiki-Sunaga
$T_{3D\text{-}2D}$	3D to 2D dimensional crossover temperature
U_{comp}	characteristic uniaxial compression energy of the vortex lattice
U_{line}	the vortex self energy
U_{pin}	characteristic pinning energy
U_{tilt}	characteristic tilt energy of the vortex lattice
U_{shear}	characteristic shear energy of the vortex lattice
v_F	Fermi velocity
V	electron pairing interaction
V_c	collective (or correlated) volume
V_{dc}	DC bias voltage
V_H	Hall voltage
XRD	x-ray diffractometry
Zr	Zirconium
α	first GL coefficient
	hexagonal close packed phase
β	second GL coefficient
γ	electronic specific heat per volume
Γ	ratio of the GL effective masses, out-of-plane to in-plane = $(M/m)^{1/2}$
Δ	pair potential
ΔT_c	transition width
ε_1	vortex self-energy

θ	angle between sample planes and field
	angle between sample stage and cryostat axis
	1/2 Bragg scattering angle
κ	GL parameter = λ/ξ
λ	magnetic penetration depth
	wavelength
Λ	multilayer wavelength or period
μ	x-ray absorption constant
ξ	GL coherence length
ξ_0	BCS coherence length
ρ_n	normal state resistivity
ϕ	angle between the transport current and applied field
ψ	Ginzburg-Landau order parameter
ψ_∞	maximum value of GL order parameter
Ψ	normalized GL order parameter = ψ/ψ_∞

Chapter 1. Introduction

In this thesis, our goal has been to better understand the basic mechanisms which determine the critical current density J_c (the highest current density which may be passed without dissipation) of technologically important superconductors. By technologically important, we mean those superconducting materials, structures, and conditions that may be useful in large-scale applications [see Larbalestier (93), Collings (83)], such as electromagnets and power generation and storage. One of the external conditions which determines J_c is the applied magnetic field B [Larkin (79), Campbell (72)]. An applied field penetrates a technological superconductor only in small regions called vortices or fluxons (because they carry a quanta of flux) [Abrikosov (59)]. It is the motion of these vortices under applied currents which determines J_c in a magnetic field [Campbell (72)]. To understand the factors which determine J_c, we must understand how the behavior of the vortices is influenced by materials, structure, temperature, and field. This is termed the flux pinning problem: to stop vortex motion, they must be "pinned down" by inhomogeneities in the superconductor.

Other superconducting properties are of interest as well: the upper critical field H_{c2} is the highest magnetic field in which superconductivity exists in the interior of the sample at a given temperature. (Occasionally, a surface sheath of superconductivity can exist to an even higher field H_{c3} [Saint-James (63)], but we have taken steps to minimize this effect in our samples.) One would like a large value of H_{c2} for most applications—therefore, it is necessary to know the effect intrinsic materials properties and external conditions have on the upper critical field.

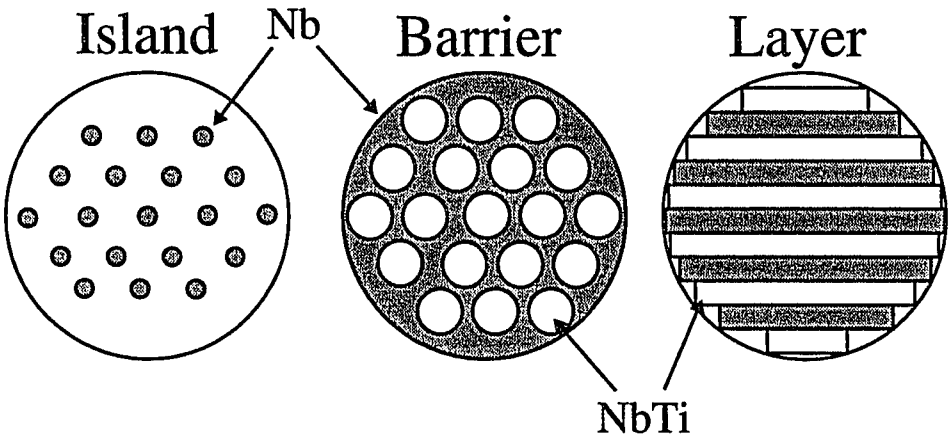

Fig. 1.1. Artificial Pinning Center wires. Each picture represents a single filament in the conductor (diameter ~ 5 μm). Typical conductors have ~ 10 000 filaments. Shaded regions are Nb, unshaded regions are NbTi alloy.

1.1. Artificial Pinning Center Conductors

Our interest was motivated initially by work on NbTi artificial pinning center (APC) wires [Matsumoto (94), Cooley (93), Motowidlo (92), Dorofejev (85)], in which second-phase pinning sites are introduced into the NbTi matrix before drawing (see Fig. 1.1.). In conventionally processed wires [Meingast (89b, 89a)], pinning centers are produced by heat treatments of the wire which cause α-Ti to precipitate out of the matrix. These precipitates are randomly distributed and have a maximum volume density of ~ 25% [Meingast (89a)]. The APC approach has four distinct advantages. The first is no heat treatments are needed to produce wires with strong pinning [Motowidlo (90)], which translates into lower processing costs. Second, the pinner material is no longer limited to Ti, but can be any material metallurgically compatible with NbTi [Motowidlo (92), Matsumoto (92)]. Third, the microstructure of the conductor can be designed and modified at will [Motowidlo (90)]. Fourth, there is no limit on the amount of pinner material which may be incorporated into the design, other than that imposed by the depression of system-wide superconducting properties by the proximity effect

[Motowidlo (92), Meingast (87), deGennes (64)]. The last three advantages can all lead to higher critical current densities than can be achieved by the conventional heat treatment process and that is why the interest in APC conductors is so great. This is not to say that the understanding of pinner material, structure, and density are not important in conventional superconducting wires.

1.2. Multilayers

To investigate these last issues for higher critical current densities, we have studied the properties of layered thin film structures of the superconductors Nb and $Nb_{0.37}Ti_{0.63}$. Additional multilayer samples composed of Ti and $Nb_{0.37}Ti_{0.63}$ were also fabricated, but time constraints prevented their full characterization. The data on the $Nb_{0.37}Ti_{0.63}$/Ti multilayers is presented in Appendix D. It was our hope that we could gain insight into the flux pinning problem and propose new directions for wire makers by using multilayers to model the structural and material variations typically found in superconducting wires. It is these variations which create the pinning potential for vortices.

Superconducting multilayers, by which we mean a thin film structure composed of at least one metallic superconductor, have long been used to study the nature of superconductivity on small length scales comparable to the superconducting coherence length. Much of the interest in multilayers springs out of the long-standing interests in the behavior of anisotropic superconductors, both naturally occurring (like the layered dichalcogenides [Beasley (80)] and high-temperature oxides [Iye (89)]) and artificially fabricated [Jin (89)]. These anisotropies are usually manifested in both H_{c2} [Ruggiero (80)] and J_c [Raffy (72)]—the behavior of the system strongly depends on the orientation of the applied field relative to the layers. The primary interests in layered materials have been in the dimensionality of superconductivity and its effect on the upper critical fields

[Takahashi (86b, 86a), Klemm (75)] and recently, as model systems for the behavior of high-T_c compounds [Koshelev (93), White (91), Neerinck (91), Koorevaar (90)].

There has been comparatively little work on the flux pinning properties of layered superconductors until recently [Koorevaar (93), Nojima (93)], with the exception of the work of Raffy and coworkers throughout the 1970s [Raffy (81, 74b, 74a, 72)]. Even so, the work on flux pinning in these studies was used primarily as a tool to study the dimensionality of layered superconductors. Our work is the first to explicitly concentrate on the issues of materials and structure important for technological applications.

1.3. Organization of the Thesis

We divide the rest of this thesis into 5 chapters. Chapter 2 provides the basic theoretical groundwork to understand the Ginzburg-Landau theory [Ginzburg (50)], which we have used (to a large extent) to interpret our data. We cover the influence of both vortex-pin and vortex-vortex interactions. Chapter 3 deals with the fabrication and measurement of $Nb/Nb_{0.37}Ti_{0.63}$ multilayers, including the cryostat and measurement apparatus. We present our results on the basic superconducting properties in chapter 4, concentrating on H_{c2} when the applied field is nearly parallel to the layers. In chapter 5, we present our measurements of the flux pinning properties of our multilayers—we observe a surprisingly strong peak effect in the pinning forces in near parallel fields whose onset occurs around ~ 0.2 H_{c2} and whose maximum occurs near ~ 0.4 H_{c2}. We explain this peak effect as arising from the competition between the elastic forces of vortex-vortex repulsion and the strong pinning forces of the layering. Finally, in chapter 6, we summarize our results and give our conclusions for this work. Four appendices dealing with the fabrication procedures, sample parameters, sample temperature corrections, and the measurements on the $Nb_{0.37}Ti_{0.63}/Ti$ multilayers follow the conclusions.

Chapter 2. Ginzburg-Landau Theory

In this chapter, we will provide a brief overview of the theoretical tools we need to understand and explain our results. We will concentrate on the Ginzburg-Landau (GL) theory of superconductivity [Ginzburg (50)], which is exact near the superconducting-to-normal phase transition ($T \rightarrow T_c$) [Gor'kov (60, 59)] and provides semi-quantitative results even far below T_c [e.g., Brandt (77b)]. Although more accurate microscopic models of superconductivity exist (e.g., the Bardeen-Cooper-Schreiffer (BCS) theory [Bardeen (57)]), they are not as intuitive or as easily calculated as the GL results. The power of the GL theory lies in its ability to more easily treat the macroscopic behaviors of superconductors when the free energies, and not the elementary excitations, are the most important factor [Tinkham (80)].

We will divide this chapter into three parts: the basics of GL theory [for a good treatment see Tinkham (80)]; the interactions of a vortex (also called a fluxon, flux-line, etc.) with inhomogeneities in the superconducting properties (which are called pinning centers, pinners, etc.); and the interactions between vortices.

2.1. The GL Free Energy

Near the superconducting-to-normal transition, we may expand the free energy of the system, the sum of the free energy due to the normal components and to the superconducting components (which we know from the microscopic theory [Bardeen (57)] are paired electrons), as

$$f = f_{n0} + \alpha|\psi|^2 + \frac{1}{2}\beta|\psi|^4 + \frac{1}{2m}\left|\left(i\hbar\nabla + 2e\vec{A}\right)\psi\right|^2 + \frac{b^2}{2\mu_0}. \qquad (2.1.)$$

In Eq. 2.1. f_{n0} is the free energy density of the normal state, ψ is the complex order parameter, $|\psi|^2$ is interpreted as the density of superconducting pairs, α and β are temperature-dependent coefficients determined by the microscopic properties of the material, m and e are the free electron mass and charge, and b is the local magnetic field. ψ is assumed to be small and slowly varying in space.

In the absence of applied fields and currents, the free energy difference between the superconducting and normal state is

$$f_s - f_n = \alpha|\psi|^2 + \frac{1}{2}\beta|\psi|^4 = -\frac{H_c^2}{2\mu_0} = \alpha|\psi_\infty|^2, \tag{2.2.}$$

where we have used the definition of the thermodynamic critical field H_C. The free energy difference has a maximum when $|\psi|^2 = -\alpha/\beta \equiv |\psi_\infty|^2$. ψ_∞ is the value the order parameter attains in the absence of fields and currents, far away from any disturbance. In the presence of applied fields and currents, we must use Eq. 2.1. and minimize the total free energy of the system. This leads to the GL differential equations.

2.2. The GL Differential Equations

Minimization of the free energy with respect to ψ^* gives the first GL differential equation:

$$\alpha\psi + \beta|\psi|^2\psi + \frac{1}{2m}\left(i\hbar\nabla + 2e\vec{A}\right)^2\psi = 0. \tag{2.3.}$$

This is a Schrödinger-like equation for the order parameter. When we minimize with respect to A, we obtain the second GL differential equation:

$$\vec{J}_s = \frac{i\hbar e}{2m}\left(\psi\nabla\psi^* - \psi^*\nabla\psi\right) - \frac{2e}{m}|\psi|^2\vec{A}\ . \tag{2.4.}$$

This is the familiar quantum mechanical expression for the current for a state with eigenfunction ψ.

2.2.1. GL Coherence Length and Magnetic Penetration Depth

There are two important length scales in the GL theory: the temperature dependent coherence length ξ and the magnetic penetration depth λ. The coherence length comes from a consideration of the first GL differential equation. In the absence of an applied field, Eq. 2.3. can be rewritten:

$$\frac{\nabla^2}{\xi^2}\Psi + \Psi - |\Psi|^2\Psi = 0, \tag{2.5.}$$

where $\Psi = \psi/\psi_\infty$. It is clear that ξ is the characteristic length over which the order parameter Ψ varies. It is equal to

$$\xi^2 = \frac{\hbar^2}{2m|\alpha(T)|} = 0.73\frac{\xi_0 \ell}{T_c - T}, \tag{2.6.}$$

where we have used Gor'kov's [60, 59] results from the microscopic theory to relate the GL coherence length to the BCS coherence length ξ_0 in the dirty limit (the mean free path $\ell \ll \xi_0$).

The magnetic penetration depth follows from the second GL equation and Maxwell's equations. In the presence of very weak magnetic fields, we can neglect the gradient term in Eq. 2.4. Using Maxwell's equation $\boldsymbol{J} = \nabla \times \boldsymbol{H}$ and combining it with the second GL equation we find that

$$\begin{aligned} \lambda^2 \nabla^2 \vec{b} &= \vec{b} \\ \lambda^2 &= \frac{m}{2e\mu_0|\psi|^2}. \end{aligned} \tag{2.7.}$$

That is, an applied magnetic field is screened out of a superconductor on the length scale λ. The ratio of the magnetic penetration depth to the GL coherence length λ/ξ is often called the GL parameter κ. It is a convenient number, which is approximately temperature independent, by which we can characterize the electrodynamic response of a superconductor. Superconductors of technological interest are type II superconductors with $\kappa \gg 1$ (as distinguished from type I superconductors, with $\kappa \leq 1/\sqrt{2}$).

We now have the fundamental tools to address the problem of vortex pinning in superconductors. Boundary conditions can be applied to Eqs. 2.3. and 2.4. and they can be solved self-consistently to obtain the full behavior of a superconducting system with applied fields and currents.

2.3. The Upper Critical Field of a Bulk Superconductor

As an example of the use of the GL equations, we will now calculate the upper critical field of a bulk superconductor H_{c2}. In a type II material, H_{c2} is the highest field for which ψ is nonzero throughout the sample. The lower critical field H_{c1} is the highest field which is screened out of the interior of the sample (the Meissner state). Between H_{c1} and H_{c2}, the magnetic field penetrates the sample. This is in contrast with a type I superconductor which is simply characterized by the thermodynamic critical field: below H_c, the magnetic field is completely excluded from the interior of the sample; above H_c, the sample is nonsuperconducting.

Near the upper critical field $\Psi \ll 1$ and we may neglect the cubic term in Eq. 2.3. Let us consider a field applied along the z axis: we choose the gauge $A_y = Bx$. The first GL equation then becomes:

$$\left(i\nabla + \frac{\pi\vec{A}}{\Phi_0}\right)^2 \psi = \left[-\nabla^2 + \frac{2\pi i}{\Phi_0} Hx\frac{\partial}{\partial y} + \left(\frac{\pi B}{\Phi_0}\right)^2 x^2\right]\psi = \frac{1}{\xi^2}\psi, \qquad (2.8.)$$

where Φ_0 = h/2e is the magnetic flux quantum. Eq. 2.8. can be recast in the form of the Schrödinger Equation for a one-dimensional simple harmonic oscillator. When we equate the known SHO eigenvalues to the operator on the right side of Eq. 2.8. we obtain an equation for the upper critical field:

$$B = \frac{\Phi_0}{2\pi(2n+1)}\left(\frac{1}{\xi^2} - k_z\right), \tag{2.9.}$$

where k_z is the wavevector of the plane wave solution along the z axis. B is maximized by choosing $k_z = n = 0$. We find the well-known GL result for the bulk upper critical field:

$$H_{c2}(T) = \frac{\Phi_0}{2\pi\xi^2(T)}. \tag{2.10.}$$

2.4. The Abrikosov Vortex Lattice

Magnetic flux will penetrate a type II superconductor ($\kappa > 1/\sqrt{2}$) above H_{c1}. The flux does not penetrate uniformly, however, since the majority of the sample is still superconducting. The magnetic field is incorporated a single flux quantum Φ_0 at a time, each of which is surrounded by a vortex of shielding currents. The reason behind this behavior is that the domain wall energy (between the superconducting and normal phases) goes from positive to negative at $\kappa = 1/\sqrt{2}$. Therefore, in a type II superconductor, it is energetically favorable to maximize the domain wall area by splitting up the normal region into many smaller regions containing Φ_0 apiece. Abrikosov [57] was the first to show, using the GL equations, that the magnetic field penetrates a type II superconductor as a lattice of vortices (also called fluxons or flux-lines). In a homogeneous superconductor, the vortex lattice is triangular, which maximizes the nearest neighbor distance and therefore minimizes the energy, with a unit cell determined by the applied field. The vortex lattice spacing $a \approx (\Phi_0/B)^{1/2}$.

2.4.1. The Structure of an Isolated Vortex

The GL equations can be solved to understand the behavior of the superconducting order parameter and the magnetic fields in the vicinity of a vortex. Ψ is zero at the center of a vortex, but rises to near unity within 2ξ. If we consider an extreme type II superconductor ($\kappa \gg 1$), we can make the approximation that outside the normal "core" (radius ~ ξ) the magnitude of $\psi \approx \psi_\infty$. With this approximation, we can use Eq. 2.7., modified to account for the core, to obtain an analytical result for the magnetic field of an isolated vortex [Tinkham (80)]:

$$\vec{b}(\vec{r}) = \hat{z}\frac{\Phi_0}{2\pi\lambda^2}K_0\left(\frac{r}{\lambda}\right), \tag{2.11.}$$

where K_0 is the modified Bessel function of zeroth-order. We illustrate the order parameter and the field of an isolated vortex in Fig. 2.1.

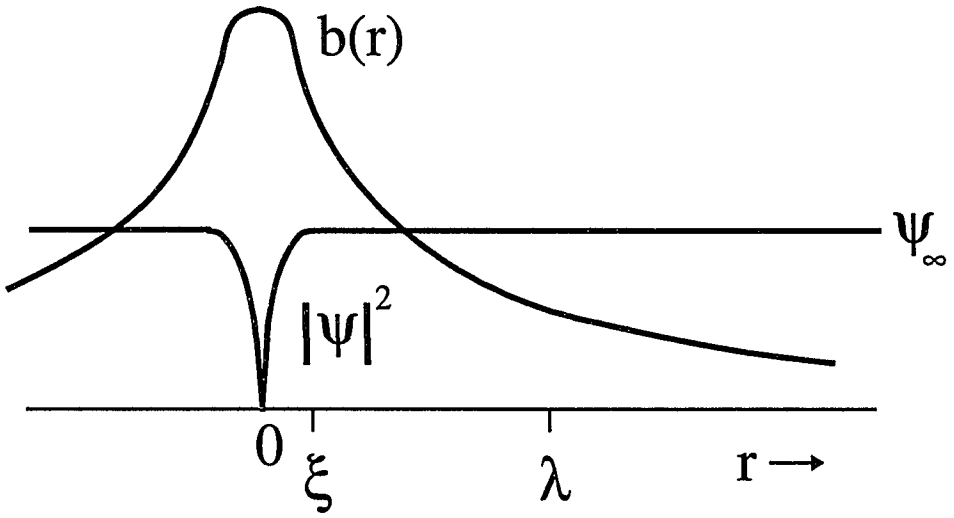

Fig. 2.1. The structure of an isolated vortex in a type II superconductor, for $\kappa \sim 7$. The vortex core has a radius ~ ξ. The field falls exponentially far away from the vortex core. Adapted from [Tinkham (80)].

2.4.2. Interactions Between Vortices

The free energy per unit length of a vortex (or line tension) has two terms—the magnetic field energy and the kinetic energy of the screening currents:

$$\varepsilon_1 = \int_S \left(\frac{b^2}{2\mu_0} + \frac{1}{2}\lambda^2 (\nabla \times b)^2 \right) dS. \tag{2.12.}$$

The expression above can be used to evaluate the self-energy of a single vortex by plugging in Eq. 2.11. The energy of interaction between n vortices can be found by using the superposed fields of the individual vortices:

$$\vec{b}(\vec{r}) = \hat{z} \frac{\Phi_0}{2\pi\lambda^2} \sum_j K_0 \left(\frac{|\vec{r} - \vec{r}_j|}{\lambda} \right) \tag{2.13.}$$

and evaluating Eq. 2.12. When this is done, the free energy per unit volume of n vortices is found to be [Van Duzer (81)]

$$\Delta f = n\varepsilon_1 + \frac{n\Phi_0^2}{4\pi\mu_0\lambda^2} \sum_j K_0 \left(\frac{|\vec{r} - \vec{r}_j|}{\lambda} \right), \tag{2.14.}$$

where the first term is simply the self-energy of the individual vortices and the second term is the energy of interaction between them. The interaction energy is repulsive when two vortices have the same chirality, as is the usual case. The force per unit length on a particular vortex can be obtained by taking the gradient of Eq. 2.14. and using Maxwell's equation curl $\boldsymbol{h} = \boldsymbol{J}$:

$$\vec{f} = \vec{J}_s \times \vec{\Phi}_0, \tag{2.15.}$$

where $\boldsymbol{J_s}$ is the total supercurrent (from other vortices and any transport current) at the center of the fluxon and Φ_0 is directed parallel to the core. The interactions between vortices can be treated in the theory of elastic media, which we discuss later.

2.5. Flux Pinning: Vortex-Pin Interactions

We have discussed the formation of vortices in type II superconductors and some of the forces upon them. Now we turn our attention to the consequences: How much transport current can pass through a superconductor without dissipation? This is the most important question for technological applications. From Eq. 2.15., we know that if we apply a current density $\boldsymbol{J}$ to a superconductor in a field $\boldsymbol{B}$, the Lorentz force per unit length on each vortex is $\boldsymbol{F_L} = \boldsymbol{J} \times \Phi_0$. The total force density is $\boldsymbol{F_L} = \boldsymbol{J} \times \boldsymbol{B}$. If there is no opposing force, the vortices move under the application of this force. The motion of vortices gives rise to an electric field (dissipation): $\boldsymbol{E} = \boldsymbol{B} \times \boldsymbol{v}$, with $\boldsymbol{v}$ the velocity. We conclude that unless there is some way to stop vortex motion in a material, we cannot carry *any* dissipationless transport current in a magnetic field.

In any real sample, we observe a finite critical current for applied fields $< H_{c2}$. Inhomogeneities in the superconducting properties form pinning centers (because they "pin down" vortices) which exert a restoring force on nearby vortices. The pinning force density can be defined in a straightforward manner—we equate the Lorentz force density at the measured critical current density with the force density with which the vortex lattice is pinned, i.e., $\boldsymbol{F_p} = \boldsymbol{J_c} \times \boldsymbol{B}$.

2.5.1. Elementary Pinning Force of a Void

Let us consider the interaction of an isolated vortex with a void in the superconductor. We can see how a pinning force arises by comparing the free energy of the system as a function of the vortex position. This is shown in Fig. 2.2. When a material is in the superconducting state, its free energy density is lower than that of the normal state by the condensation energy density $H_c^2/(2\mu_0)$ (see Eq.2.2.). If we now add a vortex to the system, we raise the total free energy by destroying superconductivity in the region of the core and adding the line tension of the vortex. In the extreme type II limit ($k \gg 1$),

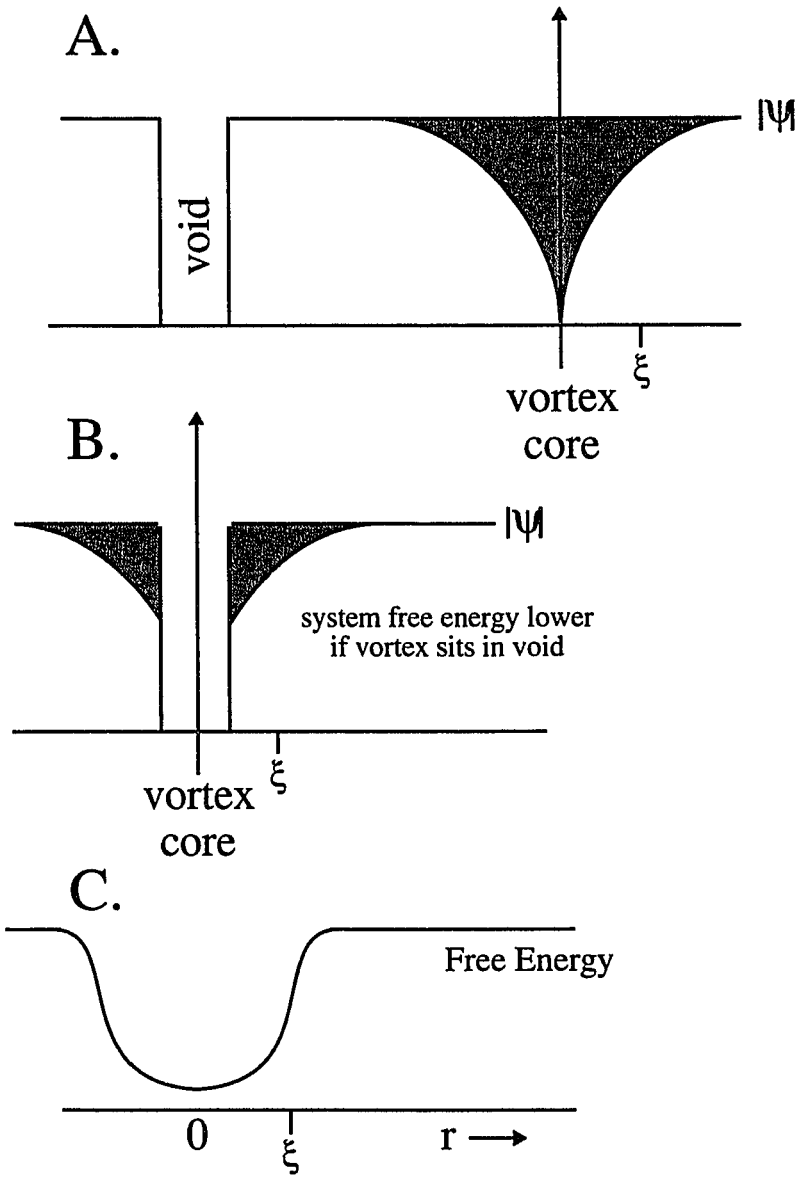

Fig. 2.2. The interaction of a vortex with an inhomgeneity, in this case, a void. A) When the vortex core does not sit in the void, a large amount of superconducting condensation energy is lost (shaded volume). B) When the vortex sits on the pin, the total condensation energy lost is lower, hence there is a potential well in the region of the void, illustrated schematically in C).

we can approximate the line tension using Eq. 2.13. in Eq. 2.12. We can also, in this limit, approximate the condensation energy lost in the vortex core by assuming that within a radius ξ, the order parameter is zero. Outside that radius, ψ has its unperturbed value. Consider the situation in Fig. 2.2.a.: when the vortex is located deep inside the superconductor away from the void, the system energy (relative to the zero field case) is higher by the condensation energy lost and the line tension of the vortex ~ $\pi\xi^2 LH_c^2/(2\mu_0)$ + $\varepsilon_1 L$, where L is the length of the vortex. If we move the vortex so that it sits on top of the void (in Fig. 2.2.b.), the energy (relative to the zero field case) is ~ $\pi\xi^2 LH_c^2/(2\mu_0)$ + $\varepsilon_1 L$ - $\pi R^2 LH_c^2/(2\mu_0)$. The difference between the vortex sitting in the void or deep in the superconductor is ~ $\pi R^2 LH_c^2/(2\mu_0)$, where R is the radius of the void. The attractive pinning force of a void comes about from this free energy difference. The elementary pinning force between a void and the vortex is

$$f \approx \frac{H_c^2}{2\mu_0} \cdot \frac{V_{pin}}{\xi} = \frac{H_c^2}{2\mu_0} \frac{\pi R^2 L}{\xi}, \qquad (2.16.)$$

where we have divided the free energy difference by the length over which that variation takes place ~ ξ. When $R < \xi$, the effective volume of the pinning center $V_{pin} \approx \pi R^2 L$. When $R > \xi$, $V_{pin} \approx \pi\xi^2 L$. Eq. 2.16. describes the so-called core pinning force; we have neglected any free energy contributions from the screening currents associated with the vortex. This is an oft made assumption [Stejic (93), Takahashi (93), Matsushita (83), Kramer (80)] because it simplifies the mathematics and because more exact calculations show that core pinning is the dominant contribution in superconductors with $\kappa \gg 1$ [Takahashi (93)].

2.5.2. General Elementary Pinning Force Calculations

The method outlined above for finding the interaction between a vortex and a void may be generalized to finding the interaction between a vortex and any nonuniformity in

material parameters which creates a change in the superconducting order parameter: grain boundaries [Stejic (93)], point defects [Thuneberg (84, 82)], normal metal inclusions [Stejic (93), Stejic (92), Matsushita (83), Kramer (80)], even weaker superconductors [Stejic (93)]. Given any inhomogeneity, we can find the elementary pinning force by solving the first GL equation (Eq. 2.2.) as a functional of the position of the vortex and plugging the solution into the GL expression for the free energy of a superconductor (Eq. 2.1.). By taking the gradient of the free energy, we obtain the pinning force on the vortex. This is illustrated in Fig. 2.2.c., where we have drawn schematically the pinning potential due to the variation of the free energy as a function of the vortex position for the superconductor-void system.

In the case of a normal metal inclusion, either a nonsuperconductor or a superconductor above its transition temperature, the elementary pinning force may be *higher* than that of a void for inclusions on the order of or smaller than ξ [Matsushita (83)]. This arises because there is a free energy penalty to induce superconductivity into a material which is not normally superconducting (this phenomenon is called the proximity effect). When a vortex sits away from the small inclusion the free energy (relative to zero field) is $\sim \pi\xi^2 L H_c^2/(2\mu_0) + \varepsilon_l L + E_{prox}$, where E_{prox} is the energy cost to induce superconductivity in the normal metal. When the vortex sits in the inclusion, the system energy is $\sim \pi\xi^2 L H_c^2/(2\mu_0) + \varepsilon_l L - V_n H_c^2/(2\mu_0)$, where V_n is the normal metal inclusion effective volume and the proximity effect energy penalty is gone. Hence, the free energy difference is the normal void-like factor $V_n H_c^2/(2\mu_0)$ *plus* E_{prox}, which means the pinning potential is deeper than that of a void of equivalent size.

In the case of a weaker (a vaguely defined term) superconducting inclusion [Stejic (93), Takahashi (93), Tachiki (89a), Mrktchyan (73)], the pinning force can be *higher* or *lower* than that of a void; the two main terms we have used to simplify the energetics of a vortex near an inclusion—the condensation energy and the line tension—both depend on

the specific superconducting properties (ξ and λ) of the inclusion. This topic is of primary importance to this work and is discussed at greater length in Ch. 5.2.1.1.

2.6. Flux Pinning: Vortex-Vortex Interactions

In the flux pinning problem, we must not only consider the interaction of the vortex lattice with the pins, but also the interactions between vortices. Vortex-vortex interactions are often modeled using local elasticity theory [Brandt (77a)]. That is, the free energy increase of distorting the vortex lattice from its equilibrium position is calculated using the harmonic approximation—Hooke's Law. If the equilibrium positions of the zeroes of ψ (the positions of the vortex cores) are located at $\boldsymbol{R}_\nu = (X_\nu; Y_\nu; z)$, where the ν index each vortex, we may write the displacement field of the vortex lattice as [Brandt (77a)]:

$$\vec{s}_\nu(z) \equiv \vec{r}_\nu(z) - \vec{R}_\nu, \tag{2.17.}$$

where $\boldsymbol{r}_\nu(z) = (x_\nu(z); y_\nu(z); z)$ are the positions of the vortex cores of the deformed vortex lattice. The free energy increase for this deformation field (see Eq. 2.14.) may be written [see Feigel'man (89)]:

$$\Delta F = \sum_\nu \int dz \left[(c_{11} - c_{66}) \frac{\left(\nabla \cdot \vec{s}_\nu(z)\right)^2}{2} + c_{66} \frac{\left(\nabla_{xy} \vec{s}_\nu(z)\right)^2}{2} + c_{44} \frac{\left(\partial \vec{s}_\nu(z)/\partial z\right)^2}{2} \right], \tag{2.18.}$$

where c_{11}, c_{66}, and c_{44} are the elastic moduli of uniaxial compression, shear, and tilt respectively and ∇_{xy} is the two-dimensional gradient operator. The above holds true only if the superconducting properties are isotropic—with cubic symmetry, only three moduli are needed to describe the response of the vortex lattice to deformation. If the superconductor is anisotropic, other terms will need to be included in Eq. 2.18. [Sudbø (91), Kogan (89)]. The elastic moduli can be found by expanding Eq. 2.14. for the free energy density in a power series with respect to the s_ν [Brandt (77b)]. Brandt [86b] gives

the results of these calculations for the elastic moduli in isotropic type II superconductors for $(2\kappa)^{-1}<B/H_{c2}<1$:

$$c_{66} \approx \frac{H_{c2}^2}{\mu_0}\frac{b(1-b)^2}{8\kappa^2}\left(1-\frac{1}{2\kappa^2}\right)\left(1-0.58b+0.29b^2\right)$$
$$c_{11}(k) = \frac{B^2}{\mu_0}\left(1-\frac{1}{2\kappa^2}\right)\frac{1}{1+(k\lambda')^2}\frac{1}{1+(k\xi')^2} \quad , \qquad (2.19.)$$
$$c_{44}(k) = \frac{B^2}{\mu_0}\left[\frac{1}{1+(k\lambda')^2}+\frac{1}{(k_{BZ}\lambda')^2}\right]$$

where $b = B/H_{c2}$, $\lambda' = \lambda/(1-b)^{1/2}$, $\xi' = \xi/(2-2b)^{1/2}$, and $k_{BZ} = (2b)^{1/2}/\xi$. The above results reflect the strong nonlocality of the elastic moduli when the distortion wavelength is smaller than the effective penetration depth λ'—the energy cost for deformation ~ B^2 is lowered since the magnetic field of the vortices cannot change on length scales much below λ'.

2.7. Flux Pinning: The Summation Problem

Now that we can describe the forces on the vortex lattice, we must discuss the methods for adding up the individual forces from vortex-pin and vortex-vortex interactions to obtain the total pinning force. This is termed the summation problem. In general terms, there are only two situations we need to concern ourselves with: the case where the pinning forces are much greater than the elastic forces and the case where they are not. However, the pinning forces and elastic forces depend on the applied field—there may be regimes where the behavior of the system crosses over between the two cases.

2.7.1. Direct Summation or Single Particle Pinning

When the pinning forces on the vortex lattice are much greater than the elastic restoring forces, the summation of the individual forces is straightforward: we ignore the vortex-vortex interactions and write the total pinning force density [Campbell (72)]:

$$F_p = \sum_m f_m \rightarrow nf. \qquad (2.20.)$$

In the simplest case, where all the pinning centers have the same strength, we have indicated that the total pinning force density is simply n, the number density of pinners, times the elementary pinning force f.

2.7.2. Collective Pinning

When the elastic forces are comparable to or larger than the pinning forces, the summation of the individual forces is more complicated. Larkin and Ovchinnikov [79] proposed a scheme of statistical summation to account for the interactions between vortices which they called collective pinning. Since their original paper, many authors have extended and tested the concept of collective pinning [Wördenweber (90), Feigel'man (89), Mullock (85), Kes (81)].

If the elastic forces are strong, the vortex lattice is said to be stiff or rigid. This rigidity will prevent the vortex lattice from deforming appreciably in the region of an inhomogeneity. In the strong pinning, direct summation case, the vortex lattice is soft and easily deformed—indeed, it need not be a "lattice" since the periodic order of the Abrikosov solution is destroyed, though the average density of vortices still remains ~ Φ_0/B. In collective pinning, the ordering of the vortex lattice persists over some volume, V_c. Because of the deformation caused by pinning centers, there is no long-range order. However, for very weak pinning or very strong elastic forces, the correlated volume V_c may include many (> 500) vortices.

In this picture, each collective volume V_c is pinned independently of the others. Because the pinning is assumed to be random and within V_c the vortex lattice is almost unperturbed, the pinning force density on the vortex lattice is

$$F_p = \frac{N^{1/2} f}{V_c} = \sqrt{\frac{nf^2}{V_c}}, \tag{2.21.}$$

where N is the number of pinners within the volume V_c and we have assumed for simplicity that the pinners each have the same elementary pinning force. To clarify the physics underlying Eq. 2.21., consider what happens when a transport current less than the critical current is applied. Each correlated volume experiences a Lorentz force from the transport current. Because the N pinners are distributed randomly, it is just as likely (on average) that the Nth pinner is pushing the vortices around it in the direction of the Lorentz force as it is pulling them against the Lorentz force. Therefore, we must use the fluctuations in the number of pinners per collective volume ~ $N^{1/2}$ to arrive at the global pinning force density.

The size of the collective volume is determined by the interplay of the elastic forces and the pinning forces. Larkin and Ovchinnikov assumed that the boundaries of the collective volumes are shifted relative to one another by a distance of order the vortex lattice spacing a and estimated the free energy density change caused by the inhomogeneities relative to the undeformed vortex lattice as

$$\delta f = c_{66}\left(\frac{a}{R_c}\right)^2 + c_{44}\left(\frac{a}{L_c}\right)^2 - \frac{faN^{1/2}}{V_c}, \tag{2.22.}$$

where R_c and L_c are the Larkin lengths perpendicular and along the field ($V_c = R_c^2 L_c$) and the c_{11} term of the elastic energy was omitted since it is in general much higher than c_{44} or c_{66}. The volume over which there is short range order is found by minimization of Eq. 2.22. with respect to R_c and L_c:

$$R_c = \frac{a^2\sqrt{32c_{66}^3 c_{44}}}{nf^2}$$
$$L_c = \frac{8a^4 c_{66} c_{44}}{nf^2} \quad . \qquad (2.23.)$$
$$V_c = \frac{256a^6 c_{66}^4 c_{44}^2}{n^3 f^6}$$

Although the collective pinning theory was proposed for superconductors with weak pinning, it has been shown experimentally [Ling (95), Stejic (94)] and theoretically [Koshelev (93), Brandt (86a), Mullock (85)] that some systems which undergo plastic distortions (strong pinning $\rightarrow R_c < a$) can be described, at least quantitatively, in the collective pinning picture.

Chapter 3. Experimental Methods

This chapter details the fabrication and measurement of single films and multilayers (MLs) of Nb and $Nb_{0.37}Ti_{0.63}$. All the samples presented in this thesis were made in the Micro Fabrication Facility (MMF) at Yale. The transport measurements were carried out at Yale. The more specialized sample characterizations, like transmission electron microscopy (TEM) and x-ray diffractometry (XRD), were done elsewhere. This chapter is divided into two main sections: the deposition and patterning of the thin film devices and their measurement.

3.1. Sputter Deposition of Nb and $Nb_{0.37}Ti_{0.63}$

Our thin films were sputter-deposited using Torus 2C magnetron guns in a Kurt J. Lesker Co. SuperSystem III sputtering machine (KJL) [see Steinberg (92)], which located in the MFF (schematic shown in Fig. 3.1.). Sputtering is a method of physical vapor deposition [Chapman (80)]. The material to be deposited (the target) is placed at a high potential (RF or DC) relative to ground. A low pressure of gas is introduced into the vacuum chamber (typically 10 to 20 mTorr Ar, research grade 99.999% purity), which spontaneously ionizes in the field. The ions then accelerate toward the target. If conditions are favorable, a self-sustaining plasma is formed. The accelerated gas molecules bombard the target, knocking off atoms. Usually these are single, neutral atoms, but occasionally small clusters or ions are ejected [Chapman (80)]. All this is shown in Fig. 3.2. Sputtering has a number of advantages over evaporation, the chief of which is the ability to deposit high-melting-temperature materials (like Nb and Ti) easily. The target need not be conductive either, if an AC power supply is used.

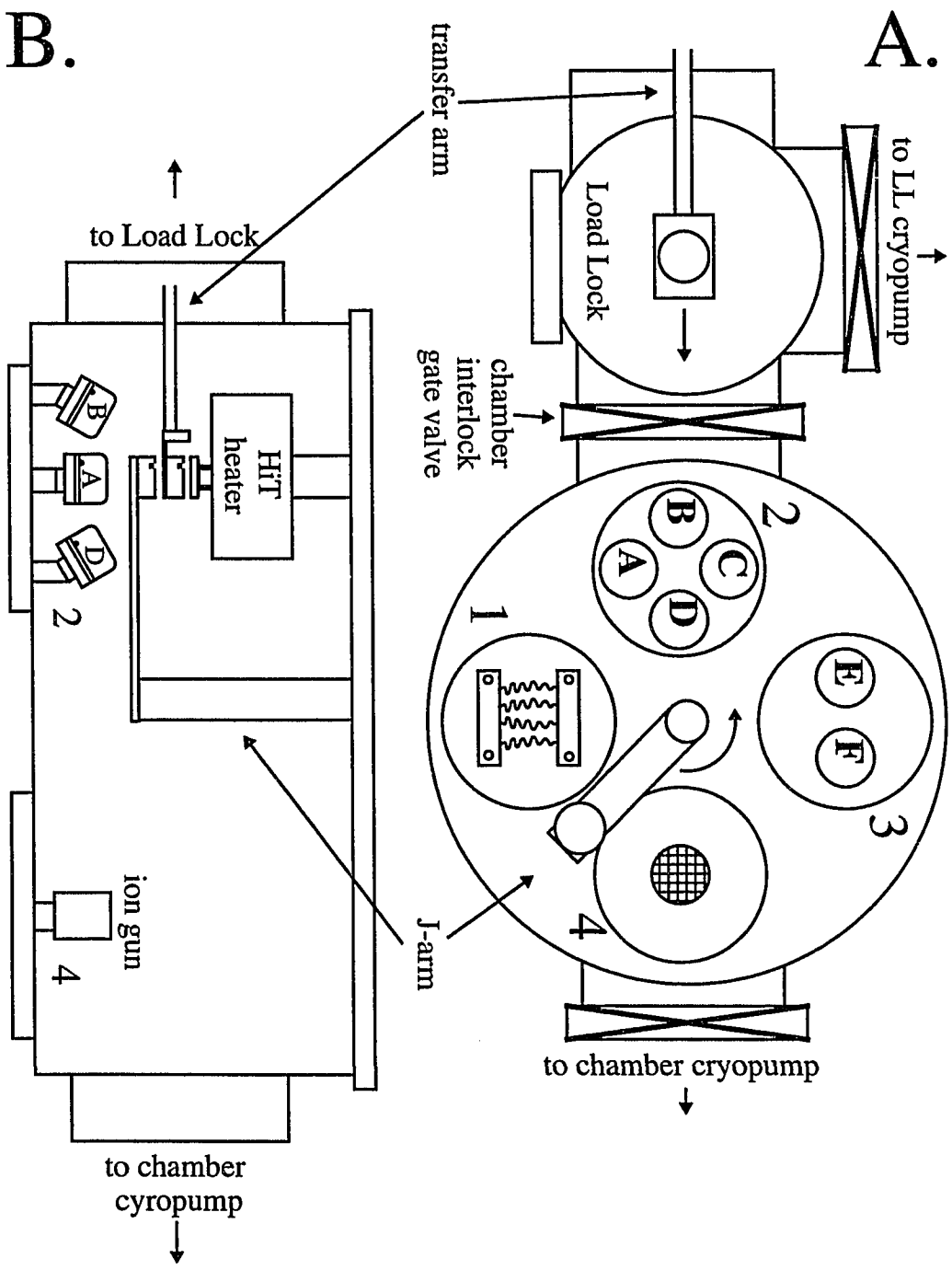

Figure 3.1. The Kurt J. Lesker Company SuperSystem III. A) Top view of the main chamber (diam. ~ 1 m) and load lock. B) Side view of the main chamber (height ~ 0.3 m). Main flanges are numbered 1-4. Sputtering guns are labeled A-F.

The sputter-deposition of Nb is a standard process in superconducting thin film work [Amos (95), Gaidis (94), Kuroda (77)]. The sputter-deposition of NbTi is more unusual, though much work exists [Stejic (94), Karkut (88), Obi (87), Jin (85), Bouchier (78), Spitzer (71), Edgecumbe (64)]. To some extent, however, sputtering is a chamber-dependent process and each group must find its own best conditions with which to produce good films. We began our work by trying to optimize the superconducting properties of our sputter-deposited Nb and $Nb_{0.37}Ti_{0.63}$ films. A number of runs were completed which investigated the influence of substrate temperature, gas pressure, and gun power using the orthogonal design technique [Steinberg (92), Fischer (42)].

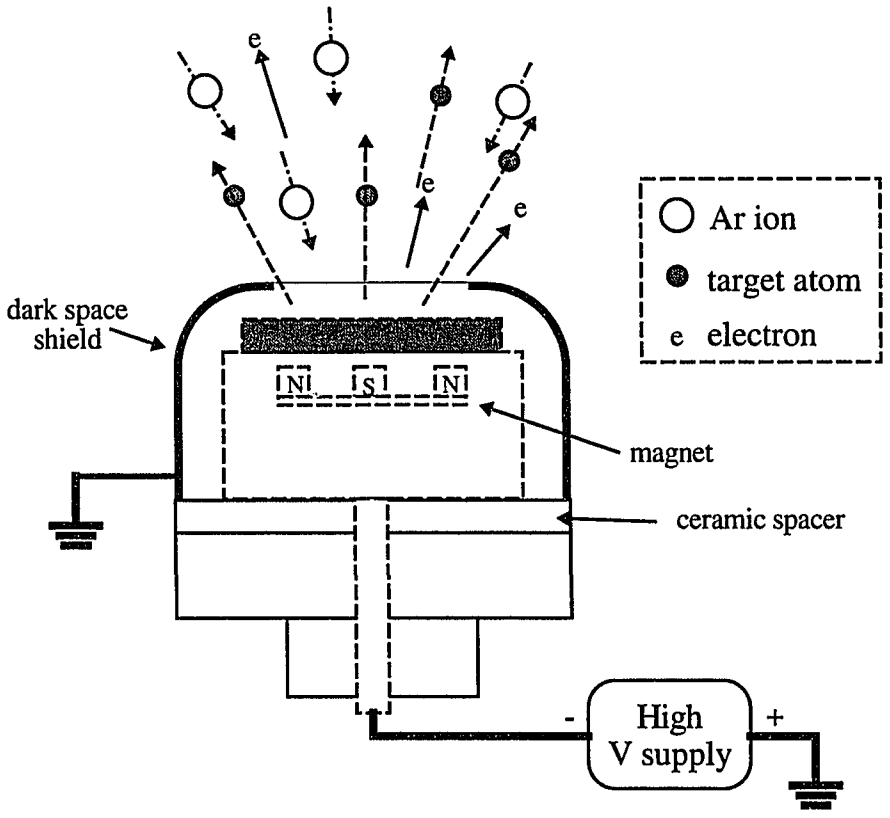

Figure 3.2. The sputtering process. Cutaway view of a magnetron sputtering gun. The surface magnetic field helps to increase the efficiency of the plasma by increasing the path length of the electrons.

The results can be summarized simply: the fewer contaminants incorporated into the film during growth, the closer the superconducting properties are to bulk values. Hence, the higher the deposition temperature, the higher the deposition rate, and the lower the background pressure of contaminants, the better the film. This holds true for Nb as well as $Nb_{0.37}Ti_{0.63}$. The background pressure of the KJL system, with both cryopumps wide open, varied between 2×10^{-8} and 2×10^{-7} Torr (2.66 μPa to 26.6 μPa), depending on how recently a gettering material (like Ti, NbTi, or Ta) had been sputtered or the chamber had been baked. During deposition, the load lock cryopump is closed off and the chamber cryopump is throttled (see below). In this configuration, without Ar flowing, the background pressure rises by a factor of ~ 20. This is an upper limit for the background pressure during deposition, since NbTi is a getter.

3.1.1. Oxidation and Overheating of $Nb_{0.37}Ti_{0.63}$

$Nb_{0.37}Ti_{0.63}$ turned out to be more difficult than Nb to DC sputter at high powers. Two major problems had to be overcome to deposit it reliably: target oxidation and target overheating. $Nb_{0.37}Ti_{0.63}$ oxidizes rapidly because Ti is a strong O getter [Jin (89)]. Oxygen is introduced into the chamber whenever the chamber is opened and during Al trilayer fabrication, which also takes place in the KJL [Gaidis (94)]. A target with an oxidized surface cannot be DC sputtered until the oxide layer is removed—charges build up on the surface until the potential difference between the target and ground is zero. The oxidation problem was greater for the pressed-powder targets we purchased initially, as compared to the arc-melted targets used in this thesis. (All of the sputtering targets used in this thesis were purchased from the Kurt J. Lesker Co.) In the pressed-powder technique, a target is formed by mixing powders of the individual elements in the right ratios and sintering them under high pressure (surprise, surprise). Targets produced this way are fairly porous and of low purity—the $Nb_{0.37}Ti_{0.63}$ pressed-powder targets are 99.9% pure and 85 to 90% of the density of the bulk. We suspect that the higher surface

area of these targets increased their rate of oxidation. Target overheating arises simply because of the poor thermal conductivity of $Nb_{0.37}Ti_{0.63}$. The Torus 2C guns in the Lesker system have a water-cooled Cu plate which helps to keep the targets at a constant temperature during deposition. If heat cannot be effectively removed from the target, the deposition rate changes unpredictably with time because, in general, the sputtering yield (the ratio of target atoms ejected to gas atoms incident) depends on temperature and also the surface oxidation [Chapman (80)]. Target overheating can also lead to buckling, where the target warps irreversibly.

We solved the problem of $Nb_{0.37}Ti_{0.63}$ surface oxidation by purchasing arc-melted targets and by switching to an RF sputtering power supply. Vacuum arc-melting produces a purer, denser target—the $Nb_{0.37}Ti_{0.63}$ was 99.95% pure and the same density as the bulk. (The Nb target was 99.999% pure.) RF sputtering obviates the concerns over target surface conductivity. The target overheating problem was solved by buying a $Nb_{0.37}Ti_{0.63}$ target (4.75 mm thick) bonded to a thin Cu backing plate (1.6 mm) to improve thermal conductivity and to lessen the chance of buckling.

RF sputtering the $Nb_{0.37}Ti_{0.63}$ raised a few new problems which had to be solved. Specifically, at high sputtering powers (above 400 W) the plasma became unstable—the RF impedance matching network would tune to the connecting cable's impedance rather than that of the plasma. This would result in a current node at one of the cable connectors (type N), which would oftentimes then be destroyed. A full solution to this problem would be to shorten the cable connecting the tuning network to the gun and to use more robust cable and connectors. However, the length of the cable between the tuning network and the gun is set, at a minimum, by how close each can be located to the other on the Lesker system. In the present configuration, they can be no closer. Changing the connectors on the cable would require changing the connector on the gun, which would

necessitate removing the gun and remachining it. So, we decided to sidestep the instability problem by simply going to lower RF power, at the expense of deposition rate.

3.1.2. $Nb_{0.37}Ti_{0.63}$/Nb Multilayer Deposition

Once we had characterized the deposition parameters, we were ready to begin depositing multilayers. In summary, we sputter deposited single films and multilayers of Nb and $Nb_{0.37}Ti_{0.63}$ onto radiatively-heated Si wafers (both oxidized and unoxidized). The substrate temperature was ~ 255 °C. The $Nb_{0.37}Ti_{0.63}$ was RF sputtered at 300 W. The Nb was DC sputtered at 100 W. The background pressure of the chamber during deposition was less than ~ 4 x 10^{-6} Torr (0.5 mPa); 10 mTorr (1.33 Pa) Ar was used as the sputtering gas. With these conditions, the Nb deposition rate was ~ 0.15 nm/s and the $Nb_{0.37}Ti_{0.63}$ rate was ~ 0.25 nm/s.

The single component films were typically ~ 200 nm thick. Each multilayer had a ~ 50 nm buffer layer of Nb, followed by 11 periods of alternating $Nb_{0.37}Ti_{0.63}$ and Nb, and finished with a ~ 50 nm cap layer of Nb. The deposition rates were measured (by profilometer) before each run and the shutter times appropriately adjusted. The buffer and cap layers served to prevent possible interdiffusion with the substrate and surface oxidation, and to reduce the effects of surface superconductivity. Samples will be referred to in this work by their run number (format: year-run-piece, e.g. 94-3-2, the second device measured from the third run of 1994) and, in the case of multilayers, by the thicknesses of the individual layers d_{NbTi} and d_{Nb} (format: [d_{NbTi}/d_{Nb}], e.g. [21/6], a 11 period ML with 21 nm thick $Nb_{0.37}Ti_{0.63}$ layers and 6 nm thick Nb layers). See Appendix B for a summary of the sample properties.

3.1.2.1.Substrates

We used Si substrates for this study. Si was chosen because of its general compatibility with superconductor processing and its availability. All were (100) orientation, 51 mm diameter, 250 to 300 μm thick test grade (n or p doped) wafers. We

used both single- (from Virginia Semiconductor Inc.) and double-sided (from General Diode Corp.) polished wafers. Additionally, we wet oxidized substrates (200 to 400 nm SiO_2) on which single films of Nb or $Nb_{0.37}Ti_{0.63}$ were deposited to ensure that the substrate did not interfere with the high temperature transport properties. Some of the first MLs were also deposited on oxidized wafers (before sample 93-32). Before being loaded into the system, all the substrates were cleaned in the standard solvents—TCA then acetone then methanol or isopropanol (from General Chemical Inc.)—for at least 5 minutes in each (with ultrasonic agitation) followed by a DI water rinse. If the substrates were not to be used immediately they were placed in a wafer holder (from Fluoroware Inc.), polished face down.

3.1.2.2.Predeposition

While the substrates were being prepared, we began the predeposition cleaning and equilibration of the sputtering guns and the sputtering rate determination. To light the Nb and $Nb_{0.37}Ti_{0.63}$ guns, we began the Ar gas flow and used the initial burst of pressure to help light the more recalcitrant gun(s)—usually $Nb_{0.37}Ti_{0.63}$. The initial power setpoint was always below 50 W to prevent damage to the supplies. Occasionally, a gun would not light with the initial pressure burst and more drastic measures had to be taken: it was found that opening all the gun shutters and lighting nearby guns would help ignite difficult plasmas, presumably because of the increased ionization available.

Once the guns were lit, the gas pressure and flow were allowed to come to the deposition values. We made all our samples at an Ar pressure of 10 mTorr (1.33 Pa) with a flow of ~ 145 sccm. The pressure is set by a Vacuum General Inc. flow controller system; the flow was set by a venetian-blind type conductance controller, which throttles the pumping speed of the chamber cryopump (CTI-Cryogenics Cryo-Torr 8). The pressure typically varied by no more than 0.02 mTorr during a run, while the flow usually dropped by 1 or 2 sccm.

3.1.2.3. Deposition Rates

The sputtering rate of each gun was measured before each run by loading a scrap piece of Si with photoresist dots on top into the sample position and depositing for at least 10 minutes. The gun powers were ramped slowly (~ 50 W/minute) to the final setpoints. Nb was DC sputtered at 100 W (Advanced Energy Industries MDX-1K) for most of the samples. For samples 94-7 and 94-8, Nb was RF sputtered at 150 W (AEI RFX-600 supply, ATX-600 tuner). $Nb_{0.37}Ti_{0.63}$ was RF sputtered at 300 W. During the rate check, the other guns were not turned off, but were shuttered and turned down to near the initial power setpoint. The scrap wafer was then removed, the photoresist stripped in Acetone with ultrasonic agitation, and the thickness measured with a profilometer (Sloan Technology Corp. DekTak 3030). Typically, we measured the thickness at 6 different positions on the scrap piece. The average rates (measured between 9/14/93 and 1/19/95) are presented in Table 3.1. Although it would have been desirable to monitor the rate constantly during deposition, one can see from Table 3.1. that the rates varied by 13 % or less over a period of 16 months. These rates are fairly low (in no case were we able to exceed 0.4 nm/s) mainly because the target-substrate distance for the HiT station is ≈ 14 cm, and rate falls off at slightly less than $1/r^2$ [Steinberg (92)].

Table 3.1. Average deposition rates of Nb and $Nb_{0.37}Ti_{0.63}$[a]

Nb 100 W DC (nm/s)	Nb 150 W RF (nm/s)	NbTi 300 W RF (nm/s)
0.15(2)	0.14(1)	0.24(2)

[a] we have indicated the error or uncertainty of the last digit of the value by the quantity in parentheses

3.1.2.4. Deposition Temperature

Once the deposition rates were determined, the substrate was placed on the stainless steel wafer carrier with a 50 mm diameter, 1.6 mm thick Cu disk backing the substrate to ensure thermal uniformity. It was then loaded into the sample position (in the

HiT heater box). The thermocouple (TC) temperature setpoint T_{set} was adjusted to 300 °C and the quartz-lamp heater was turned on. Heater-lamp feedback is provided by an Athena Controls, Inc. controller. There are two TC thermometers sitting freely suspended inside the HiT heater box (TC#4 and TC#5 on the system). TC#5 was used exclusively for all the runs (TC#4 consistently reads 100 °C higher than TC#5, because it is located closer to the heating lamps). The sample was then rotated at 30 rpm to ensure thickness and temperature uniformity. Thickness uniformity across an unrotated wafer is predicted to be better than 2% [Steinberg (92)]. A minimum of 15 minutes was allowed between turning on the heater and the start of any film deposition. The TC temperature typically varied by no more than 2 °C during a run. The true substrate temperature (T_{sub}) was measured with Omega Engineering Inc. Omegalable temperature monitors and found to be between 246 and 260 °C for T_{set} = 300 °C.

Processing would have been simpler if the multilayer and single film depositions could have been done at ambient temperature, but we could not produce superconducting $Nb_{0.37}Ti_{0.63}$ films with $T_c > 4.2$ K unless the substrate was heated to a minimum of ~ 150 °C. We *could* however deposit superconducting Nb with T_c near the bulk value at room temperature at high (> 0.3 nm/s) rates. NbTi is very susceptible to O and N contamination [Collings (86), Collings (83)]—elevated substrate temperatures during deposition drive off background contaminants and give the deposited atoms more surface mobility. We chose T_{set} = 300 °C because the thin film properties of both Nb and $Nb_{0.37}Ti_{0.63}$ were satisfactory at that temperature and because it is in line with other experiments on Nb-alloy MLs [Nojima (93), Jin (85)].

3.1.2.5. Cycle Timer

While the substrate temperature was coming to equilibrium, the shutter open times were adjusted to the desired settings. The shutter times were controlled with a solid-state-relay cycle timer (custom made by Macromatic) which allowed independent

control of two gun shutters: $Nb_{0.37}Ti_{0.63}$ was always located in gun B; Nb was DC sputtered from gun C and RF sputtered from gun D (see Fig. 3.1.). The times could be independently adjusted between 0.4 s and 24 hours and that cycle could be repeated up to 64 times. The cycle begins and ends with the Nb shutter open. The timer was spliced directly into the original control circuitry of the shutters—the shutters will not operate normally as long as the timer is wired into the circuit. All timer adjustments were made manually: a guess was made as to the proper settings to achieve the desired layer thicknesses (the deposition rates must be known); the times were then measured and the timer readjusted if necessary. The shutter on each gun takes a finite time to open (usually 1 s or less) and close (from 1 s for guns B and D to 4 s for gun C). These delays are figured into the calculation of the final layer thicknesses. Because the opening and closing times were suspected of being slightly variable, the sputtering powers (hence the deposition rates) were chosen such that any variation or miscalculation of the shutter open time would only lead to a small fractional error in the layer thickness. In practice, this meant that shutters were open for half a minute at least.

3.1.2.6. Multilayer Geometry

All of the MLs in this study have similar geometries. Each has a ~ 50 nm buffer layer of Nb followed by 11 alternating bilayers of $Nb_{0.37}Ti_{0.63}$ and Nb capped with another ~ 50 nm Nb. Fig. 3.3. shows a schematic of a 11 period (Λ) 20 nm $Nb_{0.37}Ti_{0.63}$/5 nm Nb multilayer. We chose to make 11 Λ MLs to keep the total film thickness under 0.5 μm, which makes etching easier (see below), and to be in accord with other recent experiments on flux pinning in NbZr multilayers, which use a simiar number of periods [Koorevaar (93), Nojima (93)]. The buffer and cap layers' most important function is to suppress surface effects in near parallel magnetic fields—surface superconductivity H_{c3} [Maj (91)] and the surface barrier to flux entry/exit [Ling (95)]. A normal metal cladding (or a thick, low H_{c2} superconductor such as Nb) changes the boundary conditions on the

GL wavefunction and its derivative $d\psi/dx$ [Tinkham (80)], suppressing surface effects found at a superconductor-insulator boundary. The cap layer also protects the ML from oxidation and other contamination, while the buffer layer prevents substrate-ML interdiffusion (probably not a large concern at such low values of T_{sub}).

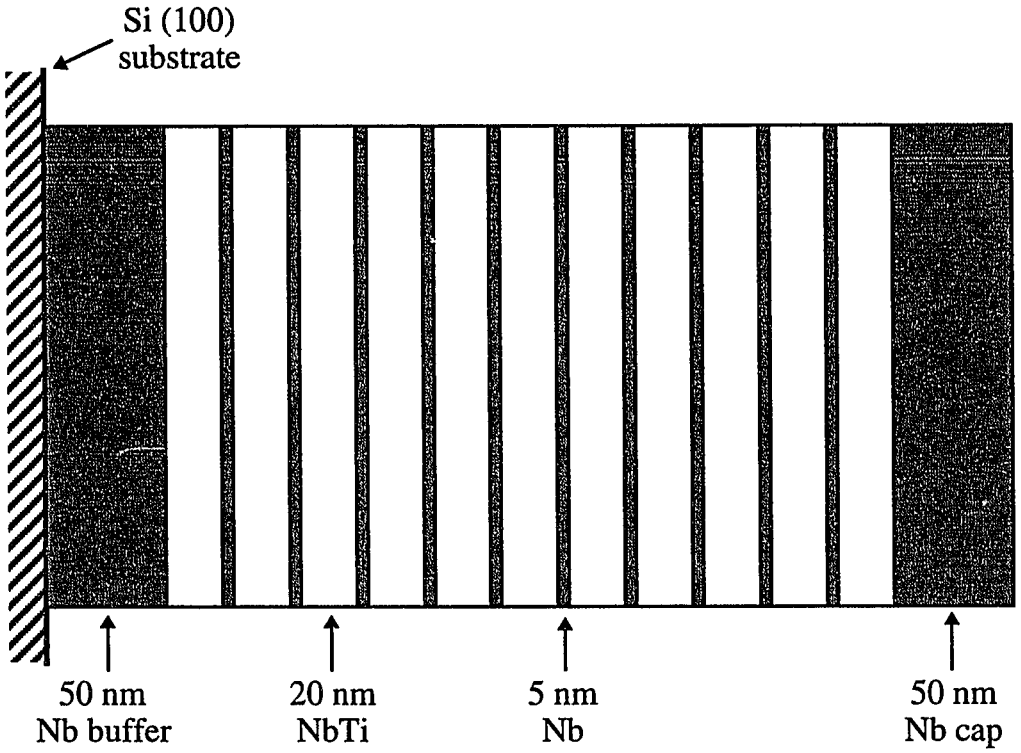

Figure 3.3. 11 period 20 nm $Nb_{0.37}Ti_{0.63}$/ 5 nm Nb multilayer. All multilayers had 50 nm buffer and cap layers with varying $Nb_{0.36}Ti_{0.64}$ and Nb thicknesses.

Once the substrate temperature equilibrated (a minimum of 15 minutes), the main shutter was opened, and the buffer layer was begun. To produce the geometry in Fig. 3.3. the cycle timer was set to deposit eleven bilayers (6 output pulses): when the buffer layer was nearly complete (50 nm minus one Nb layer thickness), the cycle timer power was turned on to begin the ML deposition. When the 11 bilayers were finished, the cycle timer leaves the Nb shutter open (the timer's default position). The Nb shutter was closed manually after the cap layer was deposited.

After the deposition was complete, the heater was immediately shut off, the rotation stopped, the guns ramped to ~ 50 W and turned off, and the Ar flow set to zero. The sample was then transferred into the load lock, to cool in vacuum. Typically, we waited 2 to 3 hours to remove the sample from the system. If the sample was not to be patterned right away, it was stored in an evacuated desiccator.

3.2. Lithography and Etching

We used standard image-reversal photolithography [Muller (86)] to liftoff an Al contact/mask layer which defines our devices. After the liftoff of the Al, the wires were reactive ion etched (RIE) in SF_6, which does not attack Al significantly. Finally, the Al over the device region was removed by wet etching and the wires were made ready to test. The various steps of this process are shown in Fig. 3.4.

3.2.1. Al Liftoff

Initially, we tried a positive photoresist mask (Shipley AZ 1470) with no contact layer, but we found that the contact resistances of such devices were high, unstable, or both, possibly because of native oxide growth on the Nb cap layer [A. H. Worsham, private communication] or because of resist implantation in the cap layer [M. C. Gaidis, private communication] during RIE (see below). Additionally, the high contact resistances of early wires led to heating problems at high currents (above 20 mA). We therefore decided to use a mask layer which would serve to both protect and make contact to our wires. The most straightforward way to do this was to liftoff an Al layer.

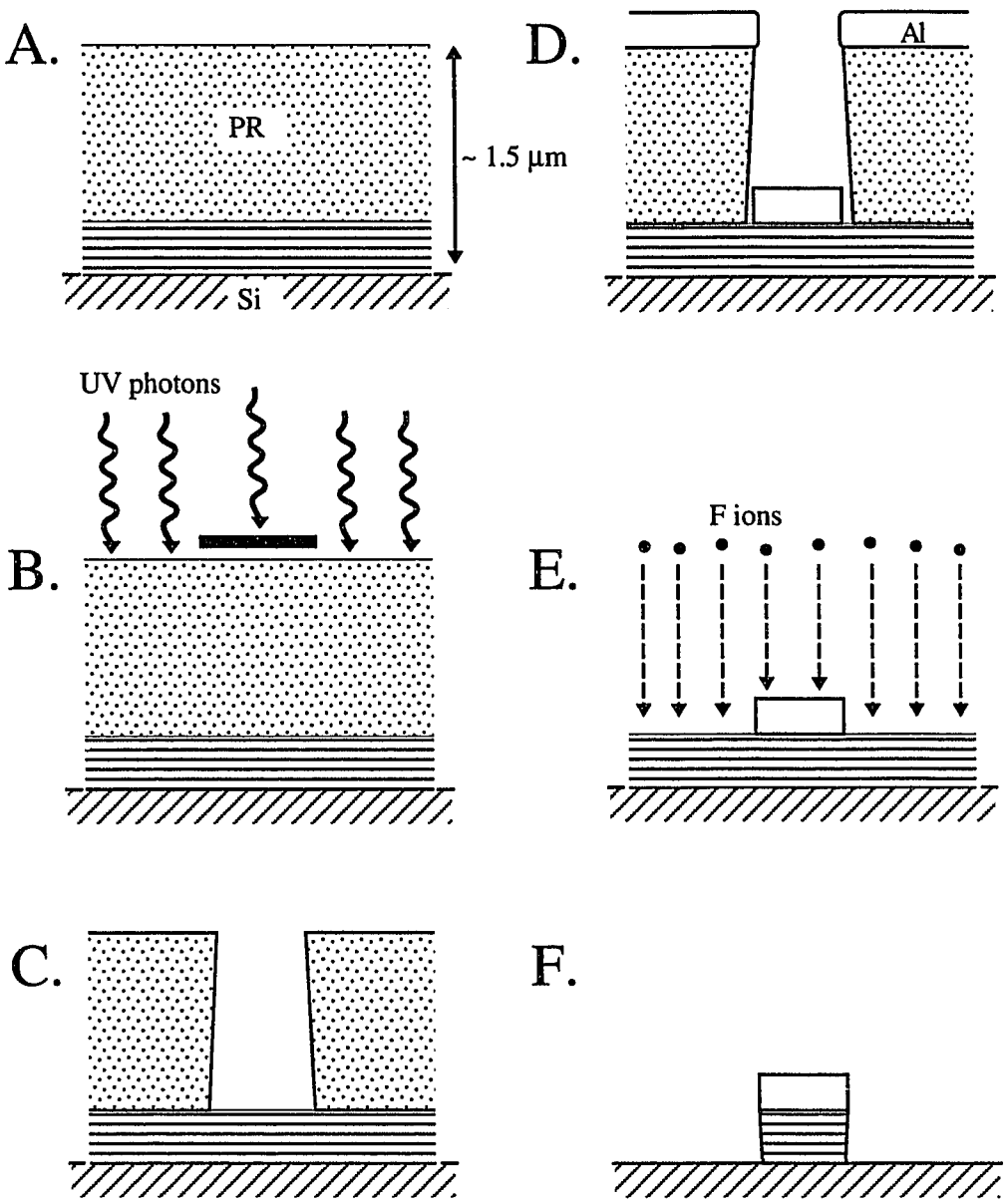

Figure 3.4. The photolithographic process: A) thick layer of image reversal photoresist spun on multilayer, B) UV exposure of optical mask, C) development of pattern, D) deposition of Al contact/mask layer, E) liftoff of Al layer, followed by reactive ion etch, F) device prior to Al removal by wet etch.

3.2.1.1. Photolithography

We used Hoechst Celanese AZ 5218-E Image Reversal photoresist (PR) to define the device region. The optical lithography mask (called JC1) was designed and made at the National Nanofabrication Facility at Cornell University with the assistance of Dr. M. Rooks. Fig. 3.5. is a schematic of this mask.

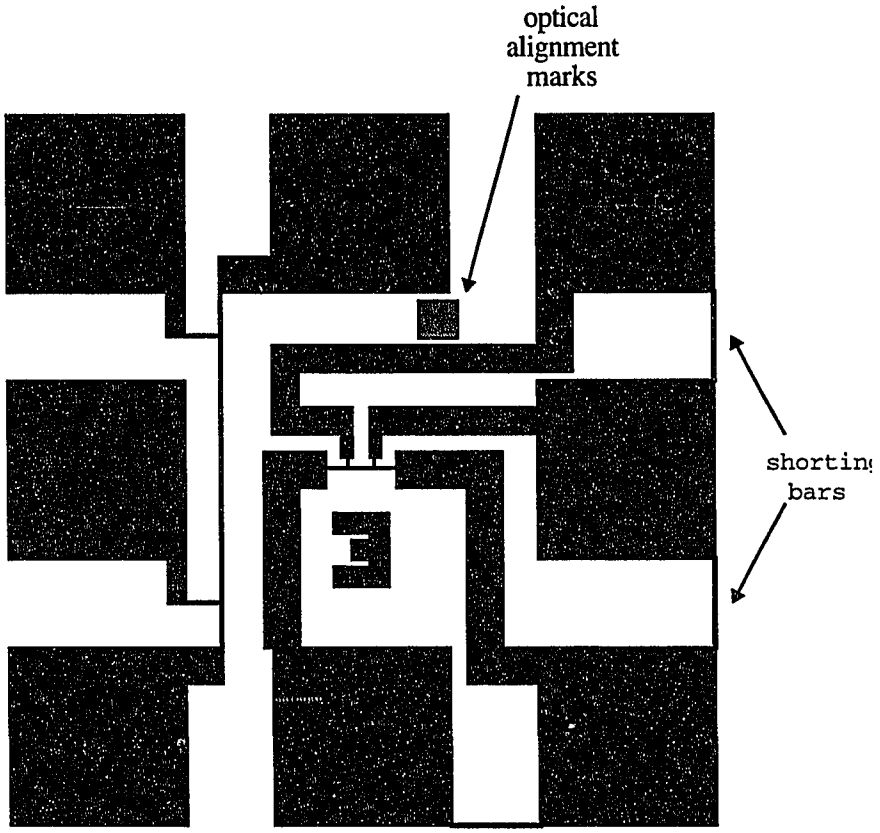

Figure 3.5. A schematic of the optical mask pattern (not to scale). Device is at the center. Width indicated by number underneath. Geometry typically 20 squares. A second 25 μm wide, 1000 μm long wire is to the left.

The wires used in this thesis are all nominally 3 μm wide and 60 μm long (center-to-center spacing of the 3 μm wide voltage taps). The mask has many different wire

patterns, with widths from 1 to 50 μm, including a Hall probe pattern. Note the shorting bars between the device contact pads (included in case we wished to do e-beam lithography) which must be broken prior to measurement (see Ch. 3.2.3.1.). The 5218 processing recipe was adapted from one M. Gaidis [94] developed (see Appendix A). Once the PR was spun on and baked at 90 °C on a hotplate, we exposed the mask pattern on a Hybrid Technologies Group, Inc. mask aligner (model 64-5X), usually in hard (vacuum) contact mode. The resist was then post-exposure baked at 110 °C (to cross-link the polymers in the exposed regions) and then flood exposed (to weaken the originally protected areas). The pattern was then developed in Shipley Microposit 351 developer. If the pattern looked satisfactory under the optical microscope, it was baked again at 110 °C to harden the PR. If unsatisfactory, the resist was stripped in developer or acetone or both, then rinsed in methanol or isopropanol and DI water and the lithography process restarted. Occasionally, a sample with stubborn traces of resist had to be RIE cleaned in oxygen (see below). Usually, we found that using older 5218 was the cause of most of our lithography problems—older resist tended to be "pockmarked" or pinholed. These problems were cured by using newer 5218.

3.2.1.2. Al Sputter Deposition

After the hard bake, samples were loaded into the KJL for sputter deposition of the Al contact layer. During pumpdown, the Al was presputtered and brought up to full power. The Ar pressure and flow were the same as those during the multilayer runs (10 mTorr, ~ 145 sccm). We deposited Al with the sample on the J-arm (target-substrate distance ≈ 5 cm) at room temperature. At 300 W DC, the measured Al deposition rate was 2.5 nm/s.

The only difficulties we encountered with the Al deposition occurred when we tried to deposit on a broken multilayer wafer [94-4, 94-6]. These pieces were mounted to 25 mm square glass microscope slides with AZ 1470 photoresist to facilitate handling.

However, when they were placed in the KJL for Al deposition, some of the 1470 boiled under vacuum and contaminated the Al. In the end, the entire multilayer fabrication had to be redone.

3.2.1.3. Liftoff

Samples were taken out of the KJL and placed directly in acetone. Typically, we would soak the samples for ~ 30 minutes and then use an acetone spray bottle to loosen the remaining Al. This might be repeated once or twice. Occasionally, a stubborn sample was left to soak overnight. If that did not do the trick, we resorted to ultrasonic agitation for ~ 30 s bursts—though this sometimes removed Al in areas we did not want removed. In general, the Al did not have adhesion problems.

3.2.1.4. Dicing

Once the Al layer had been lifted off satisfactorily, the device-side of the wafer was protected by a spun-on layer of photoresist (Shipley AZ 1470) which was not baked. The wafer was then diced on a Tempress 601 Dicing Saw. The blades were purchased from Assembly Technologies, Inc (through Kulike & Soffa). Typically, a 125 μm (0.005") deep cut was made, which allowed the wafer to be split into the various devices easily. The PR was removed with an acetone rinse. At this point, we selected the chips for RIE—generally we etched all the viable 3 μm wide wires and some backups of other widths, usually 5 or 10 μm.

3.2.2. Reactive Ion Etching

The RIE used predominantly in this work was a Cooke Vacuum Products CV-300 [see Face (87)]. A Vacutech 1520 was also used in the initial stages (until its CPU died). Reactive ion etching is a standard technique throughout the thin film and semiconductor processing industries [Chapman (80)] for creating a chemically active ion and delivering

it to the surface of the material to be etched. Its greatest advantage over other etching techniques is that RIE can be both highly selective and anisotropic (through proper gas choice and plasma conditions). Generally, a flow of gas (like SF_6) is introduced into the chamber and RF power is applied between the electrodes, creating a plasma. The energetic collisions in the plasma break up the gas into chemically active ions ($SF_6 + e^- \rightarrow SF_5 + F^-$), which are then accelerated toward the substrate by the average DC bias between the plates V_{dc}, which is caused by the capacitive coupling of the power to the plasma through an impedance matching network.

The Cooke machine is a parallel plate, low pressure, low flow RIE (as opposed to the Vacutech, which is a high pressure, high flow machine). It is well suited to anisotropic etching, since the anisotropy of the etch process depends on the mean free path of the etchant ion and the ion's incident energy, both of which are high at low gas pressures. The gases we used for etching are DE101 (CF_4 + 9% O_2) or SF_6 for Nb and $Nb_{0.37}Ti_{0.63}$ and O_2 for PR. SF_6 was preferred for its higher rates (see below) and used for the majority of our samples. In Table 3.2. we present the various etch rates measured at constant DC bias—it was found that constant bias regulation, rather than constant power regulation, provided more etch rate reproducibility [M. C. Gaidis, private communication]. A word of caution: the etch rates were measured by protecting small areas with PR, then stripping the resist and measuring the mesa height with the DekTak 3030. It is known [ChenB (90)] that RIE rates change depending on the masking material—in particular, we found the etch rates measured with a photoresist mask *underestimated* the inferred etch rates with an Al mask, sometimes by a factor ~ 2. This did not cause a problem, however as we always etched test samples to check calculated etch times and because our samples do not suffer if the Si substrate is etched.

Before samples were etched, we pumped down to 1 x 10^{-5} Torr and then cleaned the belljar with a 5 minute O_2 etch (10 mTorr, ~ 10 sccm, 50 W RF, -400 V_{dc}) followed

by a 5 minute SF_6 etch (4 mTorr, ~ 13 sccm, 60 W RF, -250 V_{dc}). The impedance matching network has to be adjusted manually to minimize the reflected power. (Network positions for O_2 etch: target load = 0005, J-load = 0043, input tune ~ 11 o'clock. SF_6 etch: target = 0005, J-load = 0035, input tune ~ 3 o'clock.) After the SF_6 preclean, the belljar was vented and the samples were loaded on the bottom (J-arm) electrode, at a radius midway between the center and the edge (~ 3 cm). The chamber was then pumped down to 1 x 10^{-5} Torr (~ 10 minutes) and the samples were etched in SF_6 (same conditions as above). Once the etching was complete, the chamber was vented and the samples were inspected visually and with a Fluke 77 ohmmeter to ensure the films were etched to the substrate. If a number of samples were to be etched in quick succession, the O_2 and SF_6 clean were *not* repeated.

Table. 3.2. RIE rates at 4 mTorr measured with a photoresist (PR) mask[a]

Conditions	Nb (nm/s)	NbTi (nm/s)	PR (nm/s)	Al (nm/s)
DE101 -300 V_{dc}	0.29	0.12	~ 0.15	n/a
DE101 -400 V_{dc}	0.42	0.38	~ 0.16	n/a
SF_6 -200 V_{dc}	2.28	1.11	< 0.1	< 0.1
SF_6 -250 V_{dc}	2.17	1.39	< 0.1	< 0.1
O_2 -400 V_{dc}	n/a	n/a	~ 1.67	n/a

[a] accuracy ± 10%

3.2.3. Al Wet Etch

When the RIE of the samples was complete, we removed the Al over the device area to prevent parasitic shunt conductance. This step was taken only when we first noticed that current-voltage characteristics of some samples which did not have the Al layer removed behaved strangely—they appeared to have an ohmic resistance below the critical current. We remeasured these samples with the Al layer removed and the ohmic resistance disappeared. It is possible that a poor Al/Nb interface caused by dirt and oxidation on the Nb surface (samples occasionally waited days between multilayer

deposition and lithography) allowed current sharing through the Al. Current sharing is not unknown in bulk superconductors [Ekin (78)], though the Al/Nb interface would have to have been extremely dirty to explain the measured ohmic resistance (10s of mΩ), given the large areas of the contact pads and the wide separation between the current leads and the voltage taps. What we do know is that all the samples without Al over the device behaved nicely.

To remove the Al, we first protected only the contact pads by brushing on a thick layer of AZ 1470 over them and baking the sample on a hotplate for a few minutes. The samples were then placed in a commercial Al wet etchant (General Chemical Corp. PAE—Phosphoric Acid : Nitric Acid : Acetic Acid : water :: 16 : 1 : 1 : 2). PAE has an etch rate of approximately 0.4 nm/s at room temperature. It does not attack Nb or $Nb_{0.37}Ti_{0.63}$; their etch rates are at least a factor of ~ 50 smaller than that of Al. When all the Al was removed, as confirmed in an optical microscope, the PR was removed in acetone.

3.2.3.1. Mounting the Sample

Before the samples could be mounted in the cryostat, the shorting bars between the device contact pads had to be scratched out with a scribe tool. With firm pressure on the scriber (enough to leave a scribe mark on the Si surface) and 2 or 3 passes over the bars, they were removed without further ado. The chip was then attached to the Cu sample stage with a small amount of Dow-Corning high vacuum grease, to improve thermal contact.

3.4. Cryostat and Dewar

The cryostat we used for all our measurements was designed by Dr. X. S. Ling and built at the Josiah Willard Gibbs machine shop. It is a variation of a standard "dipstick" design for making variable temperature measurements: the sample is mounted

on a Cu bar, along with a thermometer and heater and all the electrical leads; this bar has a weak thermal link to the liquid He bath through a stainless steel screw and a nylon spacer; the sample space is surrounded by a bronze can, which may be evacuated to reduce the thermal contact with the bath still further—pressure in the cryostat was measured with a Veeco Thermocouple (TC) vacuum gauge. Our design added the ability to vary the sample's orientation in an applied magnetic field.

3.4.1. Magnetic Field

We used the trusted "quantum transport" dewar [see Klepper (91)] for all the measurements--it too is a standard design, consisting of two nested pyrex dewars with a superconducting magnet (Magnetic Corporation of America) at the bottom of the liquid He dewar to supply the field. The magnet has a 2.5 cm bore and produces 0.2525 T/A. At 4.2 K it can produce a field of ~ 6.5 T; if the He bath is pumped, the field can go to ~ 8 T. The magnet was charged by a Lakeshore 612 superconducting magnet power supply. A schematic diagram of the cryostat and dewar is presented in Fig. 3.6.a.

One of our concerns was that the sample always sit at the field center—the magnetic field of the magnet in the Quantum Transport dewar is uniform only over a small volume. Our measurements of the field uniformity (using an HP gaussmeter) versus displacement from the magnet center are shown in Fig. 3.7. We placed a rubber stopper around the cryostat at the proper height (102.9 cm from the top of the 1" Cajon fitting to the magnet field center) to ensure that the sample stage sat as closely to the field center as possible. We estimate that our uncertainty in height was ~ 1 cm, which corresponds to an uncertainty in field of ~ 2.5%.

3.4.2. The Rotating Stage

Sample rotation was accomplished with a worm gear attached to the sample stage axle—ideally, we can rotate the sample normal from perpendicular to parallel with the

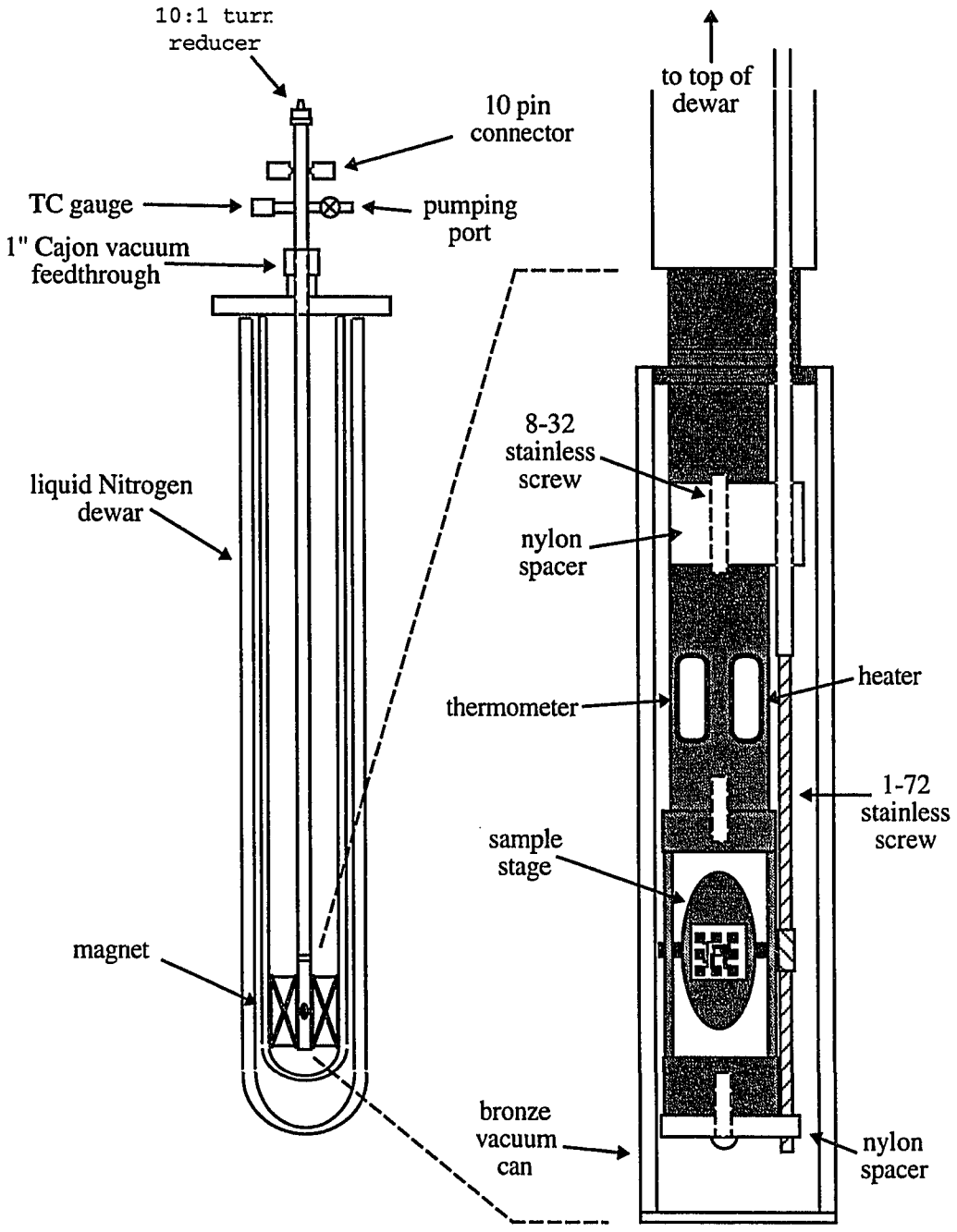

Figure 3.6.a. Variable temperature rotating stage cryostat inserted in dewar. The blowup shows a cutaway front view of the variable temperature stage.

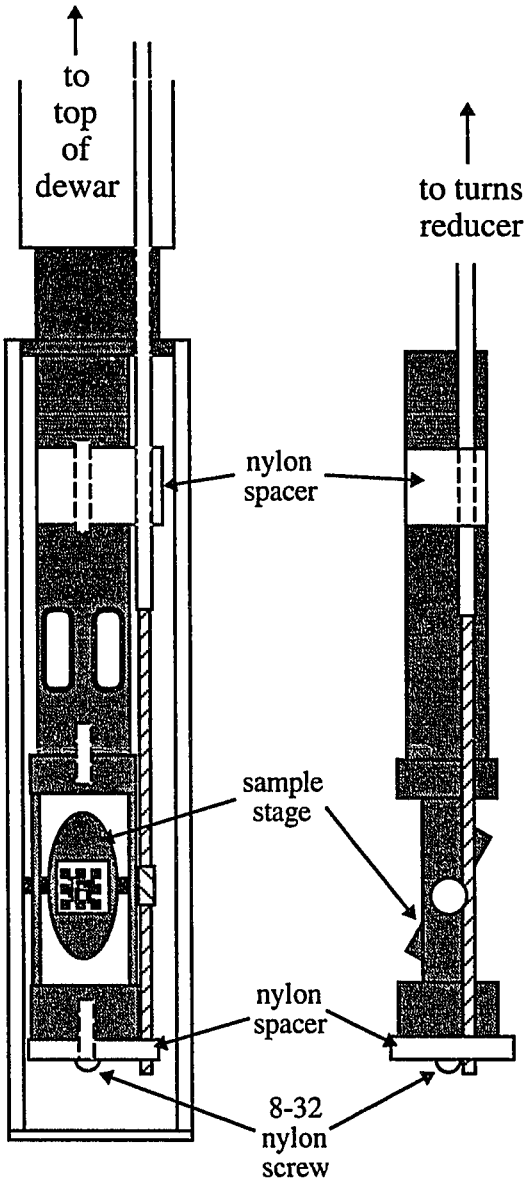

Figure 3.6.b. Variable temperature rotating stage cryostat—rotation mechanism. The left is the front view of the sample area from Fig. 3.6.a. The right is the side view of the sample area showing the linking of the worm gear mechanism.

field *in situ*. The worm gear is made from a 1-72 stainless steel screw welded to the bottom of a 1/16" (1.6 mm) OD stainless steel tube which passes out the top of the cryostat through a Cajon vacuum fitting. The tube is connected to a 10:1 turns reducer. A small bronze wheel, threaded to match the screw, is mounted on the sample stage axle (see Fig. 3.6.). By aligning the screw and wheel so that the threads mesh, the sample axle (and the stage) may be rotated over a wide range ($-30° < \theta < 120°$, where θ is the angle between the cryostat axis and the sample stage) by turning the tube connected to the screw. To set the angle $\theta$for measurements, the sample stage was aligned parallel to the cryostat axis by eye and the screw was turned to rotate the stage to the desired angle (all at room temperature). The worm gear is shown in Fig. 3.6.b.

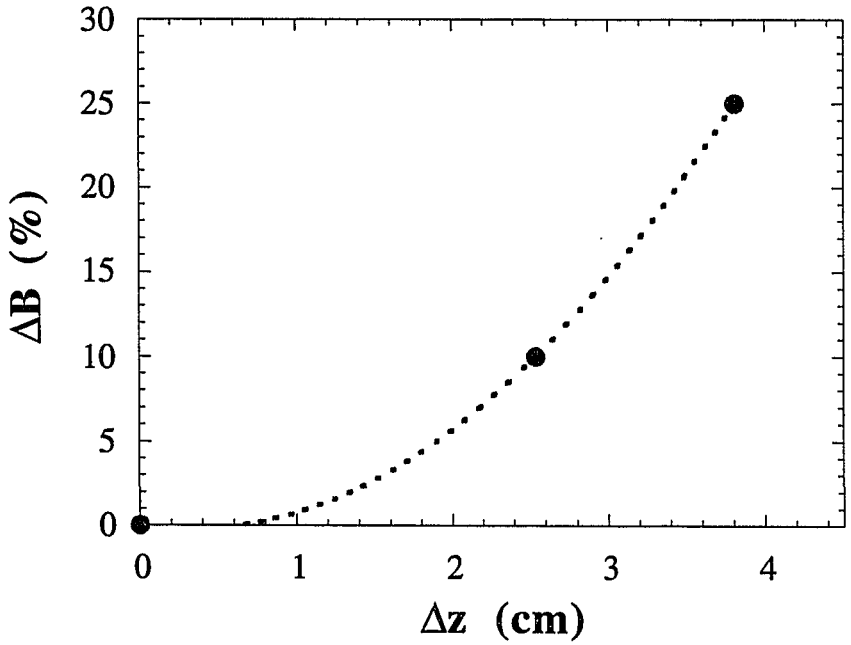

Figure 3.7. The measured percentage change in magnetic field ΔB as a function of distance away from the magnet center Δz. The dashed line is a guide to the eye.

In practice, it is difficult with the present design to rotate the sample at low temperatures *in situ*. Hence, for most of our measurements, the sample stage angle θ was fixed before the cryostat was placed in the dewar. At room temperature, the worm gear mechanism works flawlessly. At low temperatures, the axle upon which the stage is fixed has a tendency to bind in the through-hole (the machining tolerances did not allow for thermal contraction), preventing free rotation of the stage. We alleviated this problem (late in this work) by filing down the axle to allow more clearance.

3.4.2.1. Angular Error

We call the angle θ identically equal to the angle that the applied magnetic field makes with the sample planes during measurement. There are a number of places error can creep in: the non-collinearity of the cryostat and the magnet, the misalignment of the sample stage with the cryostat axis, the uncertainty of the angular calibration (turns per degree), and stage movement during thermal cycling. The collinearity is set by the machining tolerances of the cryostat and the dewar. These errors lead to an uncertainty of ~ 0.5°. The alignment of the sample stage is limited by the resolution of the human eye ~ 1.5°. The calibration error is ≈ 0.025°. The movement of the stage during thermal cycling is a possible, though unquantifiable, additional source of error—however, when we have remounted samples and remeasured J_c, the two sets of values have agreed to within our error in measurement. Adding these together in quadrature we obtain a total uncertainty in absolute angle θ of ~ 1.6°. Measurements of the sample angle made by rotating the sample *in situ* (using the cusp in J_c at 0° to calibrate the absolute angle with the field) and *ex situ* agree within our error (see Fig. 3.12.).

3.4.3. Variable Temperature Sample Stage

The temperature of the samples is measured with a Cryocal carbon-glass (CG) resistance thermometer (Serial # C2322) mounted in a slot on the Cu bar and heat sunk

with Ag paint. The sensor is calibrated at 35 points between 1.5 and 20 K by the manufacturer. The resistance of the CG thermometer is measured with an excitation current of 10 μA (supplied by Yale-made electronics), which can be reversed to eliminate thermal voltages. Typically, thermal voltages cause less than a 25 mK error. This is small compared to the error caused by the magnetoresistance of the CG sensor $\Delta T/T \sim 1.5\%$. In most measurements of the temperature, the thermal voltages were not taken into account.

The heater is simply a 1 kΩ metal-film resistor, mounted in a hole drilled through the Cu bar and heat sunk with General Electric 7031 varnish. 15 V can be applied across the heater for a maximum ΔT above liquid He temperature of ~ 25 K.

The rotating stage design also causes some problems with the thermometry—the worm-gear mechanism is a heat loss path in parallel with the weak link. This causes a linear offset between the true sample temperature and the thermometer temperature, for which we have corrected in this thesis. The correction procedure is described in Appendix D.

3.5. Electrical Transport Measurements

We characterized the behavior of our films and multilayers primarily by measuring their electrical transport properties. The measurement of the sample voltage $V(I, B, T, \theta)$ gave us the critical current density $J_c(B, T, \theta)$; measuring $R(T, B, \theta)$ gave us the critical temperature $T_c(B, \theta)$, from which we estimated the upper critical field $H_{c2}(T, \theta)$. Contact to the samples was made by spring-loaded pins (Augat Pogo Pins). Transport measurements can provide much of the useful information needed to study the flux pinning properties of any superconducting system.

3.5.1. Critical Current Density Measurements—DC Transport

We measured the DC current-voltage characteristics (I-Vs) of our samples as a function of the applied magnetic field B, the temperature T, and the angle the sample stage made with the applied field θ. The transport current was applied in the planes and perpendicular to the magnetic field (± 2°). The critical current I_c was defined as the current where the sample voltage first reached 1/3 μV, which corresponds to an electric field criterion of 55.6 μV/cm. Sample dimensions were then measured in an SEM (JEOL JSM-6400) at Yale by J. Sleight and M. Deshpande, which was regularly calibrated, and the resistivities and current densities were calculated.

3.5.1.1. Errors

The inaccuracies of the dimensions stem mostly from the uncertainty in the sample thicknesses (~ 10%). An additional source of error for the critical current density (as mentioned above) for small θ is the uncertainty in θ: We measured $J_c(\theta)$ for θ near 0° for sample [21/6] to determine this uncertainty. We plot our results in Fig. 3.12. Using our data at 5 and 6 T, we find $\Delta J_c/J_c \approx 1/J_c \, (dJ_c/d\theta) \, \Delta\theta \approx 10\%$ near $\theta = 5°$. All other sources of error are much smaller than the contributions from the sample area and angle—our total uncertainty in J_c in near parallel fields is therefore ~ 15%.

Two DC measurement setups were used: the pre-computer apparatus and the post-computer apparatus. No differences were found between the two.

3.5.1.2. All-Analog, Pre-Computer DC Transport Measurements

In the pre-computer era, the DC current bias was supplied by a dry battery in series with a resistor. We measured the current using the proportional voltage across a sense resistor with a buffer instrumentation amplifier. The voltage response of the sample

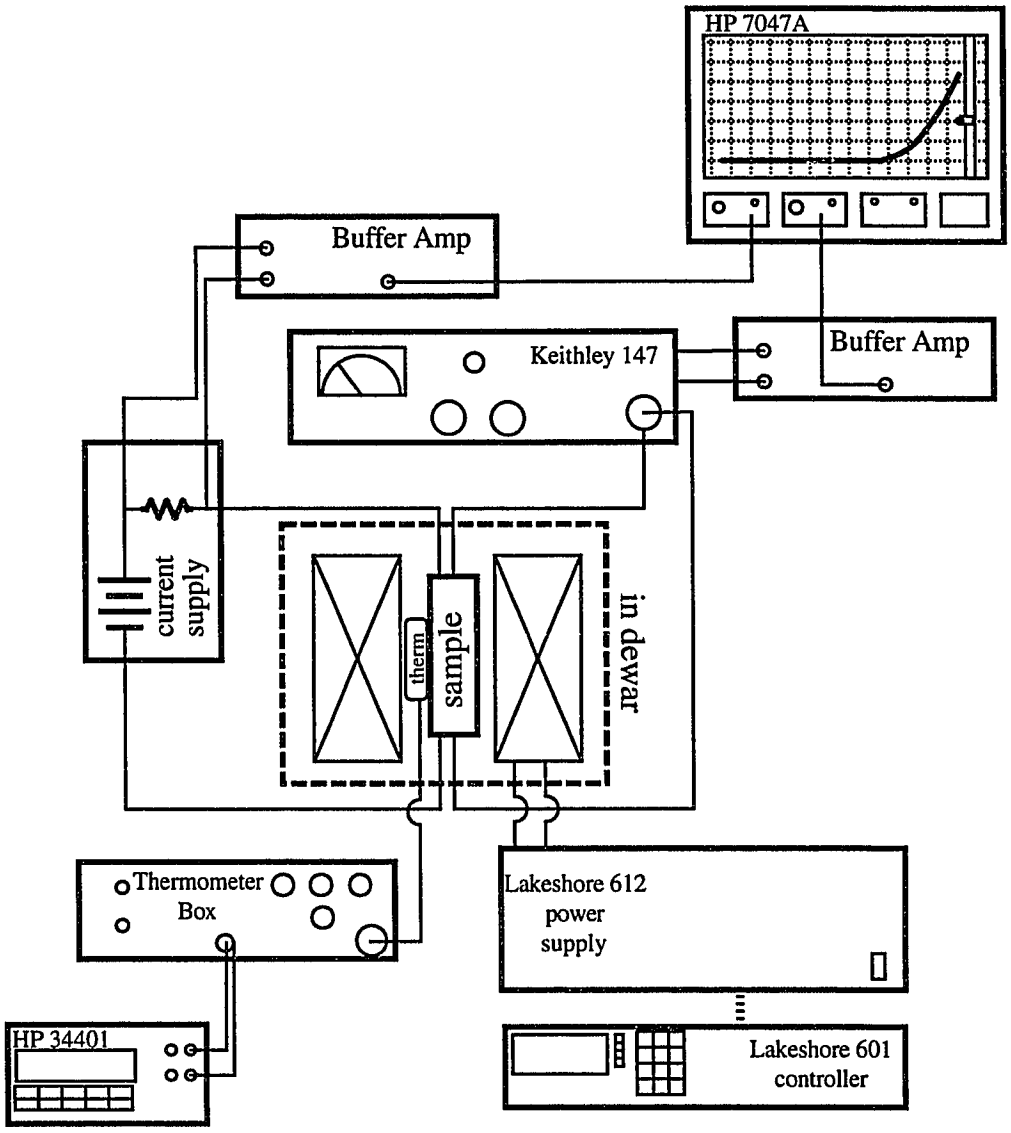

Figure 3.9. Pre-computer DC transport setup for $V(I, B, T, \theta)$ measurements.

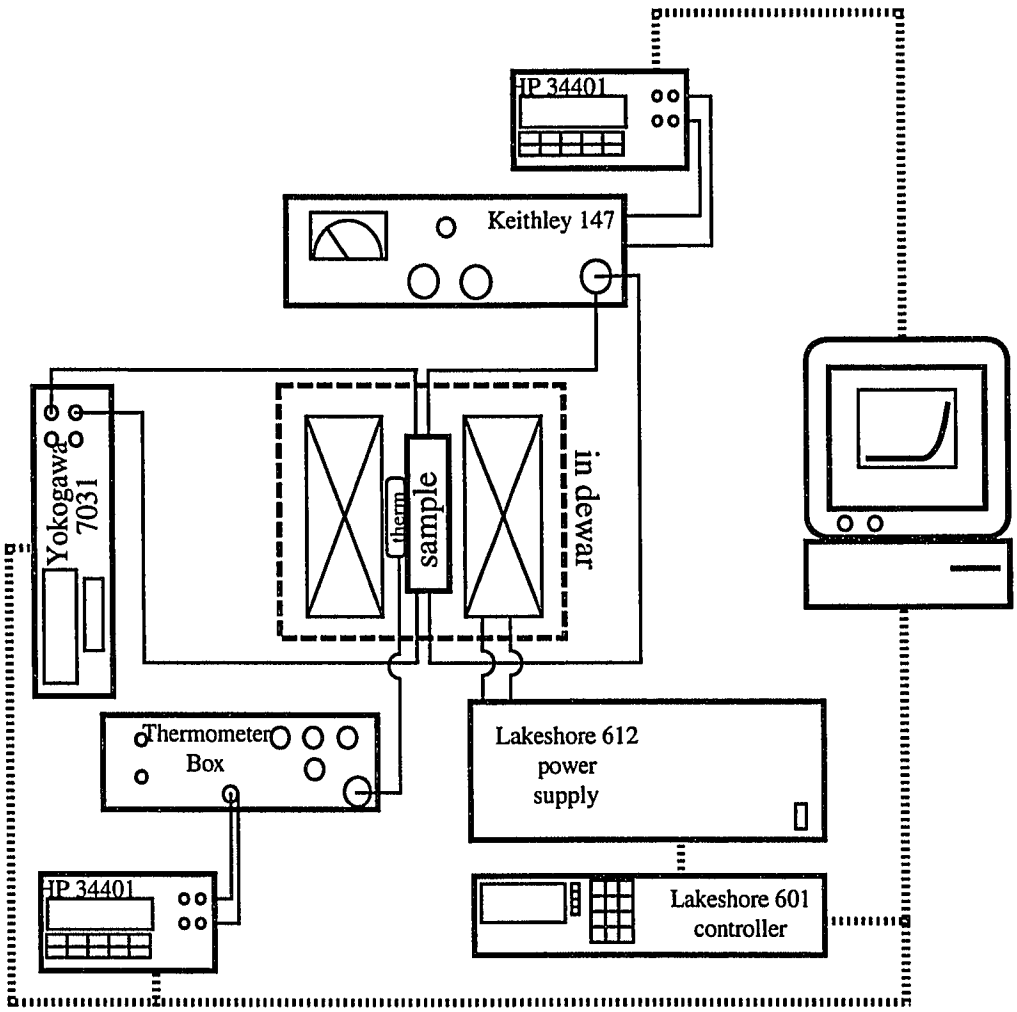

Figure 3.10. Post-computer DC transport setup for $V(I, B, T, \theta)$ measurements.

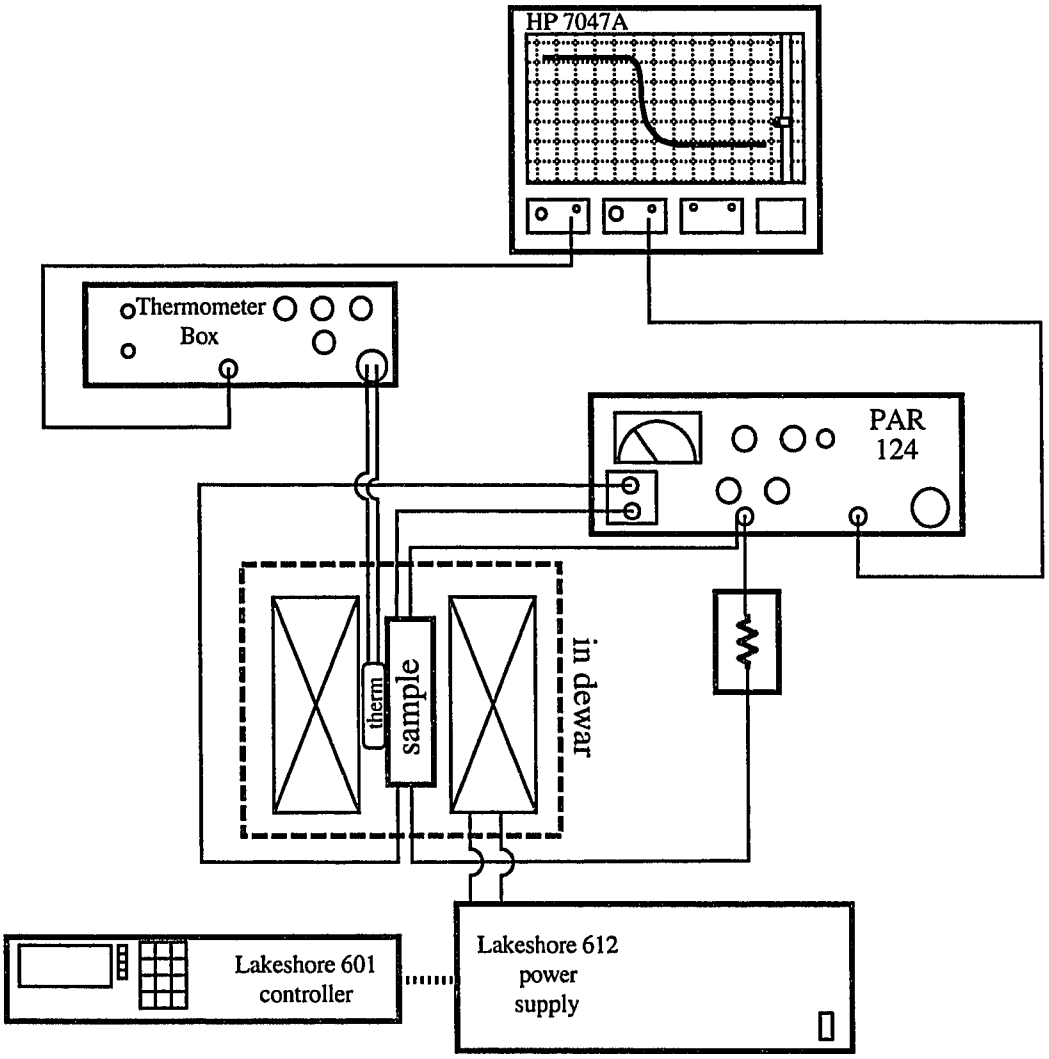

Figure 3.11. AC transport setup for $R(B, T, \theta)$ measurements.

was measured directly with a Keithley 147 Nanovolt Null Detector. Noise levels of 150 nV were typical. The analog output of the nanovoltmeter was then fed into a buffer amplifier. The temperature of the sample was set by varying the voltage across the heater manually (no feedback controller was employed)—we could achieve temperature stability of ± 25 mK routinely, as measured by the thermometer resistance by a Hewlett-Packard 34401 digital multimeter (DMM). We recorded the results on a Hewlett-Packard 7047A x-y recorder. This setup is illustrated schematically in Fig. 3.9.

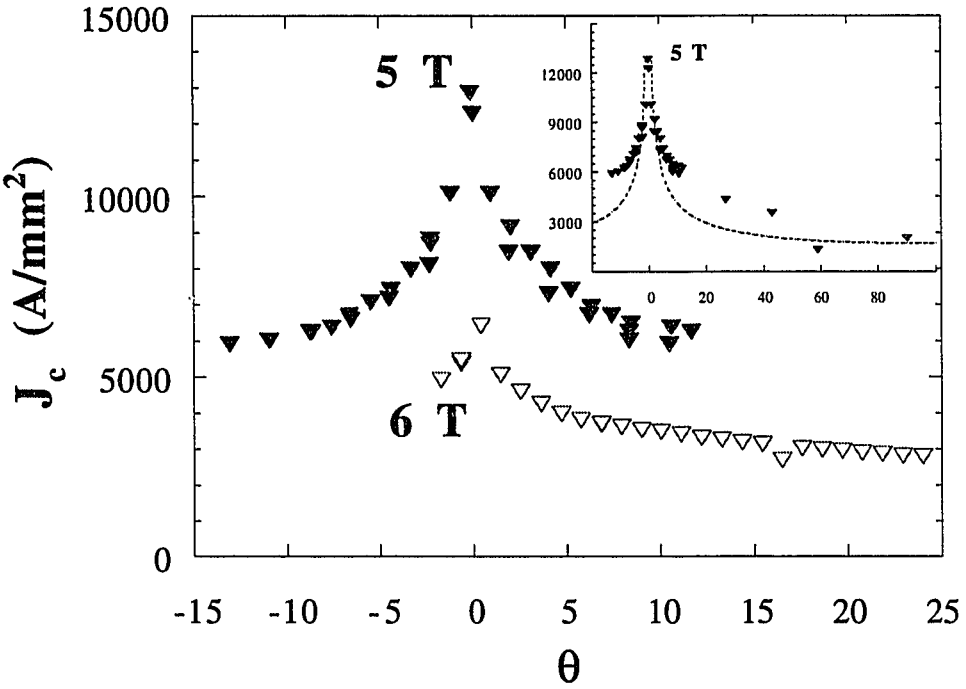

Figure 3.12. The angular dependence of J_C for [21/6] at 4.2 K and 5 and 6 T. The data were obtained *in situ*. The data have been shifted to place the maximum of J_C at 0°. Inset: the full angular range of data at 5 T with a fit to the functional form $J_C \sim 1/\sin^{1/2}\theta$.

3.5.1.3. Post-Computer DC Transport Measurements

Following the acquisition of a computer for dedicated data taking, we altered the measurement setup as follows: DC current bias to the sample was supplied by a

Yokogawa 7031 power supply; the voltage response was still measured by the Keithley 147 Nanovolt Null Detector, though its analog output was connected to an HP 34401 DMM. The Yokogawa power supply, the Lakeshore power supply (magnet current), and the two HP 34401 DMMs (thermometer voltage and nanovoltmeter analog output) were all controlled by an Apple IIsi computer, running a program written with National Instruments' LabVIEW 2.2.1. This setup is shown in Fig. 3.10. Voltage noise levels were reduced to below 50 nV by averaging as many as 25 voltage measurements per current point. The temperature was still manually adjusted during these measurements

3.5.2. Critical Temperature Measurements—AC Transport

We measured the small-signal AC resistance of our samples as a function of applied magnetic field B, temperature T, and sample orientation θ: $R(B, T, \theta)$. The critical temperature $T_c(B,\theta)$ was defined as the temperature where the sample resistance first reached 1/2 the normal state resistance just above the transition R_n. The AC current was always applied perpendicular to the field B. We determined the upper critical field $H_{c2}(T, \theta)$ by fixing the field and angle θ and sweeping the temperature: transitions were measured both for T increasing and decreasing. The data were not used unless the hysteresis was minimal (< 25 mK). This generally meant that the heating or cooling rate near the transition was below ~ 25 mK/s. Measurements of T_c were also not made if the partial pressure of He in the cryostat was above 10 mTorr—higher gas pressures provide too strong a thermal link to the bath.

3.5.2.1. Errors

The inaccuracies of the temperature and field measurements have a number of sources—some have been referred to already, like the offset caused by the thermal leak of the worm gear (see Appendix C) and the magnet inhomogeneity ($\Delta B/B$ ~ 2.5%). Because of the CG sensor's magnetoresistance, the inferred temperature change in a field is ~

1.5%. Additionally, human measurement errors on the recorder paper contribute ~ 1%, for a total $\Delta T/T$ ~ 1.6%.

3.5.2.2. AC Transport Setup

We measured the sample's resistance with a Princeton Applied Research 124 lock-in amplifier. The lock-in's reference channel was used to supply the excitation current of 1 μA (calibrated 100 mV across a 100.3 kΩ resistor) at 22 Hz. This corresponds to a measurement current density of ~ 1 A/mm^2. The in-phase voltage was measured with the signal channel, with a 10% equivalent noise bandwidth and a time constant of 300 ms. The analog output of the PAR 124 was connected directly to an HP7047A x-y recorder. We measured the temperature as above, with the voltage from the thermometer box connected directly to the HP7047A. Heating and cooling were controlled manually with the internal 15 V supply of the thermometer box. This setup is shown schematically in Fig. 3.11.

3.6. Microstructural Characterization

We tried to determine the microstructure of our MLs with a number of standard techniques: atomic force microscopy (AFM), x-ray diffractometry (XRD), and transmission electron microscopy (TEM). Of the three techniques, XRD is the most widespread in characterizing layered superconductor systems [Koorevaar (93), Nojima (93), Jin (89), Ruggiero (80)], and yields the basic information about the true layer thicknesses and crystalline order most quickly. TEM can give a direct image of both the layer thicknesses and the grain sizes with nearly atomic resolution, though sample preparation is complicated. AFM yields only information about the surface, though at atomic resolution—there is essentially no sample preparation necessary.

To summarize the results of our various investigations, our multilayers are polycrystalline with a grain size ~ 50 nm. There is evidence for some interdiffusion (~ 1

nm) at the boundaries between the Nb and $Nb_{0.37}Ti_{0.63}$ layers from the electrical transport measurements in Ch. 5.—the relatively small grain size (compared to bulk) of the films may allow stronger interdiffusion [D. Dietderich, personal communication] than would be naively expected from bulk results [Taillard (93)]. We discuss these conclusions below.

3.6.1. Atomic Force Microscopy

An AFM is essentially a profilometer with sub-nm resolution [Rugar (90), Wickramasighe (89)]. It achieves this resolution by reading the position of a very fine tip with a laser. AFM yields information only about the surface properties of a sample but, when corroborated with other techniques, is a useful and fast tool for microstructural characterization.

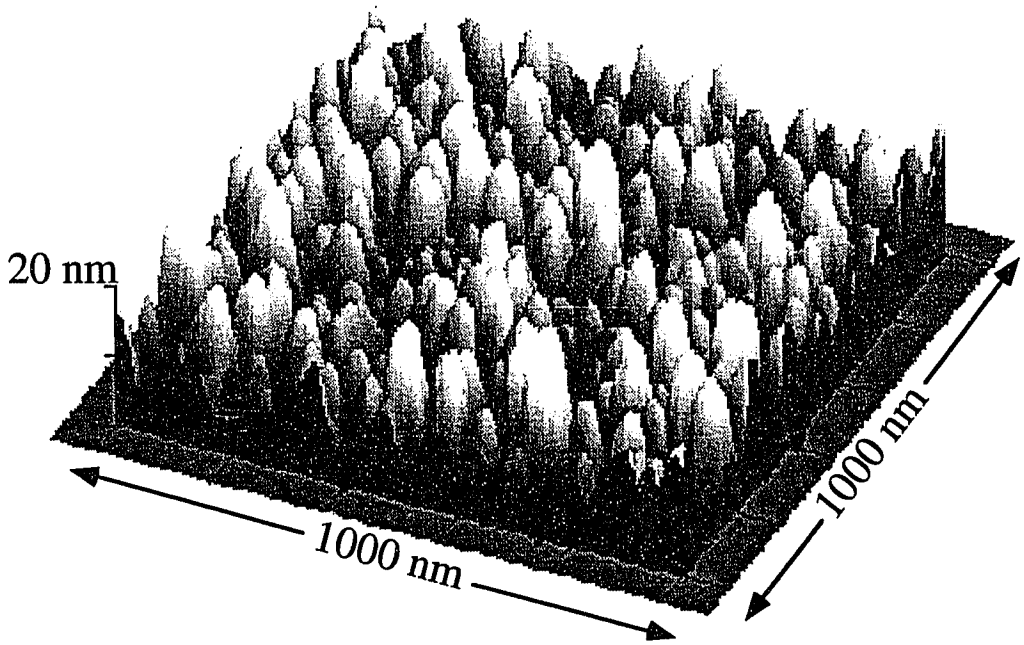

Figure 3.13. AFM image of [21/6]. The vertical scale has been greatly exagerated compared to the horizontal scales: the average surface roughness is ~ 5 nm RMS, the grain size is between 25 and 50 nm.

AFM measurements were carried out on two MLs, [21/6] and [21/8], at Yale by Dr. M. Amman. There were no general differences detected between the surface properties of the two. Fig. 3.13. is a typical image of a 1 μm by 1 μm section of [21/6]. It shows the grain structure at the surface clearly—the average grain size is ~ 50 nm in diameter. The RMS roughness is ~ 5 nm. We believe this roughness is a result of the growth of grains (which grow in columns, near normal to the substrate [Stejic (94), Kumar (94)]) and not due to the roughness of the Si (100) substrate. The RMS roughness of our Si substrates is under ~ 0.25 nm [Anderson (93)].

3.6.2. X-Ray Diffractometry

XRD is a standard thin film characterization technique. The article by Jin and Ketterson (89) provides an excellent overview. A collimated x-ray beam (typically Cu Kα, $\lambda_{CuK\alpha} = 0.154$ nm) is directed at the sample. The photons diffracted by the sample are collected by an angle-sensitive detector. The peaks in diffraction intensity are governed by Bragg's Law: $n\lambda = 2d\sin\theta$, where n is an integer, λ is the x-ray wavelength, d is the spacing between atomic planes, and 2θ is the scattering angle in the plane of the source and detector. At the most basic level, XRD may be used to determine the lattice constants (the d's may be extracted because λ and θ are known) and crystal structures (determined by which d's are *not* observed) of the constituents of a ML. Bragg's law applies equally well to the planes defined by the layers themselves—thus the modulation period Λ may also be directly measured. In an ideal sample (many sharply-defined layers without disorder), the diffraction pattern will be the superposition of the superlattice peaks (Bragg scattering off the layers) and the normal crystal structure peaks.

In a real material, a number of corrections must be made to arrive at a picture closer to the truth: we must take account of the non-uniformities [Fujii (86), Fantner (85)] and finite thicknesses of our MLs, as well as the absorption of diffracted x-rays at low angles.

3.6.2.1. Correction Factors

We first examine the effect of a random distribution of modulation periods Λ. This can be considered as statistically equivalent to the Debye-Waller effect [Jin (89)]—thermal vibrations of atomic layers at finite temperatures reduce the diffracted intensity from those planes. If Λ has gaussian fluctuations about its mean, with standard deviation σ, Fujii *et al.* (86) obtained an expression for the superlattice peak intensities:

$$I_s(s) = \frac{[1 - e^{-N\sigma^2\pi^2 s^2}]^2 + 2e^{-N\sigma^2\pi^2 s^2} \sin^2(N\Lambda\pi s)}{[1 - e^{-\sigma^2\pi^2 s^2}]^2 + 2e^{-\sigma^2\pi^2 s^2} \sin^2(\Lambda\pi s)}, \qquad (3.1.)$$

where $s = (2\sin\theta)/\Lambda$ and N is the number of modulation periods. This function falls off rapidly with increasing s. Therefore, in a sample with large σ, the superlattice peaks will only be observable for small θ.

A sample with random orientation of grains and small grain sizes can be viewed (in the extreme limit) as amorphous for the purposes of x-ray scattering. For an amorphous material, Jin and Ketterson [89] find for the superlattice intensities that

$$I_s(s) \propto \frac{1}{\pi^2 s^2}. \qquad (3.2.)$$

So, in a sample which is strongly disordered, again, the superlattice peaks will only be observed for small θ.

The effect of the finite thickness of any layer or thin film is to broaden the line width of the diffracted peak—the thicker the layer, the sharper the peak. The full width at half-maximum of the diffracted peak goes as $1/nd$, where n is the number of layers and d is their thickness [Jin (89)].

It is readily shown that if a material of thickness t has an x-ray absorption constant μ, then the intensity of both the superlattice peaks and the crystal structure peaks is reduced by a factor

$$f = (1 - e^{-\frac{2\mu t}{\sin\theta}})^{-1}. \qquad (3.3.)$$

This reduction factor is largest for small θ—the distance the x-rays must travel through a layer increases as $1/\sin\theta$.

3.6.2.2. XRD Results

XRD was performed on a number of samples in a number of labs both at Yale and elsewhere. [10/19] was measured by Dr. J. Talvacchio at the Westinghouse Science and Technology Center in Pittsburgh. [21/6] and [21/8] were measured with Prof. H. Wyckoff at the Center for Structural Biology at Yale. Additionally 94-5, a 10 period 7 nm Nb/4 nm Ti ML with 5 nm buffer and cap layers (created expressly for XRD diffraction studies), was measured by Y. Lu at the Department of Physics of Brown University.

Fig. 3.14. is a plot of the diffracted intensity versus 2θ for [10/19]. It shows clearly 4 peaks: 2 from the Si substrate one from the Al mask/contact layer and one combined peak from Nb and $Nb_{0.37}Ti_{0.63}$. They are identified (left to right) as Si (002), Nb (110) plus $Nb_{0.37}Ti_{0.63}$ (110), Al (200), and Si (004). The combined peaks of Nb (100) and $Nb_{0.37}Ti_{0.63}$ (110) occur at $2\theta = 38.7°$, which corresponds to a lattice constant of 0.329 nm, which is between the bulk values a_{Nb} = 0.330 nm [Jin (89), Qian (82)] and a_{NbTi} = 0.328 nm [Moffat (85)].

Fig. 3.14. does not show any indication that [10/19] is epitaxial to the substrate (higher order Nb or $Nb_{0.37}Ti_{0.63}$ peaks). Additionally, rocking curve widths of the Nb-$Nb_{0.37}Ti_{0.63}$ (110) peak were taken—again, there was no indication of epitaxy. These conclusions were also reached for samples [21/6] and [21/8] measured at Yale, though the

diffractometer used to measure them was not well suited to thin film analysis and no quantitative data were recorded. It is likely that the films are textured to the substrate, with the (110) plane of the bcc lattice oriented parallel to the surface—films deposited at low temperatures (compared to the melting point) tend to form close packed structures [Ahuja (94), Lowe (84)]. This conclusion is consistent with our XRD and TEM (see Ch. 3.6.3.) data and would be in line with the results of other workers [Jin (85), Lowe (84), Qian (82)].

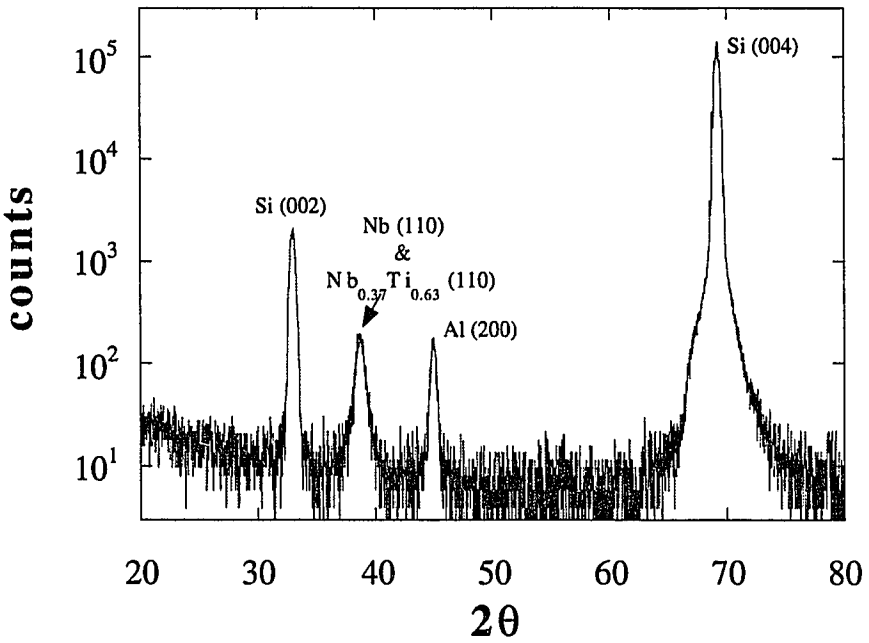

Figure 3.14. Standard θ-2θ scan of [10/19]. Counts vs. Bragg scattering angle 2θ. The four peaks are identified as Si (002) at 33°, Nb (110) plus $Nb_{0.37}Ti_{0.36}$ (110) at 38.7°, Al (200) at 45.0°, and Si (004) at 69.2°.

The data taken at Brown on 94-5, an 11 period 7 nm Nb/4 nm Ti ML with 5 nm buffer and cap layers, show superlattice peaks, though not many. The low angle data are presented in Fig. 3.15. A beam stop prevents measurements below $2\theta \approx 0.5°$. Two superlattice peaks are clearly seen at 0.85° and 1.71°. This spacing between maxima corresponds to a real-space Λ of 10.2 nm. The nominal Λ from deposition rates is 10.6

nm. That these two numbers agree so well may be coincidence—one would like to see many well-defined superlattice peaks for best comparison—but the measurement of the superlattice reflections for 94-5 is in line with the findings of other groups [Nojima (93), Jin (89), Lowe (84), Banerjee (82), Ruggiero (80)] that sputter deposition rates are usually a reliable measure of the actual ML period Λ.

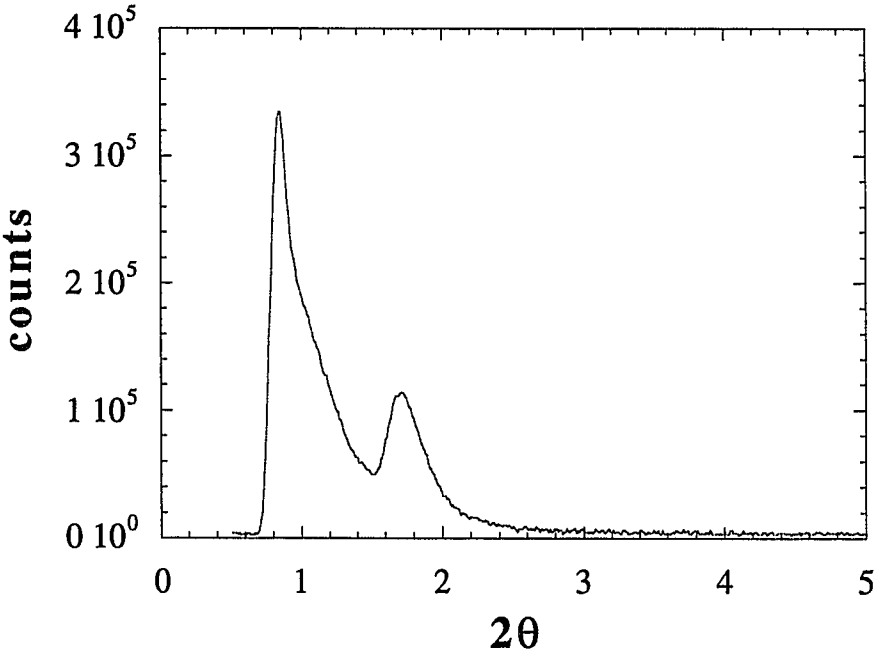

Figure 3.15. Small angle θ-2θ scan of sample 94-5 (11 period 7 nm Nb/4 nm Ti). Two superlattice peaks are seen at $2\theta = 0.85°$ and 1.71°, yielding a multilayer period of 10.2 nm, close to the estimated period of 10.6 nm.

3.6.2.3. Discussion of XRD Results

All of the data above lead us to the conclusion that our as-deposited MLs are not particularly well suited to XRD characterization, for a number of reasons. Chief among which are the few number of periods and their relatively long length. Most XRD studies are done on samples with upwards of 50 periods, which are typically less than 10 nm thick each [see for example Jin (89), Lowe (84)]. A sample with few periods will have correspondingly low, broad superlattice peaks, as discussed in section 3.6.2.1. This,

combined with the reductions in superlattice peak intensities from small variations in the ML period Λ caused by rate fluctuations and interdiffusion [Taillard (93), D. Dietderich (private communication)], might explain why we have not seen superlattice satellite peaks at large θ. The long length of our Λ probably causes absorption problems at small θ (the thick Nb cap layer, which is necessary for flux pinning measurements, only exacerbates the problem). Cu Kα x-rays have a penetration length in Nb of ~ 2 μm [see Ashcroft (76)]. This seems long, compared to the thickness of our samples (~ 0.3 μm), but at $\theta = 5°$, the *effective* thickness of our samples is ~ 3.5 μm—explaining why few low angle superlattice peaks were observed.

3.6.2.4. Other Groups' Multilayers

Our MLs differ from those of the closest competitors in substrate choice and deposition temperature. We deposited Nb and $Nb_{0.37}Ti_{0.63}$ on oxidized and unoxidized Si (100) at ~ 255°C, producing a polycrystalline, possibly (110) textured, film. The group at Chiba University [Nojima (93), Kuwasawa (90)] deposited Nb and $Nb_{0.5}Zr_{0.5}$ onto R-plane sapphire at 300 °C. XRD measurements on samples with small Λ (60 and 100 nm) showed well-defined superlattice peaks and a (110) texturing to the substrate. The group from Leiden University [Koorevaar (93), Maj (91), Aarts (90)] deposited Nb and $Nb_{0.6}Zr_{0.4}$ onto room temperature R-plane sapphire. They found texturing in the (110) direction. For long Λ samples (> 25 nm) they found no superlattice peaks, which they attributed to absorption and small scattering factor difference between Nb and Zr. For short Λ samples (< 8 nm) they did observe satellite superlattice peaks [see also Banerjee (82)].

Our problems with the full use of the x-ray diffraction technique are not unusual: our data are consistent with those of the workers above and confirm the reliability of our multilayer deposition methods.

3.6.3. Transmission Electron Microscopy

TEM is not as frequently used as the above methods for microstructural characterization because the sample preparation is difficult and destructive. In a transmission electron microscope, a beam of high energy electrons (> 100 keV) is shot through a very thin sample (~ 100 nm) [Ahuja (94), Hirsch (77)]. The electrons transmitted through the sample are detected and an image is formed, similar to a scanning electron microscope. The sample must be thin so that some of the high-energy electrons do not undergo too many collisions with the lattice as they pass through. TEM is capable of atomic resolution.

3.6.3.1. Results

K. Faase of Oregon State University took transmission electron micrographs of [27/9]. Dr. D. Dietderich at Lawrence Berkeley Laboratories took TEM images of [21/6] as well as a $Nb_{0.37}Ti_{0.63}$/Ti sample prepared expressly for TEM study (see Appendix C). Fig. 3.16. is composed of two bright field images of [27/9] taken at OSU. A bright field image is made by blocking out all the diffracted beams—dark regions are therefore where fewer electrons pass through. Fig. 3.16.a. was taken at relatively low magnification and shows almost the entire sample cross-section. Fig. 3.16.b. is a high magnification image taken near the center of Fig. 3.16.a.

The eleven $Nb_{0.37}Ti_{0.63}$/Nb bilayers are clearly resolved in Fig. 3.16.a. The Nb regions appear as dark bands. The less dense $Nb_{0.37}Ti_{0.63}$ layers appear lighter by contrast. Image analysis performed at OSU yields an average bilayer thickness of 32 nm, in good agreement with the nominal period (determined by sputter-deposition rates) of 36 nm. The images of [21/6] taken at LBL (not shown) also confirm the reliability of the deposition rates as measures of the multilayer period. The higher magnification image (Fig. 3.16.b.) shows evidence for columnar growth perpendicular to the substrate. Small

Area electron Diffraction (SAD) performed on [27/9] at OSU suggests further that the film is a strained bcc lattice with a predominantly <110> orientation in the growth direction. This agrees with the conclusions drawn from the XRD measurements above.

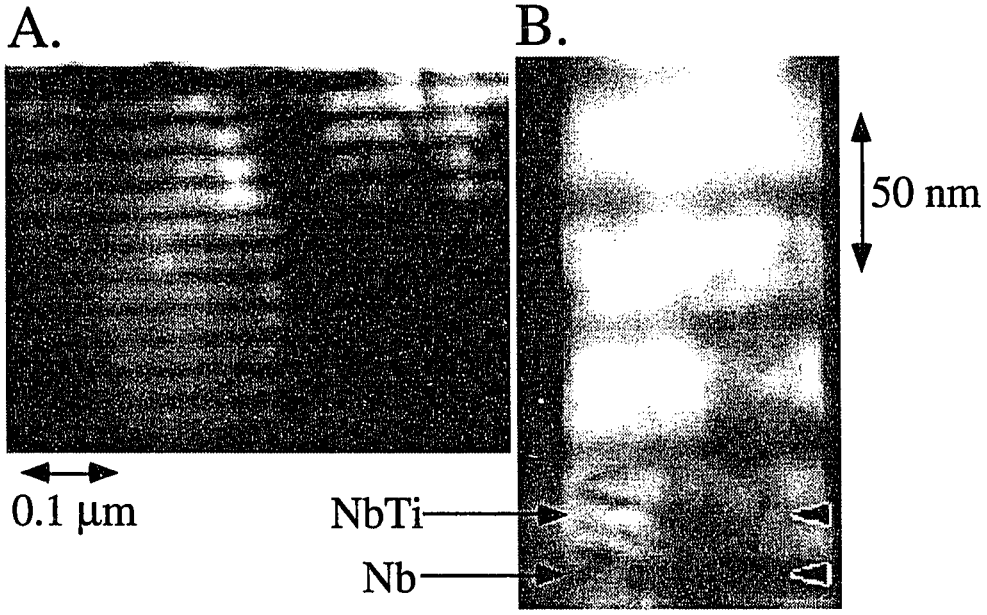

Figure 3.16. Transmission electron micrographs of [27/9]. A) bright field image at 100 000 x magnification, showing the whole multilayer cross-section, excluding Nb buffer and cap layers. B) bright field image at 2 000 000 x magnification. The dense Nb layers are dark in these images.

Chapter 4. Basic Superconducting Properties

The basic superconducting properties, T_c and $H_{c2}(\theta)$, of all-metallic multilayers have been studied in depth since the early 1980s [Maj (91), Aarts (90), Kuwasawa (90), Karkut (88), Obi (87), Kanoda (86), Banerjee (82)]. The study of layered superconducting systems, both artificial [see Jin (89) for an extensive review] and naturally-occurring [see Beasley (80) for a review of the layered chalcogenides], has an even longer history. The behavior of T_c and $H_{c2}(\theta)$ are fairly well understood, both within the phenomenological theory of Ginzburg and Landau [Jin (89), Collings (86), Tinkham (80), Klemm (75)] and the microscopic theory [Takahashi (86b, 86a)]. Although our main focus in this work is on the flux pinning properties of layered superconducting systems, information gleaned from the more basic measurements sheds light on them as well, as they are not totally separate entities.

4.1. Nb and $Nb_{0.37}Ti_{0.63}$

We made measurements on thick films of $Nb_{0.37}Ti_{0.63}$ and Nb prepared under the same conditions as our MLs, to provide baselines for the various electrical and superconducting properties of the constituent layers.

4.1.1. Zero Field Properties

We measured the normal state resistivity (DC and AC) of the single films at room temperature and just above T_c—the residual resistivity ratio ($RRR = \rho_n(300\ K)/\rho_n(\sim T_c)$) provides a useful gauge of the film quality. The low temperature resistivity is determined by lattice defects and other inhomogeneities (i.e., the mean free path ℓ) [Ashcroft (76)]. Many parameters of the GL and microscopic theories can be related to $\rho_n(\sim T_c)$. We

monitored the small-signal AC resistivity to determine T_c, which is also a measure of the film quality. As noted earlier, in the case of NbTi alloys, T_c can be depressed when O or N are incorporated into the lattice [Collings (83)]. A summary of the zero-field properties of our Nb and $Nb_{0.37}Ti_{0.63}$ is given in Table 4.1.

Table 4.1. The zero-field properties of Nb and $Nb_{0.37}Ti_{0.63}$[a]

Material	T_c (K)	ρ_n (μΩcm)	*RRR*
Nb	9.21(5)	10(1)	6.2(6)
$Nb_{0.37}Ti_{0.63}$	8.48(4)	74(7)	1.2(1)

[a] errors or uncertainties in last digit indicated by quantity in parentheses

Our Nb films are comparable to those of other workers prepared under similar conditions [Gaidis (94), Kuwasawa (90), Karkut (88)]. Likewise, the critical temperature of $Nb_{0.37}Ti_{0.63}$ is in line with the thin film measurements of others (T_c ~ 8.4 K) [Stejic (94), Obi (87), Jin (85)], but is depressed from the bulk value (T_c ~ 9 K), probably because of O and N contamination during growth. The zero-field transitions of both films had a width ΔT_c ~ 30 mK.

The normal state resistivity of Nb above T_c and its *RRR* are also comparable to the thin film results of others [Gaidis (94), Banerjee (82)]. The film value of ρ_n is higher than that of the bulk because of the shorter ℓ. The properties of $Nb_{0.37}Ti_{0.63}$ are not too different between thin film and bulk [Stejic (94), Cooley (93), Meingast (89)], because it is a dirty alloy. Using $(\rho\ell)_{Nb} = 1.5 \times 10^{-15}$ Ωm [Banerjee (82)], we obtain ℓ_{Nb} ~ 15 nm. From Collings [86], we find ℓ_{NbTi} ~ 0.5 nm.

4.1.2. Upper Critical Fields

We measured the perpendicular upper critical fields $H_{c2}(\theta = 90°)$ of the thick single films to obtain the various GL superconducting quantities, without the interference of surface effects (like H_{c3}). In Fig. 4.1. we plot the resistively-measured $H_{c2}(90°, T)$ of Nb and $Nb_{0.37}Ti_{0.63}$. We also measured the near-parallel ($\theta = 5.4°$) upper critical fields,

to assess the effects of surface superconductivity and possible anisotropies in behavior caused by the columnar growth of grain boundaries [Stejic (94), Kumar (94)]. Fig. 4.2. is a plot of $H_{c2}(T)$ of $Nb_{0.37}Ti_{0.63}$ at $\theta = 5.4°$ and 90°. The perpendicular upper critical field of our sample lies above the near-parallel H_{c2}—this (seemingly) surprising phenomenon is not unknown in thin film measurements of Nb alloys [Ashkin (84, 78)]. Stejic *et al.* [94] found similar results when the thickness of their NbTi films exceeded the magnetic penetration depth λ, as ours do.

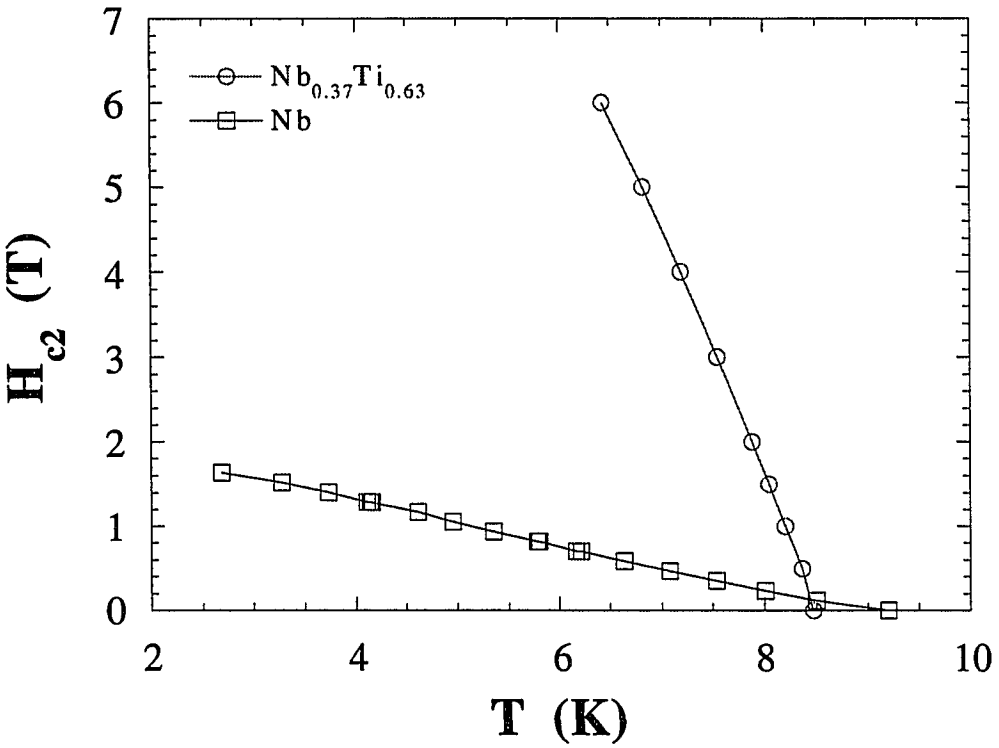

Figure 4.1. $H_{c2}(90°, T)$ of thick (~ 200 nm) Nb and $Nb_{0.37}Ti_{0.63}$ films.

This reversal of the more usual behavior of the upper critical fields can occur in films with anisotropic pinning; resistively-measured critical temperatures effectively measure the critical current I_c of the sample as a function of T. If the flux pinning properties are anisotropic (as in the case of a film with columnar grain boundary growth), the resistively-measured H_{c2} will reflect those anisotropies. As we shall see (see Fig.

5.1.), $J_c(\theta = 90°)$ *is* greater than $J_c(\theta = 5.4°)$ for our $Nb_{0.37}Ti_{0.63}$. In thick Nb films, we see little or no anisotropy in the upper critical fields or critical currents, presumably because of the much weaker pinning in Nb.

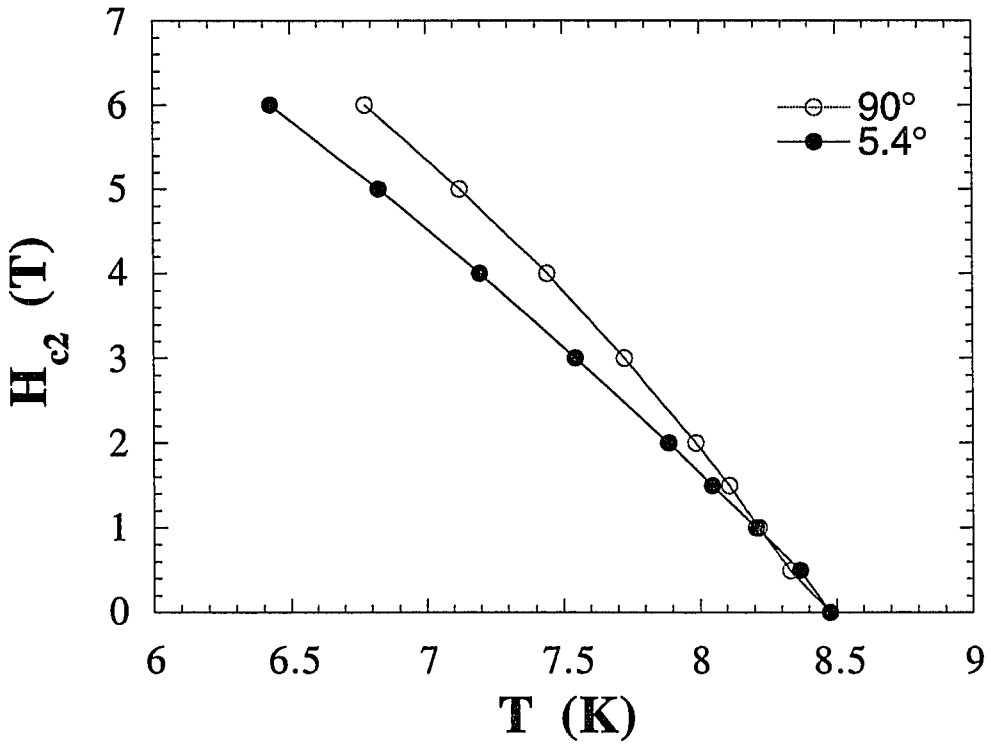

Figure 4.2. $H_{c2}(T)$ of thick $Nb_{0.37}Ti_{0.63}$ film at $\theta = 90°$ (field parallel to growth direction) and $\theta = 5.4°$ (field near perpendicular to growth direction).

Table 4.2. summarizes the superconducting properties of Nb and $Nb_{0.37}Ti_{0.63}$ extracted from the perpendicular upper critical field data. The same quantities from the θ = 5.4° data are presented in Table 4.3. We calculated the zero-temperature upper critical field using the microscopic result of Werthamer *et al.* [66]:

$$h^* = H_{c2} \Big/ -\frac{dH_{c2}}{dt}\Big|_{t=1}, \tag{4.1.}$$

where $t = T/T_c$ and $h^* = 0.68$ in the absence of paramagnetic limiting and spin-orbit scattering. Werthamer *et al.* [66] found a value of $h^* \approx 0.6$ for the data of Shapira and

Neuringer [65] on bulk $Nb_{0.44}Ti_{0.56}$. We will use this value of h^* to analyze our $Nb_{0.37}Ti_{0.63}$ data. The GL coherence length was found from a least-squares linear fit to H_{c2} vs. 1-t for $t \sim 1$ (see Eq. 4.5.). The dirty-limit GL κ parameter is calculated by combining two well-known equations, given by Collings [86]:

$$\kappa_{GL} = 7.49x10^3 \rho_n \gamma^{1/2}, \tag{4.2.}$$

$$-\left.\frac{dH_{c2}}{dT}\right|_{T_c} = 4.49x10^4 \rho_n \gamma, \tag{4.3.}$$

where both equations are in cgs units and γ is the electronic specific heat coefficient per unit volume. Solving Eq. 4.3. for γ and substituting into Eq. 4.2., we obtain

$$\kappa_{GL} = 35.4\sqrt{-\rho_n \left.\frac{dH_{c2}}{dT}\right|_{T_c}}, \tag{4.4.}$$

where the effects of Pauli paramagnetic limiting and spin-orbit coupling have been ignored in Eq. 4.2-4.

Table 4.2. Superconducting parameters from $H_{c2}(90°, T)$

Material	$-\left.\frac{dH_{c2}}{dT}\right\|_{T_c}$ (T/K)	$H_{c2}(0)$ (T)	$\xi_{GL}(0)$ (nm)	κ_{GL}
Nb	0.25(1)	2.0(2)[a]	12.3(6)	5.6(6)
$Nb_{0.37}Ti_{0.63}$	3.7(2)	19(2)	3.3(2)	58(7)

[a] linear extrapolation from 2 K

Table 4.3. Superconducting parameters from $H_{c2}(5.4°, T)$

Material	$-\left.\frac{dH_{c2}}{dT}\right\|_{T_c}$ (T/K)	$H_{c2}(0)$ (T)	$\xi_{GL}(0)$ (nm)	κ_{GL}
$Nb_{0.37}Ti_{0.63}$	3.1(1)	16(2)	3.6(2)	53(6)

The extrapolated zero temperature upper critical fields of both Nb and $Nb_{0.37}Ti_{0.63}$ are close to those of heavily cold-worked bulk samples [Collings (83), Qian (82)]. The value of H_{c2} of Nb is slightly enhanced over bulk, because of the shorter ℓ.

The GL parameters are likewise within the range of bulk values, considering the short ℓ of our Nb film and the slightly depressed T_c of our $Nb_{0.37}Ti_{0.63}$. We find the GL penetration depths $\lambda(0) = \kappa(0)\xi(0)$ are 182 nm for $Nb_{0.37}Ti_{0.63}$ and 65 nm for Nb.

4.2. Multilayers

We measured the basic superconducting properties of our MLs to obtain a better understanding of the behavior of ψ_{GL} in a two-component superconducting system and its implications for the flux pinning properties. We will begin with a discussion of the behavior of T_c as the structure changes.

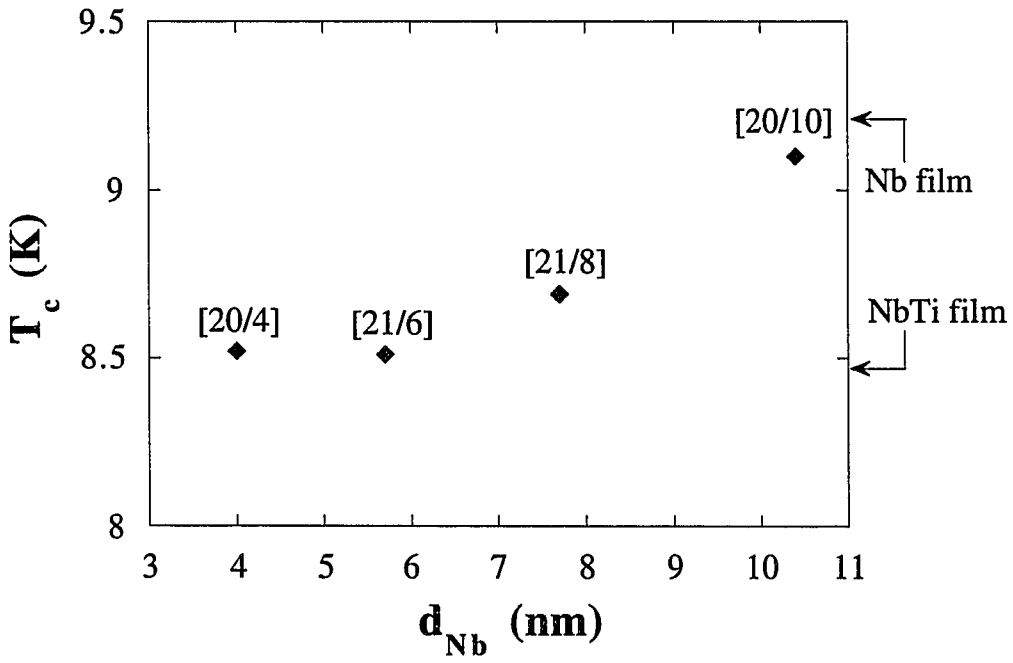

Figure 4.3. Critical temperature in ambient field vs. Nb layer thickness of multilayer samples with near constant $Nb_{0.37}Ti_{0.63}$ thickness (≈ 20 nm). The critical temperatures of thick (bulk-like) Nb and $Nb_{0.37}Ti_{0.63}$ films are indicated at left.

4.2.1. The Zero Field Critical Temperature

The behavior of the zero field critical temperature of a superconducting metallic bilayer, or the equivalent problem of the T_c of an ML, has been studied in depth both theoretically [ChenJ (90), Takahashi (86a), deGennes (64), Werthamer (63)] and experimentally [Obi (87), Lowe (84), Banerjee (82), Qian (82)]. In Fig. 4.3. we present T_c as a function of d_{Nb} for our MLs with fixed d_{NbTi} ($\approx$ 20 nm). As expected from both the TT and GL theories (see below), T_c of the MLs varies smoothly between the values of the component layers—as more vol.% Nb is added, T_c approaches that of a thick Nb film.

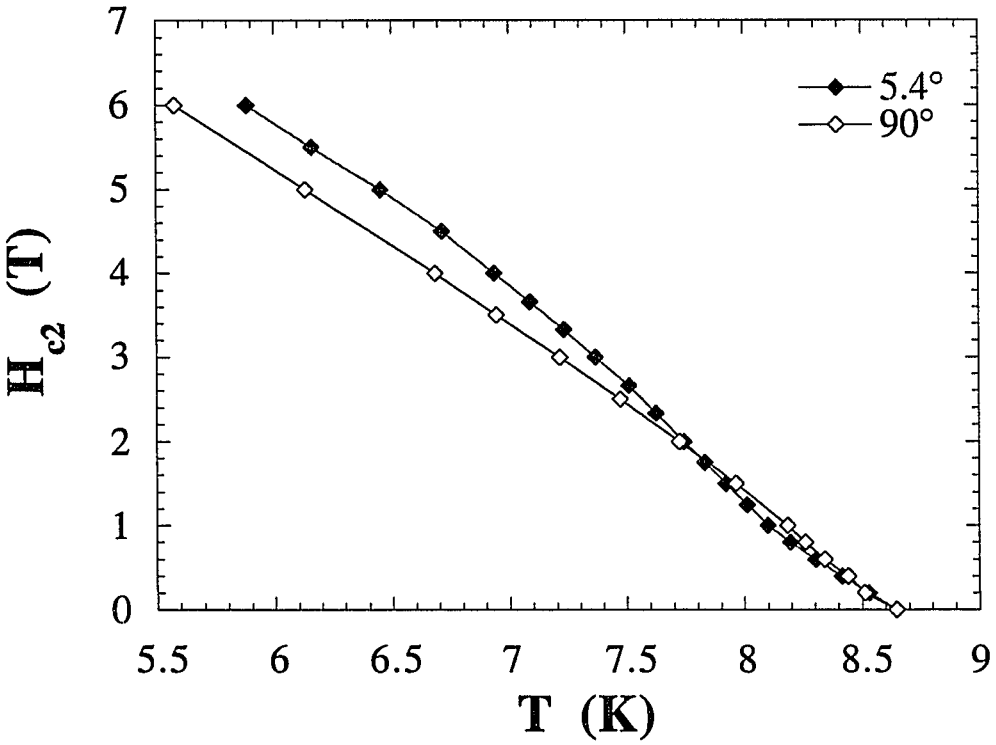

Figure 4.4. $H_{c2}(5.4°, T)$ and $H_{c2}(90°, T)$ for [21/8]. $\theta = 90°$ shows expected behavior. $\theta =$ 5.4° shows 3D to 2D dimensional crossover near $T \approx 8.2$ K.

4.2.2. Upper Critical Fields

We concentrated mainly on $H_{c2}(\theta = 5.4°)$ for the MLs, though we did take $H_{c2}(\theta = 90°)$ measurements for samples [20/4], [21/6], and [21/8]. We plot $H_{c2}(5.4°, T)$ and $H_{c2}(90°, T)$ for sample [21/8] in Fig. 4.4. We notice immediately that there is a difference between the two orientations: the near parallel data is higher at low temperatures and has a slight "kink" (a change in slope) near $T \approx 8.2$ K. This kink is typical of a dimensional crossover, which will be investigated more fully below. The low temperature ratio of $H_{c2}(5.4°)/H_{c2}(90°)$ was below 1.1 for all three samples. This indicates that our multilayers are strongly coupled (in the temperature range to which we have access, which is limited by the highest field we can attain ~ 6 T) as far as the microscopic quantities are concerned. We look at the effect of these small anisotropies in the next few sections.

4.2.2.1. Anisotropic Ginzburg-Landau Theory

In an isotropic superconductor, the upper critical field is given by in the GL theory as

$$H_{c2}(T) = \frac{\Phi_0}{2\pi\xi^2(T)} = \frac{\Phi_0}{2\pi\xi^2(0)}\left(1 - \frac{T}{T_c}\right). \tag{4.5}$$

What happens when the superconductor is a multilayer? Lawrence and Doniach [71] were the first to consider this question theoretically, though others followed soon after [Klemm (75)]. They used the GL formalism to consider a stack of 2D superconducting layers of neglible thickness coupled by Josephson tunneling. The first GL equation for the nth layer then becomes:

$$\alpha\psi_n + \beta\psi_n|\psi_n|^2 + \left[\frac{\hbar}{i}\nabla_{xy} + 2e\vec{A}\right]^2\psi_n + \eta(\psi_{n-1} - 2\psi_n + \psi_{n+1}) = 0, \tag{4.6.}$$

where η is the coupling coefficient between layers. The z direction is perpendicular to the layers. If η is sufficiently large (the strong coupling limit), we may rewrite Eq. 4.6. using an effective mass tensor:

$$\alpha\psi+\beta\psi|\psi|^2+\left[\frac{\hbar}{i}\nabla+2e\vec{A}\right]\cdot\frac{1}{2\tilde{m}}\cdot\left[\frac{\hbar}{i}\nabla+2e\vec{A}\right]\psi=0, \tag{4.7.}$$

where ψ is now three dimensional. The effective mass tensor is diagonal:

$$\tilde{m}=\begin{bmatrix} m & 0 & 0 \\ 0 & m & 0 \\ 0 & 0 & M \end{bmatrix}. \tag{4.8.}$$

The effective mass in the x-y plane of the layers is m; the effective mass in the z direction is $M \propto \eta^{-1}$. To find the upper critical field, we solve for the eigenvalues α of Eq. 4.7., using $\psi \rightarrow 0$ which allows us to neglect the term in $|\psi|^2$. The solutions have the familiar GL form for fields applied perpendicular and parallel to the layers:

$$\begin{aligned} H_{c2}(90°,T) &= \frac{\Phi_0}{2\pi\xi_\perp{}^2(T)} \\ H_{c2}(0°,T) &= \frac{\Phi_0}{2\pi\xi_\perp(T)\xi_{||}(T)} \end{aligned}, \tag{4.9.}$$

where

$$\begin{aligned} \xi_\perp{}^2(T) &\equiv \frac{\hbar^2}{2m|\alpha(T)|} \\ \xi_{||}(T) &\equiv \sqrt{\frac{m}{M}}\xi_\perp(T) \end{aligned}. \tag{4.10.}$$

We see immediately that $H_{c2}(0°)$ will be larger than $H_{c2}(90°)$, the ratio being equal to $(M/m)^{1/2}$.

Klemm *et al.* [75] considered the case of arbitrary coupling strength η. They confirmed the Lawrence-Doniach model in the strong coupling limit, but found new

results in the intermediate regime. Near T_c, the coherence length ξ is long enough to extend over many layers, giving strong coupling. As we move further below T_c, ξ shrinks rapidly. Soon ξ is of order the interlayer distance s or smaller. When this occurs, the layers are no longer strongly coupled, since the overlap of the order parameter on adjacent layers $<\psi_n|\psi_{n+1}>$ will be small—if the individual layers are thinner than ξ they will behave quasi-two-dimensionally. In this regime, the parallel upper critical field has the form:

$$H_{c2}(0°,T) = H_{c2D}(0)\sqrt{1-T/T_{3D-2D}}\,, \tag{4.11.}$$

where

$$H_{c2D}(0) = \frac{\sqrt{12}\Phi_0}{2\pi\xi_\perp(0)d}, \tag{4.12.}$$

and d is the layer thickness and $T_{3D\text{-}2D}$ is the temperature at which $\xi \approx s/\sqrt{2}$.

This is the well-known 3D to 2D dimensional crossover: near T_c, the behavior of the sample is bulk-like and $H_{c2} \propto (1\text{-}t)$. When the layers decouple, the sample's behavior is quasi-2D and $H_{c2} \propto (1\text{-}t)^{1/2}$. The above results only hold quantitatively for a multilayer which is well-modeled by a stack of thin superconductors coupled by tunneling. For all-metallic MLs like ours, we must turn to the microscopic theory for results which are quantitatively correct, although the results of the anisotropic GL theory still provide good guidance in understanding the behavior of anisotropic metallic multilayers.

4.2.2.2. Takahashi-Tachiki Theory of the Upper Critical Field

Most of the microscopic treatments of the upper critical field [Jin (89)] are based on the linearized self-consistent field method [deGennes (64), Werthamer (63)]. They start with a linearized equation for the pair potential Δ in a superconductor due to Gor'kov [60]:

$$\Delta(\vec{r}) = V(\vec{r}) k_B T \sum_{\omega} \int d^3\vec{r}' \, Q_\omega(\vec{r},\vec{r}') \Delta(\vec{r}'), \tag{4.13.}$$

where V is the electron pairing interaction, $\omega = (2l+1)\pi k_B T$ are the Matsubara frequencies, and the kernel is defined

$$Q_\omega(\vec{r},\vec{r}') = \sum_{n,m} \frac{\phi_m^*(\vec{r}')\phi_n^*(\vec{r}')\phi_m(\vec{r})\phi_n(\vec{r})}{(\xi_m + i\hbar\omega)(\xi_n + i\hbar\omega)}. \tag{4.14.}$$

The wavefunctions ϕ_m and their eigenenergies ξ_m are solutions to the one-electron Hamiltonian in the normal state, which includes the effects of impurity and boundary scattering [deGennes (64)]. The problem of determining H_{c2} becomes the problem of finding Q_ω for the system under study and determining the highest temperature at which Δ is nonzero throughout the sample. The boundary conditions in the dirty limit were first given by deGennes [64] for the interface between metals 1 and 2:

$$\begin{aligned} \frac{\Delta_1}{N_1 V_1} &= \frac{\Delta_2}{N_2 V_2} \\ \frac{D_1}{V_1}\frac{d\Delta_1}{dx} &= \frac{D_2}{V_2}\frac{d\Delta_2}{dx} \end{aligned}, \tag{4.15.}$$

where N is the density of states at the Fermi surface, $D = (1/3)v_F\ell$ is the diffusion constant of the electrons, and V is the electron pairing interaction. Also

$$\frac{d\Delta}{dx} = 0 \text{ at a free surface.} \tag{4.16.}$$

Takahashi and Tachiki [86a] extended deGennes' self-consistent method to finite magnetic fields and applied it to dirty limit ($\ell < \xi_0$) MLs. Theirs is the most general treatment to date, because they allow for N, D, and V to vary spatially and independently of one another.

The application of the TT formalism requires extensive numerical analysis. It has not been used specifically to fit experimental data [Jin (89)] on the upper critical field,

though TT did carry out the computations in a number of illustrative cases, usually varying only one of the parameters N, V, or D, at a time. We can summarize their results simply: dimensional crossover similar to that predicted in the anisotropic GL formalism occurs for multilayers when any one of the above parameters varies between the constituent layers. The case which closely reflects our experiments on $Nb_{0.37}Ti_{0.63}$/Nb MLs is that in which the bulk critical temperatures of the two layers are equal, but the bulk upper critical fields are not. TT treated this case most extensively [Takahashi (86b,86a)].

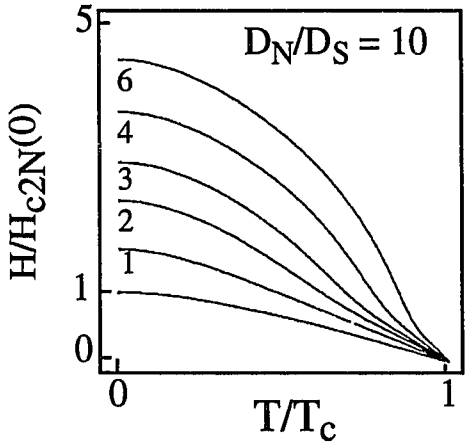

Figure 4.5. Calculated temperature dependence of the parallel ($\theta = 0°$) upper critical field of a metallic multilayer for different ratios of the bulk diffusion constants D. ($d_N = d_S = 0.75\ \xi_S(0), V_N = V_S$, and $N_N = N_S$.) For $D_N/D_S > 2$, $H_{c2}(0°)$ shows dimensional crossover. The fields are normalized to the bulk upper critical field of the N layer. Adapted from [Takahashi (86b)].

TT considered a ML with two superconductors: the clean, low diffusion constant, superconductor was referred to as the N layer, the dirty superconductor as the S layer. In Fig. 4.5. we plot their results for the parallel upper critical field of a multilayer $N_N = N_S$ and $V_N = V_S$ ($d_N = d_S = 0.75\ \xi_S(0)$) as a function of T/T_c and the ratio $D_N/D_S = H_{c2S}/H_{c2N}$. We see that as the layer anisotropy increases, the crossover from 3D to quasi-2D behavior is greatly accentuated. In a follow-up paper [Takahashi (86b)], they examined the behavior of multilayers where D_N/D_S and the layer thicknesses were

large—they found a *second* dimensional crossover was possible for some MLs. At the time, this second crossover had not been observed experimentally. (Experiments were later reported by a number of groups [Aarts (90), Kuwasawa (90), Karkut (88)].)

The second dimensional crossover (the Takahashi-Tachiki Effect) is shown in Fig. 4.6. We plot the TT results for the parallel upper critical field of a multilayer with $d_N = d_S = \xi_N(0)$ and $N_N = N_S$ and $V_N = V_S$. For small values of D_N/D_S the results are no different from Fig. 4.5. In Fig. 4.5. the layers are fairly thin—below the zero temperature GL coherence length in either material. In Fig. 4.6. the layers are much thicker: when the critical ratio of D_N/D_S (which depends on the thicknesses of the layers) is exceeded, there is a sharp upturn in $H_{c2}(0°)$ at a temperature T^+. This critical ratio increases as the layer thickness decreases.

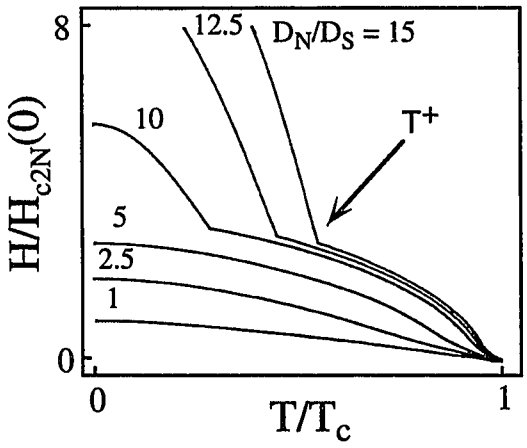

Figure 4.6. Calculated temperature dependence of the parallel upper critical field for a multilayer with $d_N = d_S = \xi_N(0)$. All other parameters identical to Fig. 4.5. At this thickness, the critical ratio of D_N/D_S to observe the second dimensional crossover (2D to 3D) is between 5 and 10. Adapted from [Takahashi (86b)].

Why is there a second dimensional crossover? When solving for the upper critical field of a multilayer, there is some ambiguity over where the order parameter first nucleates as the field drops below H_{c2}. By symmetry, Δ must have a maximum at the center of one of the layers, N or S. TT carried out the calculation of $H_{c2}(0°)$, allowing Δ to nucleate on the N or S layers and compared the resulting upper critical fields [see also

Dobrosavljevic (77), Ami (75)]. This is plotted in Fig. 4.7. for the sample with $d_N = d_S = \xi_N(0)$ and $D_N/D_S = 12.5$. The dashed curve is the upper critical field of the multilayer when Δ is centered in the N layers; the dash-dotted curve is when it is centered in the S layers. The observed H_{c2} is the higher of the two curves at any particular temperature.

The explanation underlying this behavior is very similar to the explanation of dimensional crossover in the anisotropic GL theory. At high temperatures, Δ extends over many layers, and the upper critical field reflects the 3D averaged behavior of the two component layers. As the temperature decreases, the coherence length decreases enough so that Δ may be localized primarily in the clean N layers, which then behave as "isolated" quasi-2D films. As the temperature is reduced still further, nucleation in the S layer becomes possible when the coherence length is of order the S layer thickness or smaller. At these temperatures and fields, Δ becomes localized in the S layer, but because $d_S > \xi_S$, the behavior of H_{c2} is bulk-like.

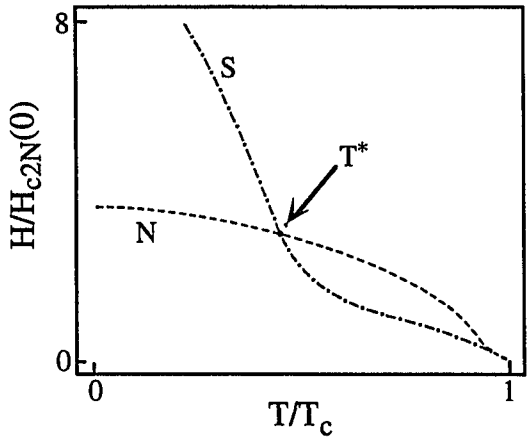

Figure 4.7. Temperature dependence of the parallel upper critical fields for $D_N/D_S = 12.5$ and $d_N = d_S = \xi_N(0)$. The dashed and dash-dotted curves indicate Hc2 when $\Delta(r)$ nucleates in the N and S layers respectively. The observable H_{c2} is the higher of the two. Adapted from [Takahashi (86b)]

4.2.2.3. Experimental Observation of Dimensional Crossover

The geometry of our multilayers was chosen to be similar to that of Artificial Pinning Center (APC) wires [Matsumoto (94), Cooley (93), Motowidlo (92)]—a thin NbTi layer (≈ 20 nm) with a thinner Nb "pinner." Also, the ratio $(H_{c2})_{NbTi}/(H_{c2})_{Nb} = D_N/D_S \approx 7$, a value lower than that of other workers [Aarts (90), Karkut (88)]. As a consequence of their small layer thicknesses and anisotropies, our MLs are not well-suited to the study of dimensional crossovers [Takahashi (86b, 86a)], where thicker layers and higher anisotropies in the electron diffusion constants are usually employed to see the full range of behaviors. Nevertheless, our samples *do* show weak 3D to 2D crossover of the superconducting order parameter as T decreases, just below T_c and $\theta = 5.4°$, which can be adequately explained in either the anisotropic GL or TT theories of the parallel upper critical field.

In Fig. 4.8. we plot $H_{c2}(5.4°, T)$ for samples [20/4], [20/10], and [27/9] and a fit to Eq. 4.11. for each [Aarts (90), Broussard (87), Ruggiero (82)], where $H_{c2D}(0)$ is the zero temperature upper critical field of the clean layer and $T_{3D\text{-}2D}$ is the temperature where the clean layers decouple from one another—since this is a result of the anisotropic GL model, it is not expected to hold exactly. The extent of the 2D regions in our samples is somewhat ambiguous, but for each sample we could fit Eq. 4.11. to some portion of the phase diagram between $0.88 < t < 0.95$, though sometimes with large uncertainties. We also found that the 3D-2D crossover took place when $\xi(T_{3D\text{-}2D}) \sim 0.65\ \Lambda$, which is in line with theoretical predictions [Klemm (75)] as well as with the experimental data of others [Maj (91), Aarts (90)]. Tables 4.4. and 4.5. summarize the anisotropic GL parameters extracted from the upper critical field data for our multilayers.

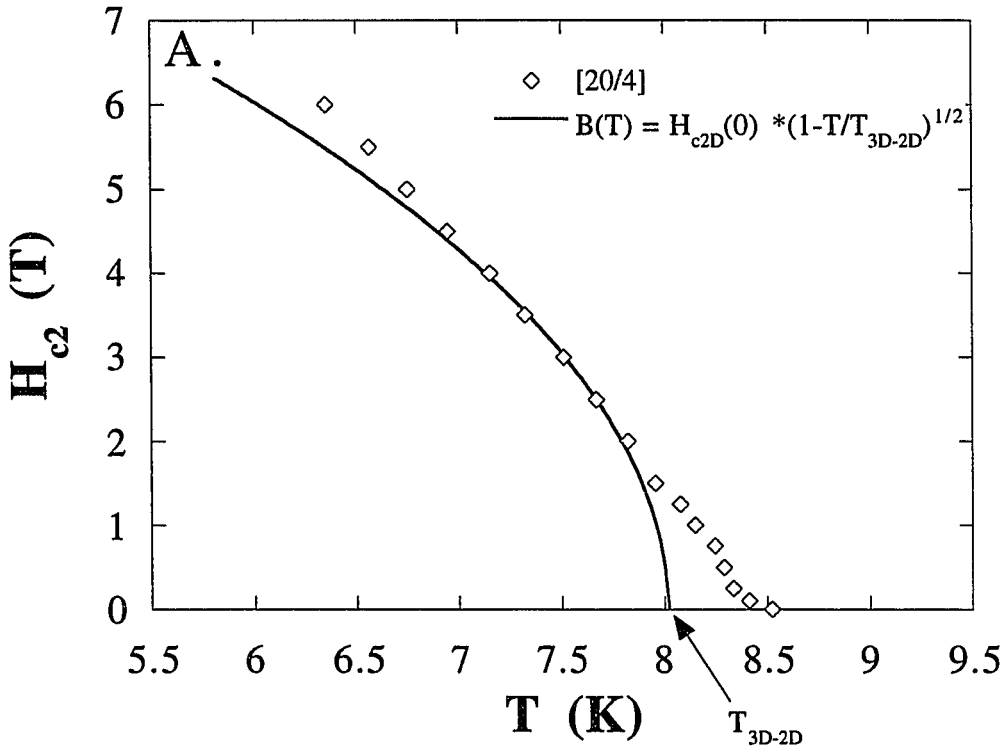

Figure 4.8.a. $H_{c2}(5.4°, T)$ and a fit to the quasi-2D region for sample [20/4]. Sample [20/4] has what appears to be unusual curvature above the infered $T_{3D\text{-}2D}$.

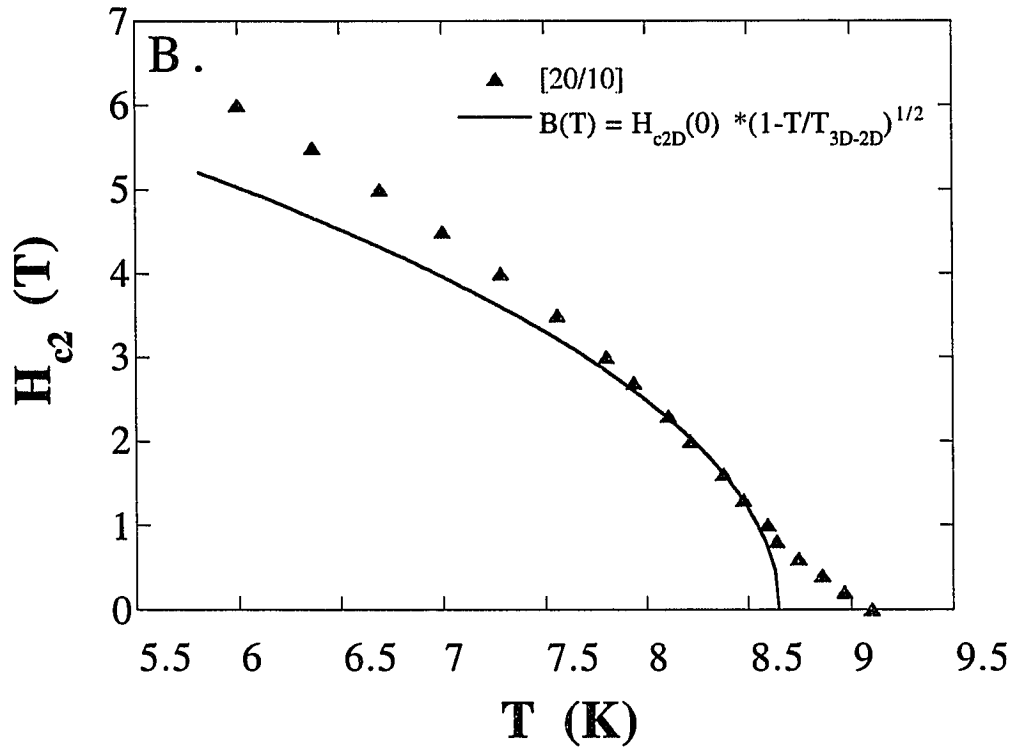

Figure 4.8.b. $H_{c2}(5.4°, T)$ and a fit to the quasi-2D region for sample [20/10].

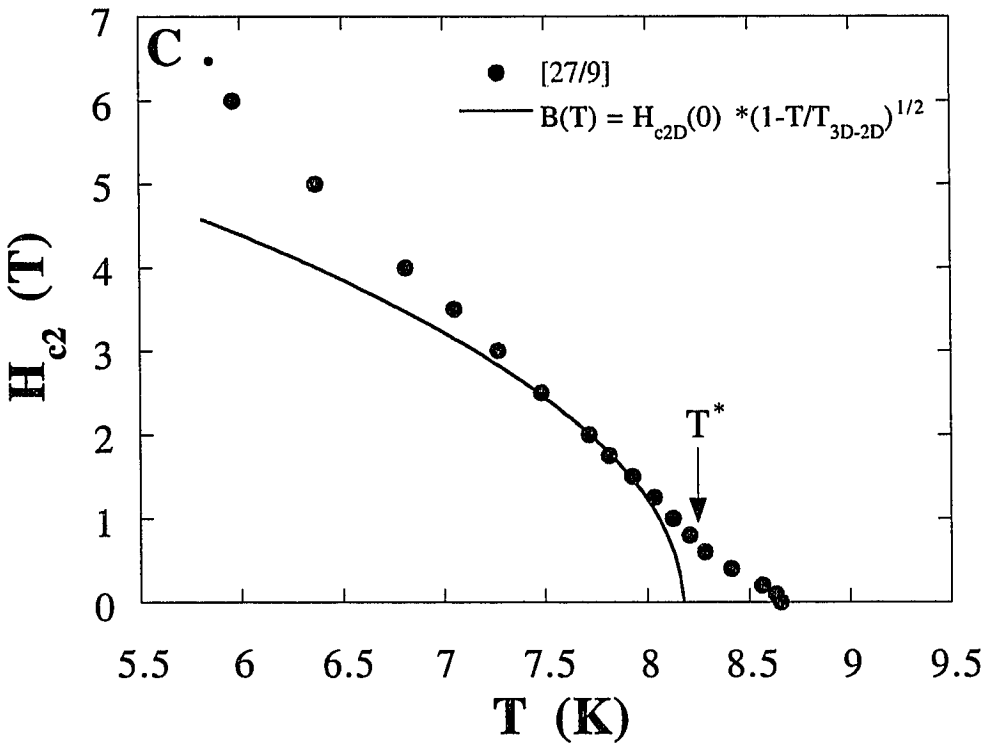

Figure 4.8.c. $H_{c2}(5.4°, T)$ and a fit to the quasi-2D region for sample [27/9]. Sample [27/9] has no well-defined 2D region, but shows a change in linear slope near T^*.

Table 4.4. Superconducting properties of Nb/$Nb_{0.37}Ti_{0.63}$ multilayers, $H_{c2}(90°)$.

Sample	T_c (K)	$-\left.\frac{dH_{c2}}{dT}\right\|_{T_c}$ (T/K)	$\xi_{GL}(0)$ (nm)
[20/4]	8.52(5)	3.12(1)	3.6(2)
[21/6]	8.51(5)	2.83(1)	3.8(2)
[21/8]	8.65(5)	2.40(1)	4.1(2)

In Table 4.4. we see that the perpendicular upper critical field slope near T_c increases as the ratio d_{NbTi}/d_{Nb} increases, which is sensible because we expect the upper critical field to go up as $Nb_{0.36}Ti_{0.64}$ becomes a larger volume percentage of the whole. The same explanation holds for the θ = 5.4° data. We expect $-dH_{c2}/dT$ to increase monotonically as d_{NbTi}/d_{Nb} increases [Aarts (90)], which is confirmed by the actual $-dH_{c2}/dT$ vs. d_{NbTi}/d_{Nb} plot in Fig. 4.9. The dashed line is a guide to the eye. The overall weak anisotropy of our samples is reflected in the poor fit of the anisotropic GL theory to the 2D regions (see Fig. 4.8.)—$H_{c2D}(0)$ has uncertainties up to 15%, though it does increase as d_{Nb} decreases, as one would expect qualitatively from Eq. 4.12. Some of our samples do not have so much a 2D region as a change in linear slope at a temperature T^* (see Fig. 4.8.c.). This behavior has been seen by other groups [Aarts (90), Kuwasawa (90), Obi (87)], though Aarts *et al.* [90] saw it for samples with much longer Λ (> 50 nm). Without detailed microscopic calculations for these particular geometries, we cannot say more about the 3D-averaged-to-quasi-2D crossover in our samples.

As a last point, we discuss the absence of the second dimensional crossover in H_{c2} predicted by TT. We do not have calculations of the microscopic theory for our samples, but we do know qualitatively that the critical ratio D_N/D_S needed to observe the Takahashi-Tachiki Effect increases dramatically as the thicknesses of the N and S layers drop below $\xi_N(0)$, the zero temperature GL coherence length in the N layer [Takahashi (86b)]. We also know (see Fig. 4.6.) that T^+ goes to zero as D_N/D_S decreases. Our $\xi_{Nb}(0)$ = 12.3 nm, which is larger than any of our values of d_{Nb}—we therefore would expect

from Takahashi-Tachiki theory not to see the sharp upturn unless D_N/D_S were quite large. Our value of D_N/D_S (≈ 7) is either too low to observe the crossover altogether or it is too low to observe it at the upper critical fields we investigated (~ 6 T).

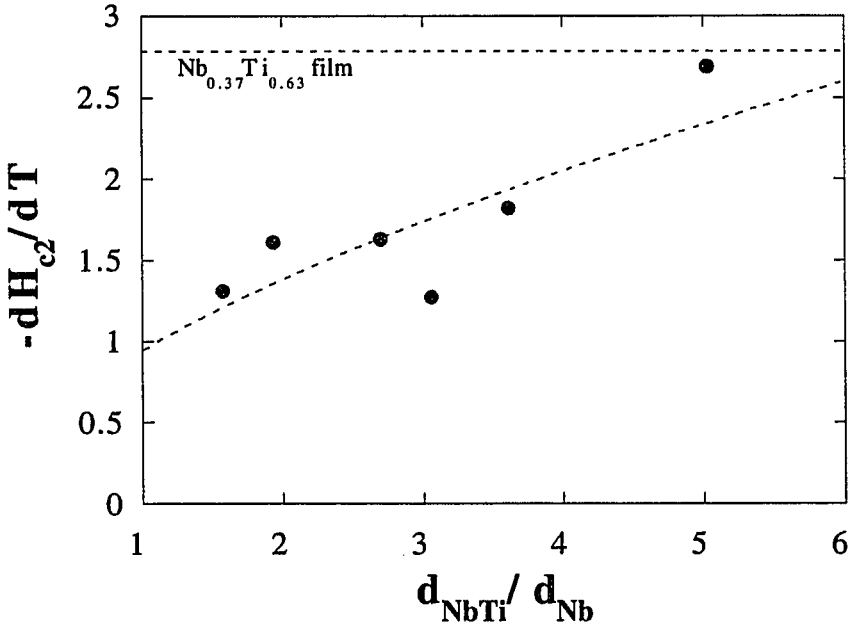

Figure 4.9. Slope of the $\theta = 5.4°$ upper critical field near T_c for all our multilayers as a function of d_{NbTi}/d_{Nb}. The slope for a thick $Nb_{0.37}Ti_{0.63}$ film is indicated at the top. The dashed line through the data is a guide to the eye.

Table 4.5. Superconducting properties of multilayers, $H_{c2}(5.4°)$.

Sample	T_c (K)	$-\left.\frac{dH_{c2}}{dT}\right\|_{T_c}$	$\xi_{GL}(0)$ (nm)	$T_{3D\text{-}2D}$ (K)	$H_{c2D}(0)$ (T)
[20/4]	8.52(5)	3.01(26)	3.7(2)	8.02(20)[a]	11.69(50)
[21/6]	8.51(5)	2.04(9)	4.5(2)	8.08(9)	9.75(30)
[21/8]	8.65(5)	1.82(8)	4.7(2)	8.11(9)	9.15(70)
[20/10]	9.10(5)	1.80(8)	4.6(2)	8.65(7)	8.85(25)
[14/9]	8.41(5)	1.46(6)	5.3(3)	7.43(10)	9.84(50)
[27/9]	8.65(5)	1.42(6)	5.3(3)	8.17(20)[b]	8.28(100)[b]

[a] shows unusual behavior for T > 8 K
[b] 2D region very ambiguous

Chapter 5. The Peak Effect

"It has to happen quicker when it's thicker."
—N. D. Rizzo

In this chapter, we will discuss our results on the flux pinning properties of single films and multilayers. As might be expected from the upper critical field measurements (Ch. 4.), we observe very different behavior depending on the orientation of the applied magnetic field B with the plane of the layers. For angles θ sufficiently away from perpendicular, the global pinning force density $F_p = J_c B$ and sometimes the critical current density J_c show a pronounced peak effect as the field is increased. (Unless otherwise noted, all the measurements of the peak effect which we will present were taken at $\theta = 5.4°$.) This peak effect has been seen by others for NbZr/Nb MLs [Koorevaar (93), Nojima (93)], Nb/Ta MLs [Broussard (88)], and PbBi/Bi compositionally-modulated MLs [Raffy (81, 74b, 74a, 72)]. We also describe a simple model which qualitatively captures the aspects of the peak effect in our MLs. We begin by investigating the pinning properties of our single films.

5.1. Pinning in Nb and $Nb_{0.37}Ti_{0.63}$ Films

In Fig. 5.1. we plot the critical current densities versus applied magnetic field at 4.2 K of our thick Nb and $Nb_{0.37}Ti_{0.63}$ films and that of optimized conventional wire made for the superconducting super collider (SSC). The pinning strength of the SSC wire is primarily from α-Ti inclusions [Meingast (89b), Larbalestier (84)] which precipitate out of the initial alloy after extensive heat-treatments above 400 °C. The J_c of extensively cold-worked bulk NbTi is typically an order of magnitude lower, and is due to weak grain boundary pinning [Ling (95), Larbalestier (84), Collings (83)]. The J_c of our $Nb_{0.37}Ti_{0.63}$ film in near parallel fields ($\theta = 5.4°$) is comparable to that of a heavily cold-worked bulk

NbTi wire [Ling (95)]. However, when the field is perpendicular to the film surface (parallel to the growth direction), the critical current of our $Nb_{0.37}Ti_{0.63}$ film is much larger—larger even than the J_c of SSC wire. This type of anisotropy in the pinning of nominally isotropic thin films has been observed by other workers, and is attributed to the columnar growth of grain boundaries [Stejic (94), Kumar (94), Koorevaar (93)]—the pinning force is greatly increased when the field is applied parallel to the growth direction of the grains. The critical current for our thick Nb film at $\theta = 90°$ is very low and negligible above ~ 1 T, which reflects the weaker grain boundary pinning and lower H_{c2} of Nb (because of the large ξ and small κ) compared to $Nb_{0.37}Ti_{0.63}$.

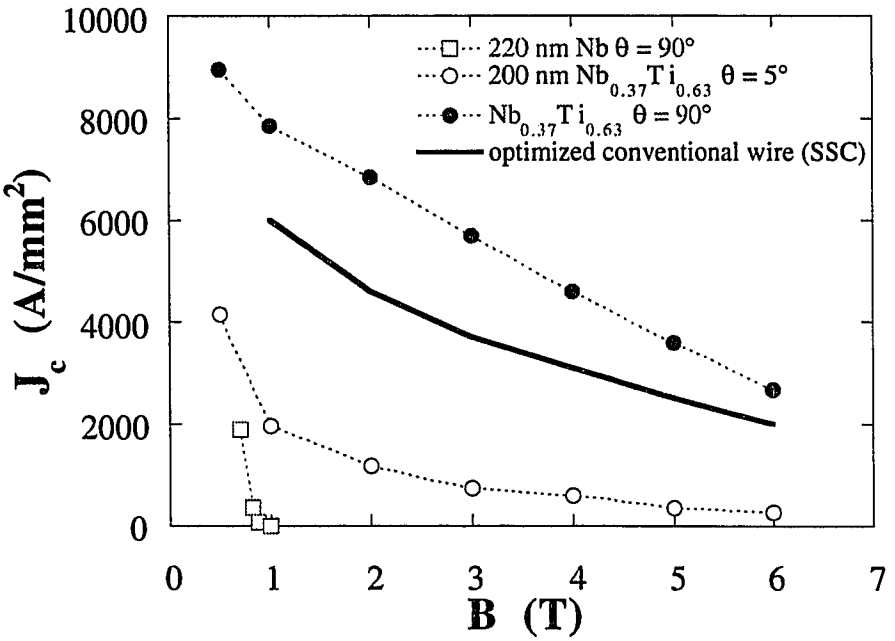

Figure 5.1. Critical current density versus field at 4.2 K for Nb ($\theta = 90°$) and $Nb_{0.37}Ti_{0.63}$ (θ = 5.4° and 90°) films. $J_c(B)$ of an optimized conventional wire is provided for comparison.

5.2. The Influence of Layering on the Pinning Properties

The critical current density is normally a monotonically decreasing function of field, at least for an isotropic superconductor in intermediate fields ($H_{c1} \ll B \ll H_{c2}$) [Larkin (79)]. What happens if the superconductor is anisotropic? In our multilayer samples, $J_c(B)$ for $\theta = 90°$ is a monotonically decreasing function, but the magnitude of J_c (or equivalently, F_p) is increased by as much as a factor of 2 at low fields over that of the thick single films. In Fig. 5.2. we plot $J_c(B, 90°)$ for three multilayer samples, [20/4], [21/6], and [21/8], and a 200 nm thick $Nb_{0.37}Ti_{0.63}$ single film. This increase of pinning forces of multilayers over single films is most likely due to the reduction of the tilt modulus c_{44} (see Ch. 2.6. and Ch. 5.5.3.1.) in layered superconductors in perpendicular fields [Koshelev (93)].

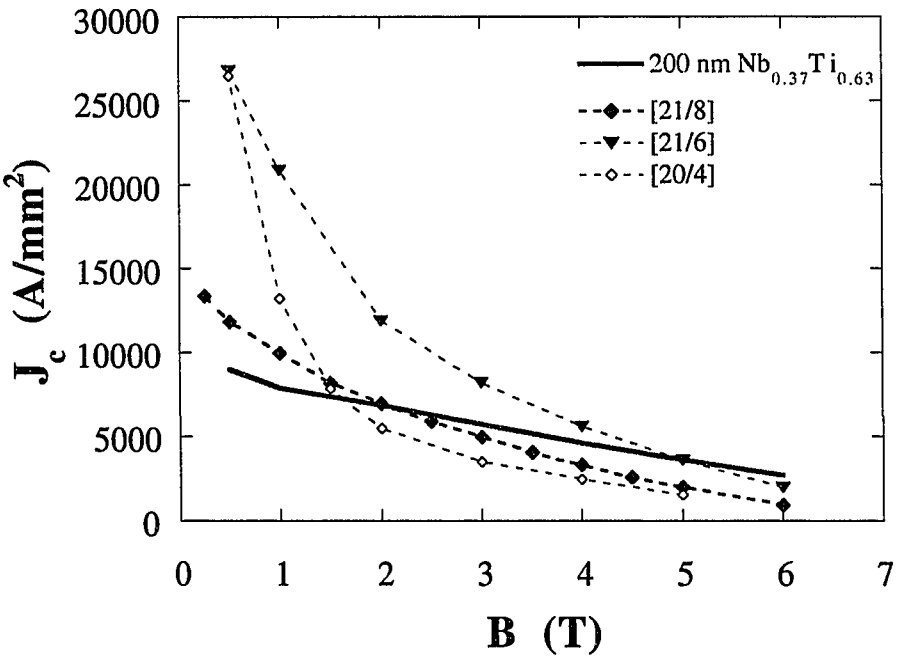

Figure 5.2. Critical current density versus magnetic field at $\theta = 90°$ for samples [20/4], [21/6], and [21/8] at 4.2 K. Also included for reference is the J_c of a single film of $Nb_{0.37}Ti_{0.63}$.

In Fig. 5.3.a. we plot $J_c(B)$ at $\theta = 5.4°$ and 4.2 K for a thick $Nb_{0.37}Ti_{0.63}$ film and samples [20/4] and [21/6]. We plot the corresponding global pinning force densities $F_p(B) = J_cB$ in Fig. 5.3.b. What is most striking in Fig. 5.3.a. is the peak in J_c for sample [21/6]. Sample [20/4] does not show a peak in Jc, but rather a plateau. Both multilayers have *very* large J_c (and F_p) compared to the unlayered $Nb_{0.37}Ti_{0.63}$ film which shows the expected monotonic decrease of J_c. The pinning force density also shows unexpected features for the multilayer samples. Typically, $F_p(B)$ for isotropic films is a dome-like function with a single maximum [Larkin (79)]. In Fig. 5.3.b. we see the pinning force curves have a shoulder at low fields (sample [21/6]) or even two maxima (sample [20/4]). We define two fields which we will use to characterize the peak effect in our MLs: B_{min} is the inflection point between maxima on the F_p curve (corresponding closely with the minimum in J_c), B_{max} is the field of maximum pinning force above B_{min}. We have marked the fields B_{min} and B_{max} for [21/6] in Fig. 5.3.b. We choose the pinning force density to characterize the peak effect, rather than J_c, because it is a more fundamental quantity in the theories of flux pinning and because samples which have no peak in J_c *do* have recognizable structure in F_p. Other groups have chosen to characterize the peak effect in superconducting MLs by the critical current data [Koorevaar (93), Nojima (93), Raffy (81, 74, 72)]. The characteristic fields obtained by this method scale with those obtained from F_p, in general, though as will become clear, do not appropriately capture the physics underlying the peak effect.

5.2.1. The Influence of Layer Thicknesses

5.2.1.1. Elementary Pinning Force of the Interface

What is the mechanism responsible for the large peak pinning forces in our multilayers? We believe it is the variation of the free energy $\propto \Delta(r)$ across the layers which provides the pinning potential—the so-called intrinsic pinning of the structure

[Kwok (91), Tachiki (89a, 89b)]. We know that in the quasi-2D regime (as determined from H_{c2} measurements) $\Delta(r)$ has its maximum in the clean layers [Takahashi (86a, 86b), Dobrosavljevic (77), Ami (75)]. This implies for our MLs that the Nb layers are the barriers to flux line motion and that the lowest energy state of a vortex is to be centered on a $Nb_{0.37}Ti_{0.63}$ layer. A true microscopic calculation of the elementary pinning force f at the interface between two superconductors for $T \ll T_c$ and $B \ll H_{c2}$ is a daunting task. However, a number of groups have done simpler calculations based on a GL approach which show semi-quantitative agreement with our data.

The first was Mkrtchyan et al. [73], who considered the interface between two semi-infinite superconductors and found an analytic approximation for the elementary pinning force per unit length on vortex in the S layer (in cgs):

$$f_L = \left(\frac{\Phi_0}{4\pi\lambda_N}\right)^2 \frac{\lambda_S^2 - \lambda_N^2}{\lambda_S^2 + \lambda_N^2} \frac{1}{\xi_N}, \tag{5.1.}$$

where the subscripts S and N refer to the dirty and clean layer respectively. Using our values for the various GL parameters, we obtain $f_L \sim 3 \times 10^{-3}$ N/m at 4.2 K.

Tachiki and Takahashi [89a] modeled a layered superconductor by assuming a sinusoidal variation of $\Delta(r)$ across the layers. By comparing the free energy difference between the system with and without a vortex located at a minima of $\Delta(r)$ they obtained an expression for the maximum intrinsic elementary pinning force (in cgs units):

$$f_L = \frac{H_c}{8\pi} 2\pi\Lambda \left(\frac{\xi_\perp}{\xi_\parallel}\right)\eta, \tag{5.2.}$$

where η is a function which depends on the magnitude of the modulation of $\Delta(r)$ and the ratio $\xi_\parallel/\Lambda$. Over a wide range of parameters, $\eta \sim 0.2$. Using this value for η, we obtain $f_L \sim 6 \times 10^{-4}$ N/m.

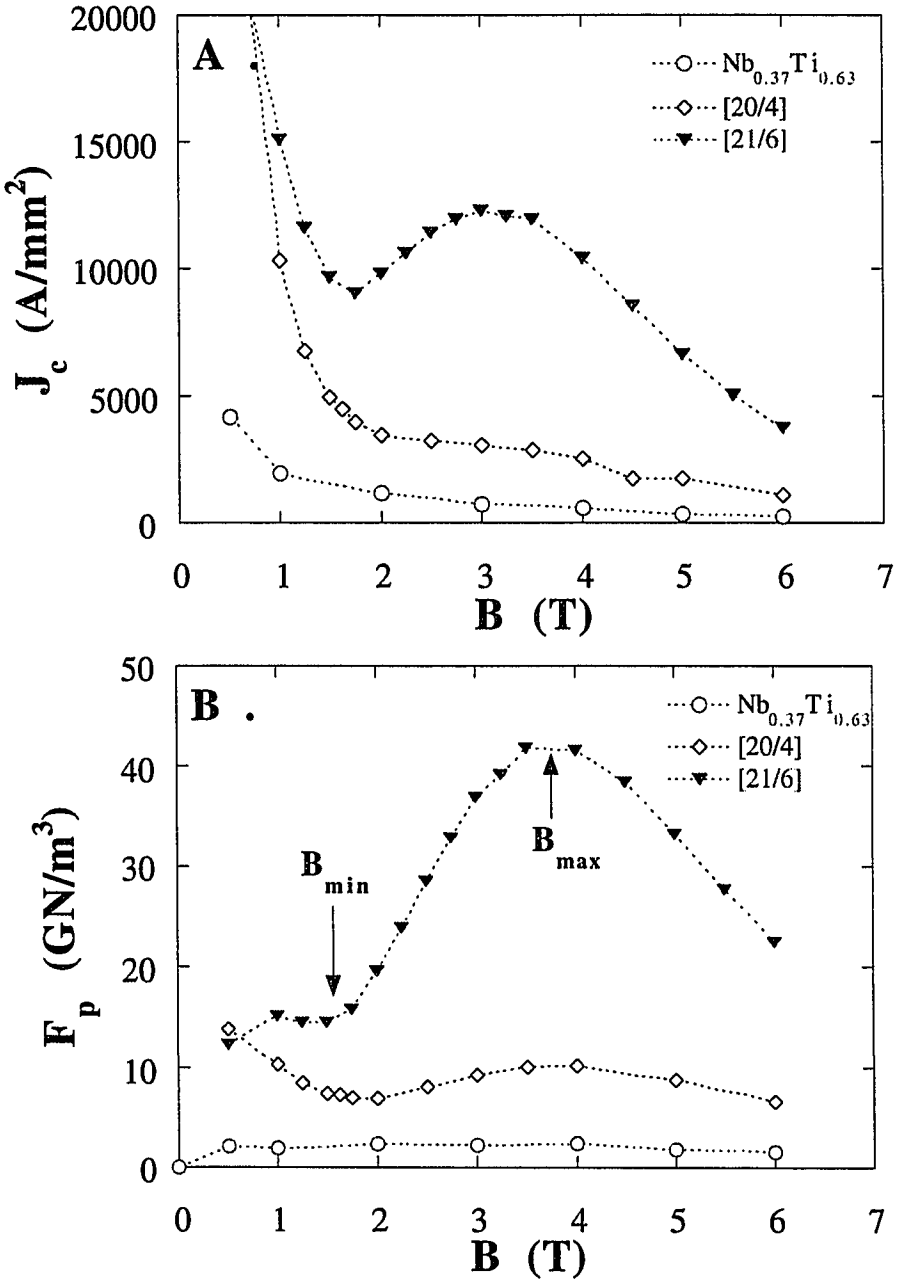

Figure 5.3. The influence of layering on the pinning behavior in near parallel fields. A) the critical current densities at 4.2 K of a thick $Nb_{0.37}Ti_{0.63}$ film and samples [20/4] and [21/6]. B) the corresponding pinning force densities. B_{max} and B_{min} for [21/6] are marked.

Takahashi, Tachiki and Sunaga [93] considered a model similar to Mrktchyan *et al.* [73], but performed numerical calculations for the specific example of an interface between two superconductors with equal coherence lengths, but whose penetration depths differ by a factor of 2. They found $f_L \sim 7H_c^2\xi$, or 7 x 10^{-4} N/m using the value of H_c(4.2 K) ~ 0.16 T for $Nb_{0.37}Ti_{0.63}$ [Collings (83)] and our value of ξ(4.2 K) ~ 5 nm. They claim that f_L increases greatly as the ratio of the penetration depths increases.

Stejic [93] performed a mean-field GL calculation of the elementary pinning force of an idealized NbTi/Nb multilayer (infinite extent, T_c of both layers equal, bulk GL lengths, and no interdiffusion) as a function of d_{Nb} and d_{NbTi}. We plot his numerical results for f_L, along with our experimental values at 4.2 K, as a function of d_{Nb} in Fig. 5.4. We determined the experimental values of f_L using the definition

$$f_L = \frac{F_p}{n_\Lambda}\xi_{NbTi}, \tag{5.3.}$$

where $n_\Lambda = 1/\Lambda$ is the linear density of pinners (the discontinuities in superconducting properties at the interfaces). We take F_p of the multilayer samples at B_{max} because we believe that is the field regime where the vortex-vortex interactions are least important (compared to the vortex-pin interactions), therefore $F_p(B_{max})$ represents the "true" intrinsic pinning force of the layered structure. The fit to the experimental data is fair: the nearly linear dependence of f_L on d_{Nb} is reproduced, but the magnitude is too high by a factor ~ 2. The dashed line for the slope in Fig. 5.4. is a guide to the eye. Note it does not pass through zero Nb thickness. That the interfacial pinning extrapolates to zero near d_{Nb} ≈ 3 nm implies the homogenization of the GL properties at the interface on the same scale—possibly indicating interdiffusion between the Nb and $Nb_{0.37}Ti_{0.63}$ layers. Considering the approximations used, we find the agreement between our data and the various estimates above for the elementary pinning forces consistent with the claim that the high pinning force densities in our samples are due to the layering.

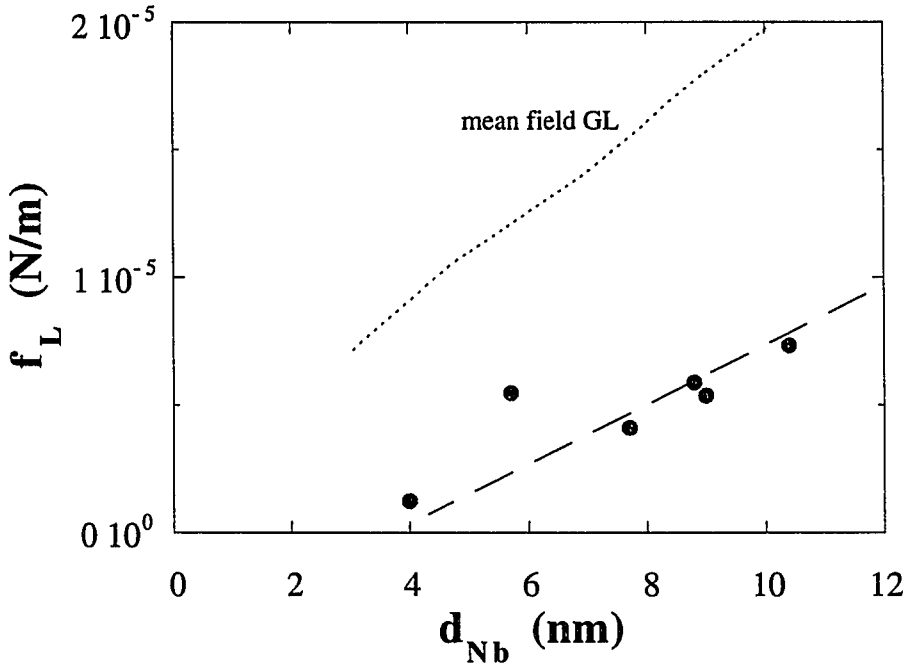

Figure 5.4. The dependence of the elementary pinning force per unit length of the $Nb/Nb_{0.37}Ti_{0.63}$ interface as a function of d_{Nb} at 4.2 K. The dashed line through the data is a guide to the eye. The dashed line above the data is the predicted dependence of $f_L(d_{Nb})$ from [Stejic (93)].

5.2.1.2. Commensurability and the Characteristic Fields

Some workers have attributed the cause of the peak effect seen in multilayers to the geometrical matching between the flux lattice and the intrinsic pinning lattice, which is termed commensurability [Broussard (88), Raffy (81, 74a, 74b, 72), Ami (75)]. It can be shown [Ami (75)] that the matching fields H_m are

$$H_m = \frac{\sqrt{3}\Phi_0}{2\Lambda^2}\frac{1}{n^2+p^2+np}, \qquad (5.4.)$$

where n and p are integers. In the anisotropic case, the triangular Abrikosov lattice is distorted and $H_m' = H_m(m/M)^{1/2}$ [Koorevaar (93)]. We can quickly discard the explanation of the peak as purely geometrical matching because we find no dependence

of B_{max} (which should correspond to H_m) on $1/\Lambda^2$. In fact, B_{max} scales weakly with the N layer thickness as $1/d_{Nb}$ (shown in Fig. 5.5.). Koorevaar *et al.* [93] found much stronger evidence for a $1/d_{Nb}$ dependence for their multilayers—they found B_{max} to be independent of the S layer (NbZr) thickness, as do we. Raffy *et al.* [74a] found $B_{max} \sim 1/\Lambda$, but they could not vary the N and S layer thicknesses independently of one another. Hence a $1/\Lambda$ dependence would be indistinguishable from a $1/d_N$ dependence. No group has shown the $1/\Lambda^2$ dependence of B_{max} expected for simple commensurability for multilayers [Broussard (88), Raffy (74a)]. Eq. 5.4. has no terms which are temperature dependent—simple commensurability cannot account for the temperature dependence of the characteristic fields, which we explore in the next section.

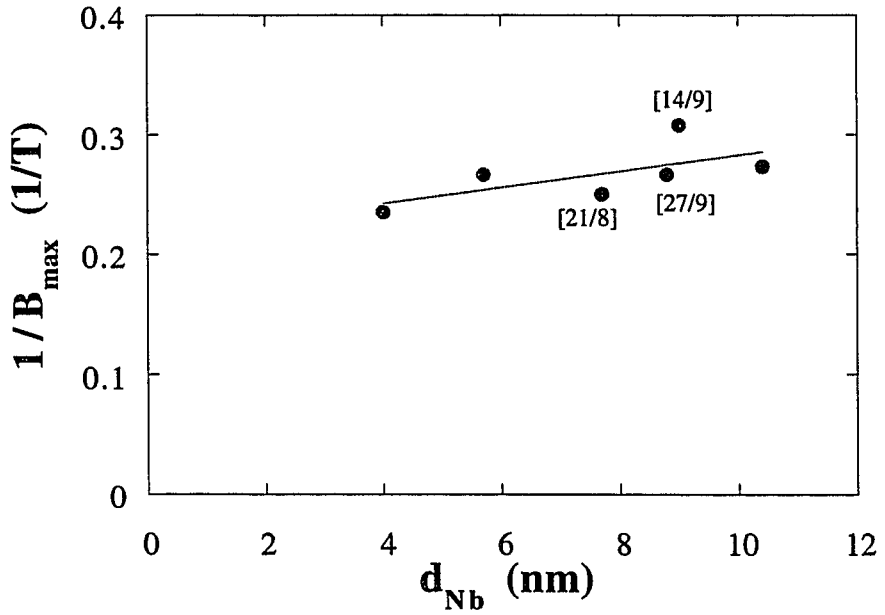

Figure 5.5. The dependence of B_{max} on the Nb layer thickness at 4.2 K. Samples with comparable d_{Nb} but differing d_{NbTi} are marked. The line through the data is a guide to the eye.

So far, we have confined our attention to B_{max}. What about B_{min}? We find that B_{min} scales as $1/\Lambda$. This is shown in Fig. 5.6., where we plot $1/B_{min}$ versus Λ at 4.2 K. Other groups have not reported systematic data on B_{min}—the data of Koorevaar *et al.*

[93], by far the most extensive of the other studies of the flux pinning behavior of multilayers, are qualitatively similar to ours (see figures 3 and 11 of [Koorevaar (93)]).

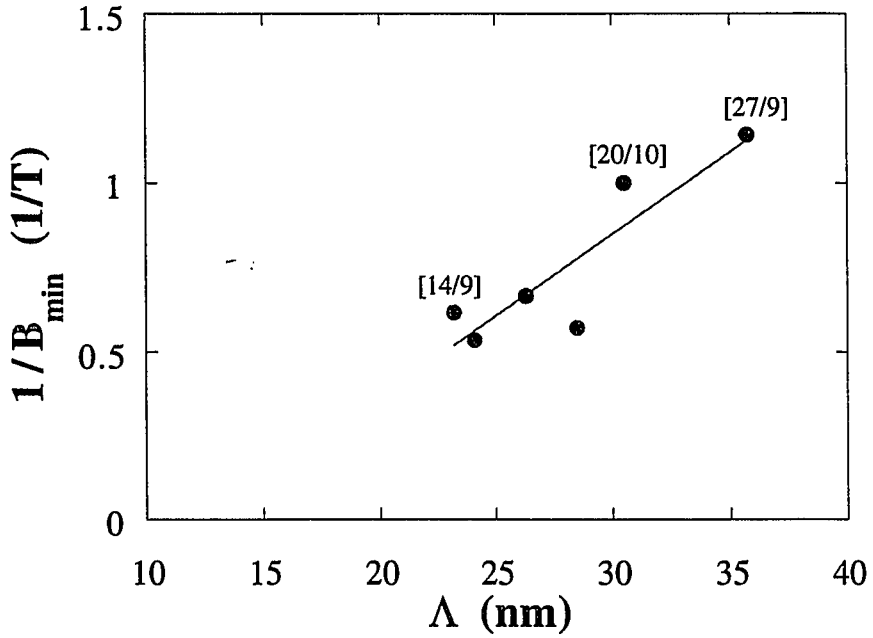

Figure 5.6. The dependence of B_{min} on the multilayer period at 4.2 K. Samples with comparable d_{Nb} and different d_{NbTi} are marked. The line through the data is a guide to the eye.

5.3. Temperature Dependence of B_{max} and B_{min}

We find the characteristic fields B_{min} and B_{max} are not only structure dependent, but temperature dependent as well. We plot the pinning force curves at $\theta = 5.4°$ for [20/10], whose behavior is typical of our MLs, for 4 temperatures between 4.2 and 7.38 K in Fig. 5.7.a. We plot the corresponding critical current densities in Fig. 5.7.b. Both characteristic fields decrease as the temperature is increased. We find that B_{max} scales with $(1- T/T_{3D\text{-}2D})^{1/2}$ (see Eq. 4.11.), where $T_{3D\text{-}2D}$ is the temperature below which $\Delta(\boldsymbol{r})$ first nucleates in the N layers, determined from H_{c2} measurements. Equivalently, we may say that B_{max} scales with $H_{c2D}(T)$ and *not* $H_{c2}(T)$. In Fig. 5.8. we plot the phase diagrams

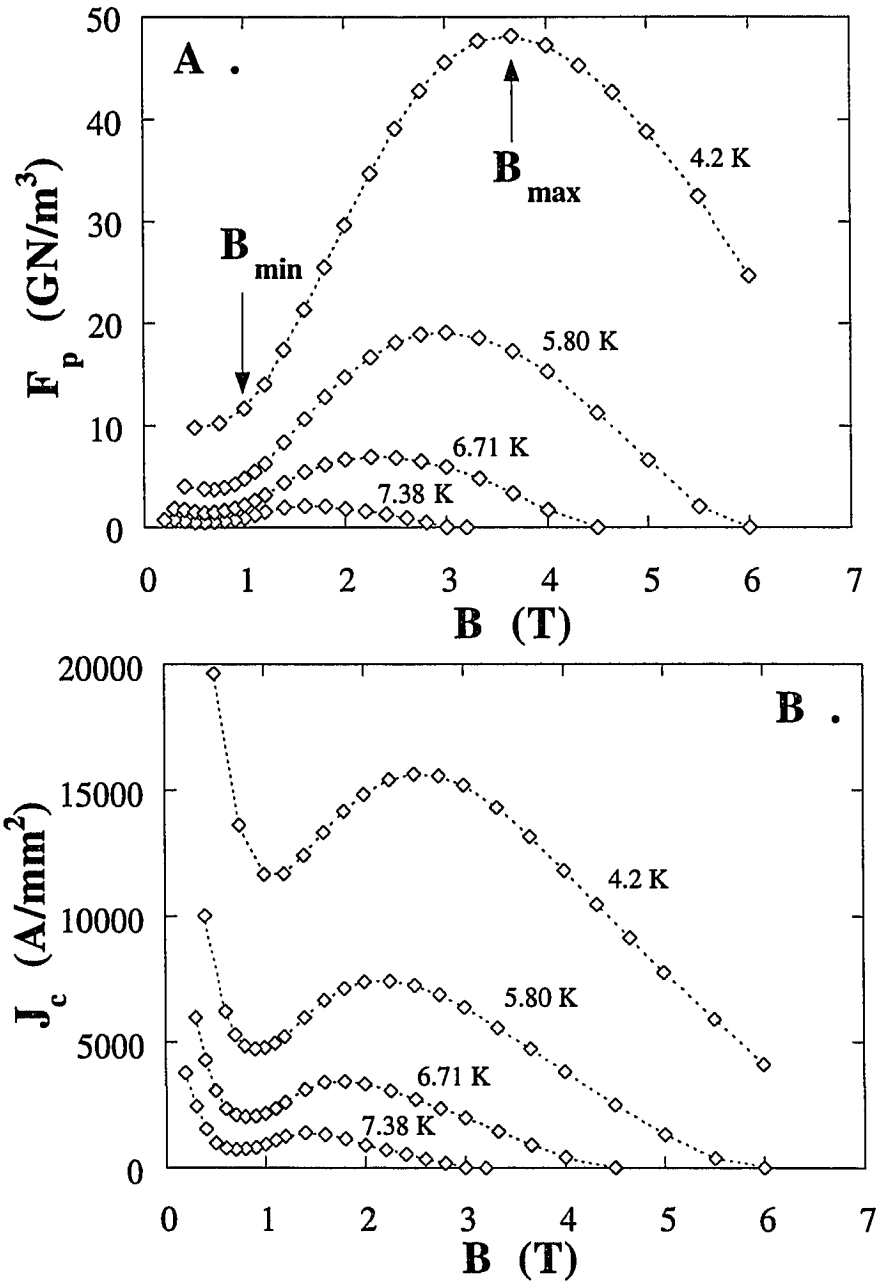

Figure 5.7. The temperature dependence of the pinning behavior of sample [20/10] at θ = 5.4°. A) the pinning force density versus field at 4.2 K, 5.80 K, 6.71 K, and 7.38 K. B) the corresponding critical current density curves. B_{max} and B_{min} are marked for 4.2 K.

(see Ch. 4.2.2.3.), along with the characteristic fields, for samples [21/8], [14/9], [21/6], and [20/10]. We summarize the data from the scaling of B_{max} to Eq. 4.11. in Table 5.1. Koorevaar *et al.* [93] were the first to report the dependence of B_{max} on $(1- T/T_{3D\text{-}2D})^{1/2}$, though Raffy *et al.* [74b] made the observation that the peak effect was not observable above a certain temperature, which we believe to be $T_{3D\text{-}2D}$.

B_{min} is temperature dependent, though not as strongly as B_{max}. It does not in general scale with either H_{c2D} or H_{c2}. The behavior of $B_{min}(5.4°, T)$ for all the samples we measured is plotted in Fig. 5.8.

Table 5.1. The Scaling of B_{max}[a,b]

Sample	$B_{max}(0)$ (T)	$B_{max}(0)/H_{c2D}(0)$
[14/9]	4.75(10)	0.48(6)
[21/6]	5.64(25)	0.58(5)
[21/8]	5.53(12)	0.60(8)
[20/10]	4.83(20)	0.55(5)
[27/9]	4.85(30)[c]	0.59(14)

[a] see Table 4.5. for more information on the phase diagrams of our MLs
[b] errors or uncertainties in last digit indicated by quantity in parenthesis
[c] ill-defined 2D region

5.4. Angular Dependence of B_{max} and B_{min}

The peak effect in our samples exists over a suprisingly wide range of magnetic field orientations to the plane of the layers [Koorevaar (93)]. In Fig. 5.10., we plot the F_p curves for sample [21/6] at 5 values of θ, the angle between the plane of the layers and the applied magnetic field, at 4.2 K (see also Fig. 3.12.). The peak persists out to ~ 60° though its magnitude decreases as θ is increased. Other groups have also seen such a critical angle around $\theta = 60°$ [Koorevaar (93)]. Both B_{max} and B_{min} shift out in field as θ is increased. We note that the $\theta = 90°$ data shows no peak, though its overall magnitude is larger thanthe 58.9° data. As mentioned in section 5.1., the "secondary maximum" at (or

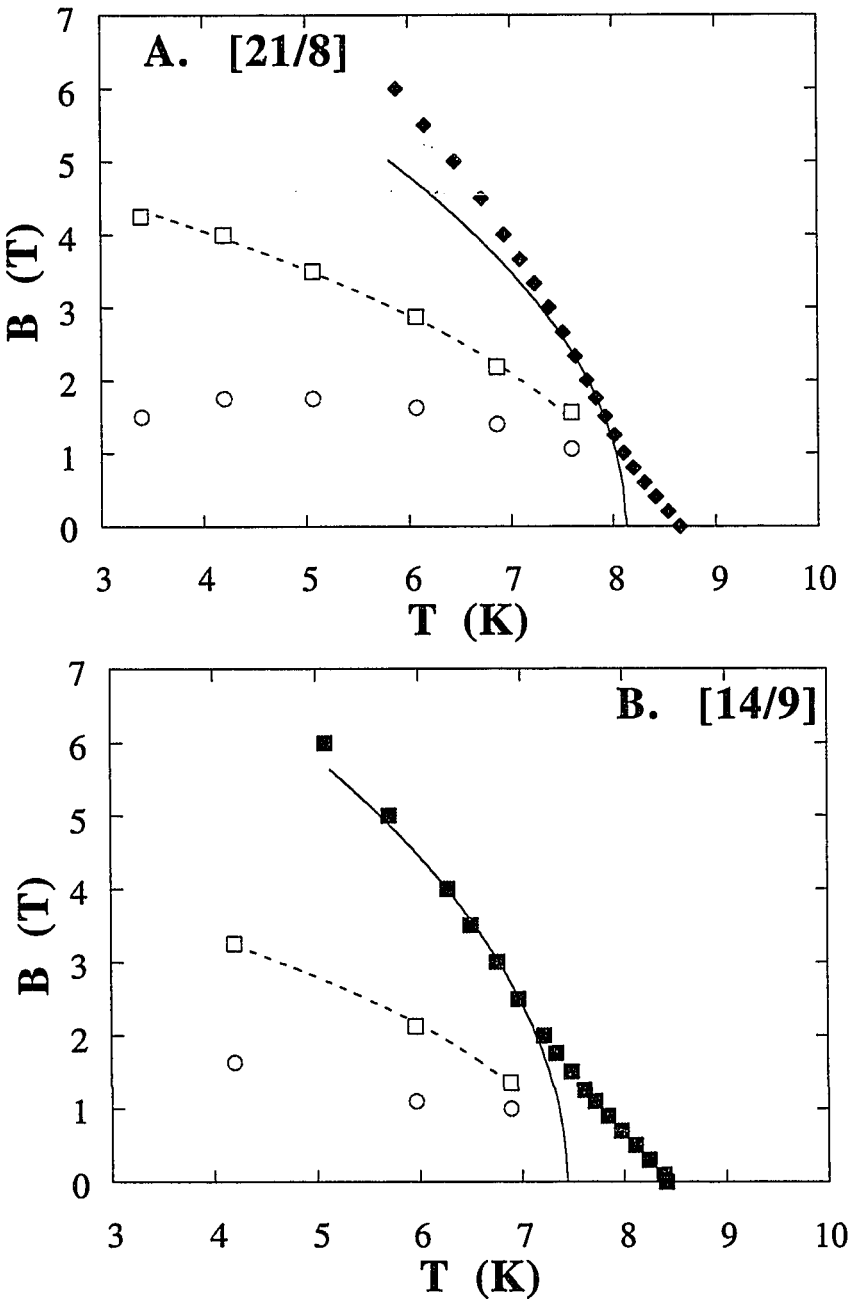

Figure 5.8. The phase diagrams $H_{c2}(5.4°, T)$ for A) [21/8] and B) [14/9]. $H_{c2D}(T)$ is indicated as a solid line (Eq. 4.11.). B_{max} and B_{min} are plotted as squares and circles respectively, with a fit to Eq. 4.11. through B_{max}.

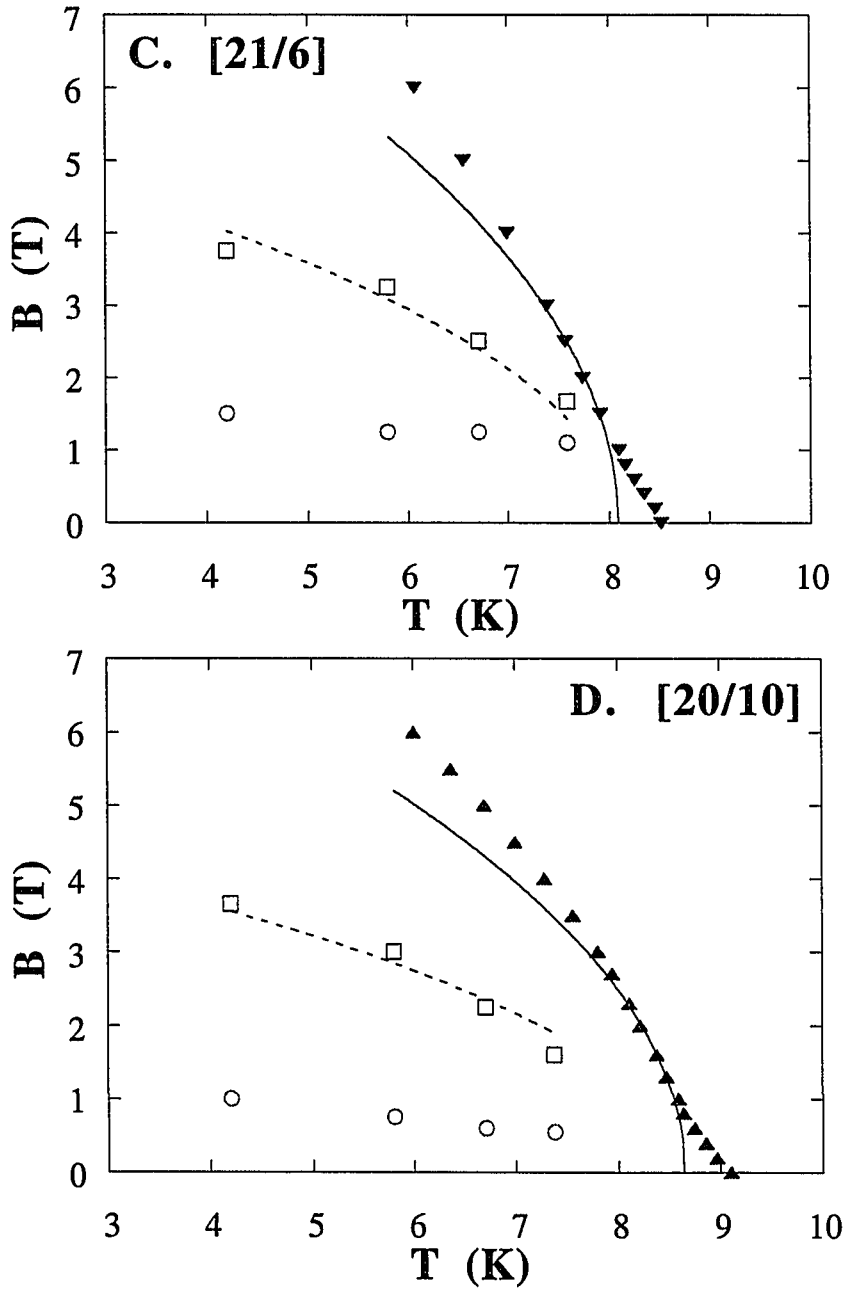

Fig. 5.8. (continued) The phase diagrams $H_{c2}(5.4°, T)$ for C) [21/6] and D) [20/10]. $H_{c2D}(T)$ is indicated as a solid line (Eq. 4.11.). B_{max} and B_{min} are plotted as squares and circles respectively, with a fit to Eq. 4.11. through B_{max}.

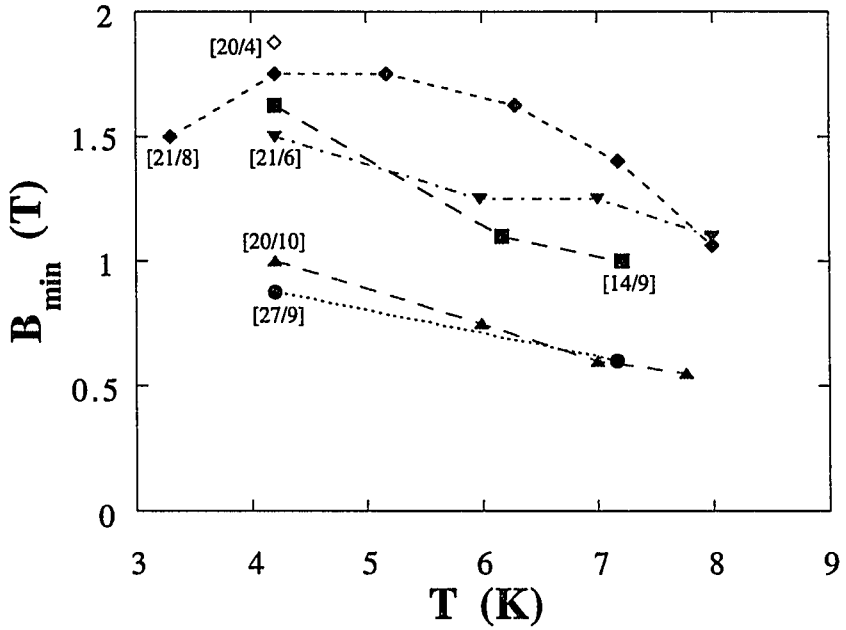

Figure 5.9. The temperature dependence of B_{min} at $\theta = 5.4°$.

near) perpendicular fields is caused by the pinning of the columnar grain boundaries, which form parallel to the growth direction.

5.4.1. Stepwise Vortex Lattice in Layered Superconductors

Recently, Tachiki and Takahashi [89b] proposed a new model, the stepwise vortex lattice (SVL), to describe the vortex lattice structure in layered superconductors. They developed their model with the high-T_c oxide superconductors in mind, but the ideas are quite general and apply to any layered superconductor with intrinsic and extrinsic pinning [Nojima (93), Koorevaar (93)]. We discussed the intrinsic pinning of our MLs in section 5.2.1.1. Extrinsic pinning centers are simply the inhomogeneities in the system not caused by the layering: grain boundaries, point defects, and the like.

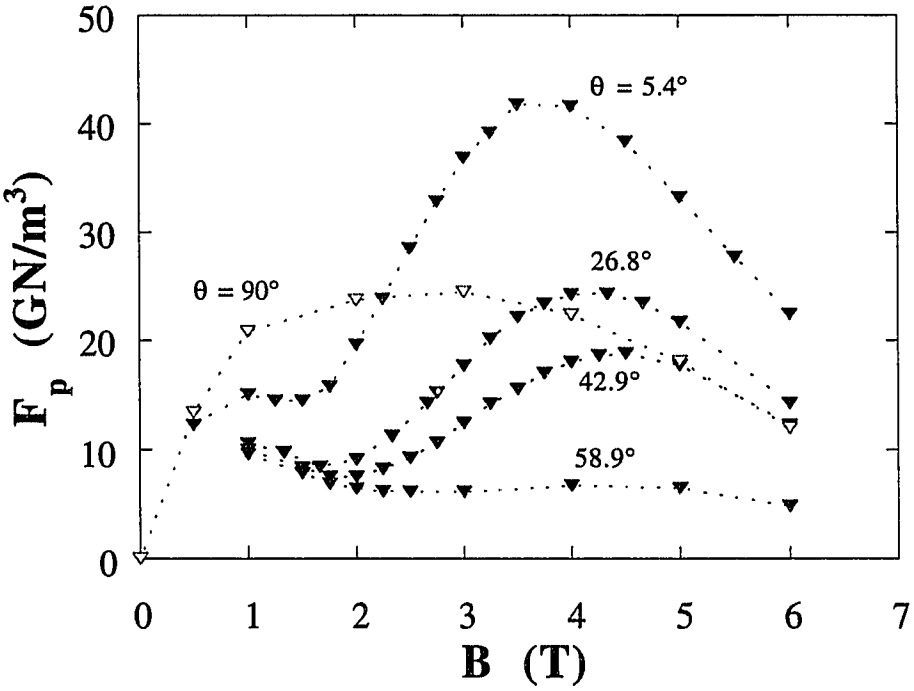

Figure 5.10. Pinning force versus field at $\theta = 5.4°$, 26.8°, 42.9°, 58.9°, and 90° for [21/6].

In a regime where the characteristic pinning energy U_{pin} is large and the vortex self-energy (line tension) U_{line} is small, the vortex penetrates the superconductor in a stepwise fashion, neglecting contributions from the vortex-vortex interactions. This is illustrated in Fig. 5.11. A single vortex line now consists of vortex "disks," located in the clean N layers, and vortex "strings" in the dirty S layers. Nojima *et al.* [93] and Koorevaar *et al.* [93] both suggested the peak effect in their MLs was associated with the creation of a stepwise vortex lattice. If we return to Fig. 5.10., we can now explain the existence of a critical angle θ_c, above which the peak dissapears, in the stepwise vortex picture: if $U_{line} > U_{pin}$, then the kinked vortex state is unfavorable.

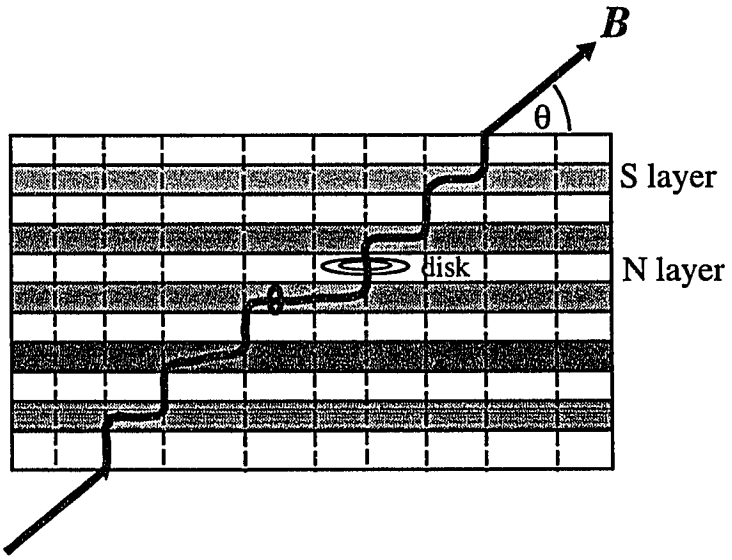

Figure 5.11. A kinked vortex line in a layered superconductor. "Disks" or "pancakes" of screening supercurrents are formed in the clean N layer and "strings" connect them through the dirty S layer. The circulating currents of a string and disk are indicated near the center of the figure. The dashed lines indicate the columnar grain boundaries, which are mainly parallel to the growth direction. The disks are pinned by the grain boundaries, the strings by the interfaces. Adapted from [Tachiki (89b)].

5.4.1.1. Estimate of θ_c

We can make a crude estimate of the critical angle in the above picture. We compare the line tensions of the stepwise vortex with the straight vortex as functions of θ. If we apply a magnetic field at an angle θ to a layered superconductor, with layer thicknesses d_S and d_N, the line tension in the unkinked case is given by (see Fig. 5.12.):

$$U_{line} = \frac{\varepsilon_S d_S + \varepsilon_N d_N}{\sin\theta}, \tag{5.5.}$$

where ε_S and ε_N are the line tensions in the S and N layer respectively. Tinkham [80] gives the formula for the vortex line energy for $\kappa \gg 1$(in cgs):

$$\varepsilon = \frac{H_c^2}{8\pi} 4\pi\xi^2 \ln\kappa. \tag{5.6.}$$

In the kinked vortex state, the total line tension is:

$$U_{line}^{KVL} = \varepsilon_N d_N + \varepsilon_S \left[d_S + \frac{(d_S + d_N)}{\tan\theta} \right]. \qquad (5.7.)$$

Evaluating Eqs. 5.5. and 5.7. for sample [21/6], we find that the kinked vortex lattice is energetically favored for $\theta < 80°$, which is larger than the experimentally determined value of θ_c, but vortex-vortex interactions [Koshelev (93), Sudbø (91)] and extrinsic pinning centers [Tachiki (89b)], which are neglected in this model, are important in determining the state of the vortex lattice in layered superconductors. We have also applied the extreme type II limit to Nb ($\kappa \sim 6$).

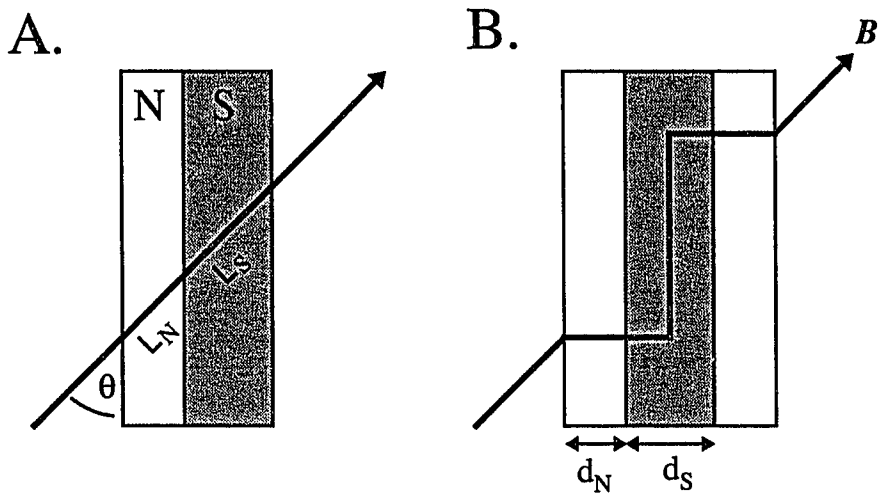

Figure 5.12. Minimizing the line tension of a vortex in a layered superconductor: although the straight vortex (A) has the least length, the total vortex line energy is lower in the stepwise vortex (B).

5.4.2. The Influence of the Lorentz Force

Other groups have amassed a large amount of data which also suggests the strong connection between the formation of a stepwise vortex lattice and the peak effect in superconducting multilayers. Koorevaar *et al.* [93] performed an experiment which tested the configuration of the vortex lattice by measuring the speed (voltage) and direction of vortex motion with a driving current at a number of fields. They applied the field $\boldsymbol{B}$ at an angle to the planes and to the transport current—$\boldsymbol{B} = (B_x, B_y, B_z)$ and $\boldsymbol{J} = (0, J, 0)$ (the axes are defined in Fig. 5.13.). The Lorentz force on the vortices is $\boldsymbol{J} \times \boldsymbol{B} = (-JB_z, 0, JB_x)$. The longitudinal voltage of the sample V measured the vortex motion along the layers (the x-component); the Hall voltage V_H measured vortex motion across the layers (the z-component). The direction of $\boldsymbol{B}$ was chosen such that the Hall and longitudinal voltages would be approximately equal if the sample were to behave isotropically. Koorevaar *et al.* found that above B_{min} the ratio V_H/V dropped rapidly—at B_{max} the ratio was a factor of 100 below that at B_{min}. They explained the drop of V_H/V as a result of the onset of a SVL—motion across the layers decreases as the vortices become more and more kinked.

To further test the assumption that the onset of the peak correlated with the onset of a SVL, both Koorevaar *et al.* [93] and Nojima *et al.* [93] performed experiments where ϕ, the angle between the plane of the layers (also the transport current density $\boldsymbol{J}$) and the applied field $\boldsymbol{B}$ could be varied. We illustrate their experimental geometry in Fig. 5.13. Both groups found that the critical current densities taken at $\boldsymbol{J} \perp \boldsymbol{B}$ ($\phi = 90°$) and $\boldsymbol{J}$ along $\boldsymbol{B}$ ($\phi \neq 90°$) were almost equal above B_{max}, but diverged quickly at lower fields. Koorevaar *et al.* [93] also saw a plateau in J_c beginning at B_{min} in the $\boldsymbol{J}$ along $\boldsymbol{B}$ orientation. We show their data in Fig. 5.14.

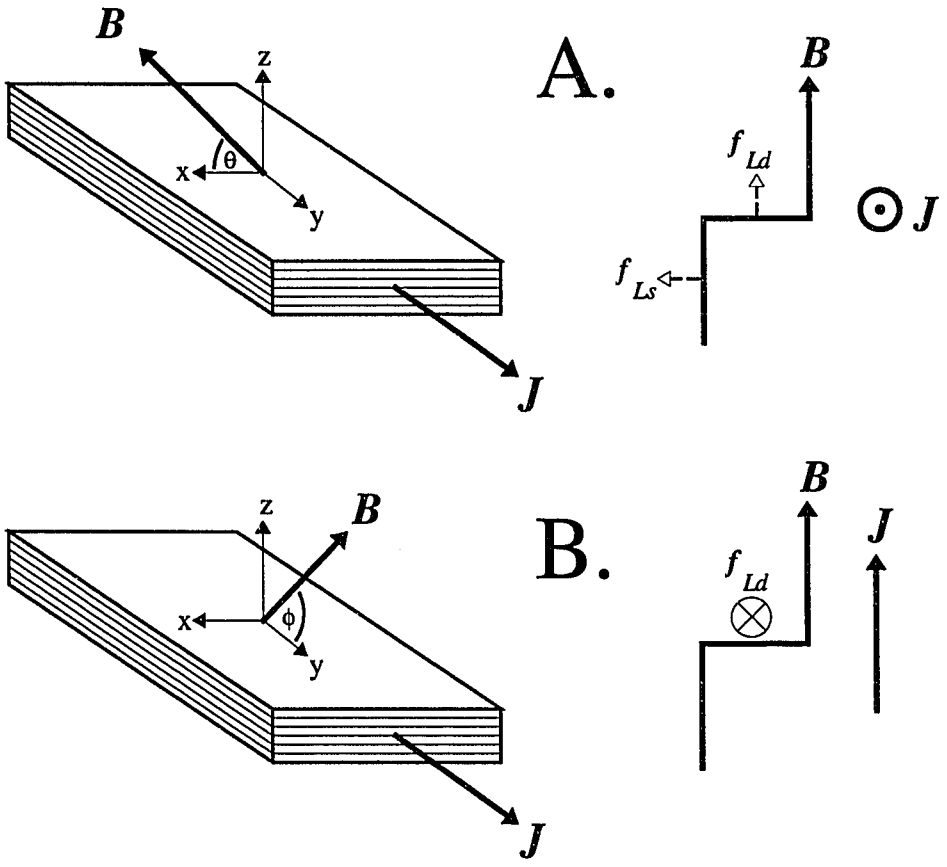

Figure 5.13. Two possible configurations for measuring the pinning force of layered superconductors and illustrations of the Lorentz forces on the different segments of a stepwise vortex. A) $\boldsymbol{J} \perp \boldsymbol{B}$ ($\phi = 90°$), the usual configuration, both strings and disks feel a Lorentz force. B) $\boldsymbol{J}$ along $\boldsymbol{B}(\phi \neq 90°)$, only the disks feel a Lorentz force. Adapted from [Koorevaar (93), Tachiki (89b)].

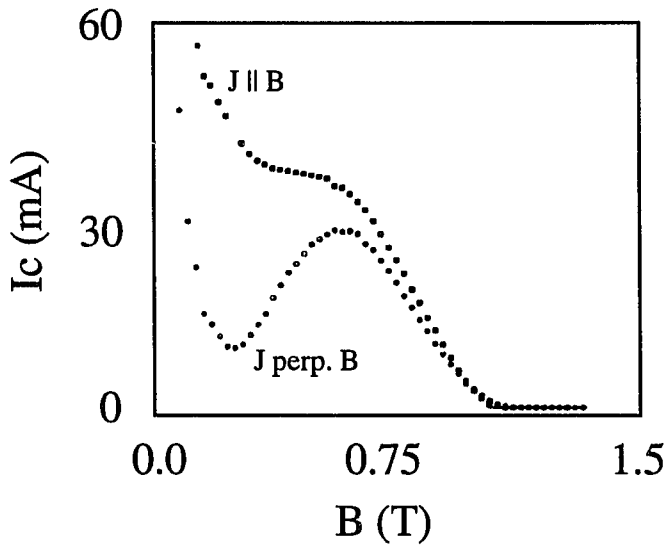

Figure 5.14. The orientational dependence of $I_c(B)$ for a 7 period 24 nm Nb/24 nm NbZr multilayer at 9.25 K and $\theta = 14°$. With $\boldsymbol{J} \perp \boldsymbol{B}$, the usual peak effect is seen. When $\boldsymbol{J}$ is along $\boldsymbol{B}$, the Lorentz forces on the strings are drastically reduced (see Fig. 5.13.). Note that in either orientation, the critical currents are nearly equal above the peak. Adapted from [Koorevaar (93)].

The above results cannot be explained if the vortices pass straight through the sample, because $\boldsymbol{F_p} = \boldsymbol{J_c} \times \boldsymbol{B}$ is very different in either case. However, in the fully-formed stepwise vortex lattice, there is no Lorentz force on the strings when $\boldsymbol{J}$ is along $\boldsymbol{B}$ ($\phi \neq 90°$) (see Fig. 5.12.b.)—the dissipation is primarily due to disks moving along a layer. The data of Koorevaar *et al.* and Nojima *et al.* are understandable if above B_{max} the SVL is fully formed. J_c is the same for the two orientations ($\boldsymbol{J} \perp \boldsymbol{B}$ and $\boldsymbol{J}$ along $\boldsymbol{B}$) because the strings are strongly pinned by the intrinsic potential and only motion of the disks along the layers is possible.

We believe the plateau Koorevaar *et al.* saw in J_c beginning at B_{min} for the $\boldsymbol{J}$ along $\boldsymbol{B}$ orientation, along with all the data we and others have gathered on the peak effect, suggests that the onset of kinking occurs at B_{min} and that the SVL is fully formed in the region of B_{max}. The reason the vortices become kinked is because the pinning energy

U_{pin} becomes larger than the elastic energy of the vortex-vortex interactions near or at B_{min}, which allows the individual vortices to deform to take best advantage of the strong periodic pinning potential. This process continues until the difference between the pinning energy and the elastic energy is no longer increasing, which occurs in the vicinity of B_{max}.

Our interpretation above is not the only one of the peak effect in MLs [Koorevaar (93), Nojima (93), Raffy (81, 74b, 74a, 72)]. We begin our explanation of the peak effect with a discussion of the alternatives proposed by other workers in the field.

5.5. Explanations of the Peak Effect

The first group to see the peak effect in multilayers were Raffy and coworkers [Raffy (81, 74b, 74a, 72)]. They suggested that the mechanism for the peak effect was geometric matching between the flux lattice and the layers. We have discussed above the inadequacies of this explanation. The strong temperature dependence and non-commensurate structural dependences of the peak, in our view, argue against their claim.

Two other groups have recently made suggestions on the nature of the peak effect in MLs. We discuss them in following two sections.

5.5.1. Dimensional Crossover of $\Delta(r)$

Nojima *et al.* [93] found that below H^{max} (the field at peak J_c) the configuration of the vortices was well-described by the stepwise vortex lattice, based on measurements of the angular dependence of the critical current density of their Nb/NbZr MLs which seemed to follow the predictions of Tachiki and Takahashi [89b] for the SVL. The angular dependence of J_c above H^{max} was also consistent with the existence of an SVL. Above H^{max}, they suggested that the fall-off of J_c could be explained by the decoupling of the N layers from one another, i.e. the Nb layers are proximity coupled through the S layers, and that coupling ~ $\Delta(r)$ in the S layers goes to zero at H^{max}. They therefore claimed that

H^{max} represents a dimensional crossover field: below it, the vortex lattice behaves in an anisotropic 3D manner; above it, since the Nb layers are decoupled, the vortices would behave like a stack of 2D "pancake" vortices. This model was originally proposed for the highly anisotropic high-T_c oxide superconductors or superconductor-insulator multilayers [Koshelev (93), Clem (91)]. These pancakes only exist in the strongly superconducting layer and are magnetically coupled to one another through the nonsuperconducting layers.

A number of problems exist with this model, chief of which is the suggestion that Δ goes to zero in the S layers below H_{c2} of the system. Since H_{c2} of a bulk NbZr layer is much higher than that of Nb, it seems unlikely that at any point on the phase diagram that NbZr is not superconducting—Nojima *et al.* expressed some uncertainty on this point as well. Koorevaar *et al.* [93] were the first to point out that the claims of Nojima and coworkers can be tested directly—if H^{max} represents the field at which the Nb layers are decoupled from one another, it should depend in some fashion on the thickness of the S layer. Koorevaar *et al.* found no dependence of H^{max} on d_{NbZr}. We have also seen no dependence of B_{max} or H^{max} on d_{NbTi}, rather they depend on d_{Nb} (see Ch. 5.2.1.2.). Lastly, we point out that the angular dependence data of Nojima *et al.* [93] can be fully explained in the stepwise vortex model of Tachiki and Takahashi [89b].

5.5.2. Structural Vortex Lattice Transition

Based on the data they obtained, Koorevaar *et al.* [93] proposed a phase diagram for superconducting multilayers using the ideas of Takahashi and Tachiki given above [Takahashi (86a, 86b), Tachiki (89b)]. It is shown in Fig. 5.15. Briefly, Koorevaar and coworkers said that H^{max} represents not a dimensional crossover field, but the location of a structural transition of the vortex lattice. Below H^{max}, the vortices are straight and behave isotropically. At H^{max}, the vortex lattice undergoes a transition to a SVL. The SVL

is more strongly pinned than the straight Abrikosov lattice, which causes a peak to be observed in J_c.

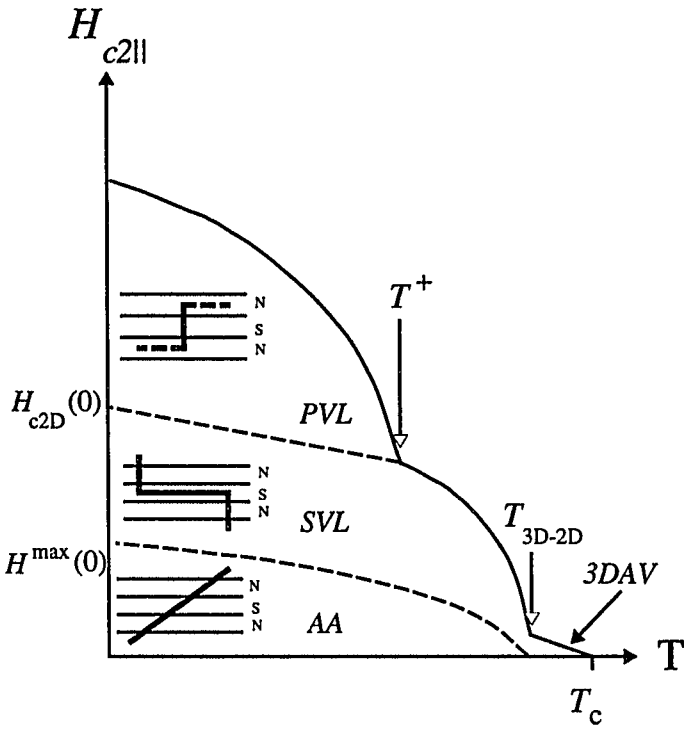

Figure 5.15. The proposed phase diagram of Koorevaar *et al.* for superconducting multilayers in near parallel fields. The vortex lattice has 5 distinct regions: the Meissner state (below H_{c1} and T_c, not shown); the 3D averaged state near T_c; the anisotropic Abrikosov lattice for $H_{c1} < B < H^{max}$ and $T < T_C$; the stepwise vortex lattice for $H^{max} < B < H_{c2D}$ and $T < T_{3D\text{-}2D}$; and the pancake vortex lattice for $H_{c2D} < B < H_{c2}$ and $T < T^+$. The last three configurations of the vortex lattice are schematically illustrated in the appropriate region. Adapted from [Koorevaar (93)].

However, Koorevaar *et al.* do not definitively describe a mechanism which would drive the transition itself, or explain its dependences on field, temperature, or ML geometry. They conclude (wrongly, we believe) that the intrinsic pinning of the layer interface cannot account for the vortex lattice transition—they used the estimate of Mrktchyan *et al.* [73] discussed above to estimate the pinning behavior of the interface, but they assume that a change from a nonpinning to a pinning interface occurs at H^{max}.

With this assumption, they could not reconcile the field-dependent behavior of λ_S and λ_N (see Eq. 5.1.) with a transition at H^{max}. Koorevaar and coworkers go on to argue that there might exist *another* intrinsic pinning mechanism: the formation energy of the kinked structure itself may provide an energy barrier. Once formed, the kinks would then prevent movement of the vortices across the layers.

We believe Koorevaar *et al.* to be in error on a number of points. The first and foremost of these is the dismissal of the intrinsic pinning potential of the layers as part of the mechanism which drives the transition from straight, weakly pinned vortices, to kinked, strongly pinned vortices. As we have seen in Ch. 5.2.1.1., four independent estimates of the elementary pinning force of the Nb/$Nb_{0.37}Ti_{0.63}$ interface provide adequate quantitative agreement with our experimental data on the magnitude of $F_p(B_{max})$. We believe the interface provides strong pinning in the whole quasi-2D regime, as defined by $H_{c2D}(T)$. They have also neglected the vortex-vortex interaction in their explanation, which is known to be extremely important in determining pinning behavior, even in the strong pinning regime [Ling (95), Koshelev (93), Brandt (86a), Wördenweber (86), Mullock (85), Larkin (79)]. Lastly, we believe there is a transition from straight to kinked vortices, but its onset is at B_{min}, not H^{max}. We develop a qualitative model to explain the peak effect below.

5.5.3. Reduction of Compression Energy

In the strong pinning regime, vortex-vortex interactions are usually ignored because the magnitudes of the elastic energies U_{tilt} and U_{shear} are far below U_{pin}. The energy cost to compress the vortex lattice U_{comp} is normally much larger than the shear or tilt energies—the vortex lattice is usually considered to be incompressible [Brandt (86b)]. Peak effects were believed to occur for strong pinning samples only near H_{c1} or H_{c2} [Larkin (79)]. However, the situation for multilayers is very different from the usual isotropic bulk systems that are considered.

The weight of experimental evidence, ours as well as that of others [Koorevaar (93), Nojima (93)], and theoretical understanding [Tachiki (89b), Takahashi (86b, 86a)] leads to the conclusions that vortices pass through a layered superconductor in a stepwise fashion in the region of the peak field and that as the field is reduced, the vortices become progressively straighter. Let us analyze the distortions of the vortex lattice in the strongly-pinned stepwise configuration: in Fig. 5.16. we illustrate the SVL at some intermediate field. We see in this figure that there are significant tilt (along the direction of applied field) and *compression* (perpendicular to the applied field) distortions of the straight vortex lattice to form the stepwise lattice. (There may also be shear distortions (not shown), but they are out of the plane, perpendicular to the applied field.) In order for the vortex lattice to form the stepwise structure, the pinning energy must exceed not only the shear and tilt energies, but the compression energy as well. The compression energies are much higher than any of the other energies under consideration in bulk systems, but in multilayers they must compete with the strong, periodic pinning of the layers.

It is this competition between pinning and compression which determines the onset of the kinked vortex lattice—at low fields, the compressive energy cost to deform the vortices into a stepwise lattice is prohibitive, but as the vortex spacing approaches the pinner spacing, this energy must drop rapidly, allowing the vortices to take full advantage of the available pinning potential. This can be seen most easily when the field is applied parallel to the planes: when $a > \Lambda$, significant compression must occur for each vortex to sit at a minimum of the pinning potential; when $a \approx \Lambda$, little or no compression need occur. In some sense, we have returned to the concept of matching or commensurability [Raffy (81, 74b, 74a, 72), Ami (75)], but clearly the vortex-vortex interactions modify the original idea tremendously.

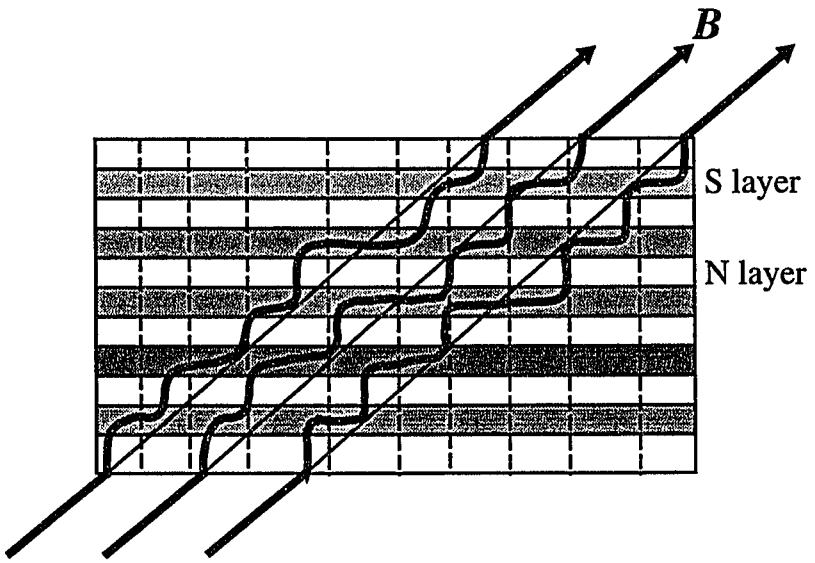

Figure 5.16. The compression (perpendicular to applied ***B***) and tilt (along applied ***B***) distortions of the stepwise vortex lattice. Tilt distortions take place with a characteristic size on the order of the multilayer period Λ. Compression distortions take place on the scale of the intervortex spacing a.

5.5.3.1. The Characteristic Energies

The tilt modulus c_{44} and the uniaxial compression modulus c_{11} are strongly dispersive—the energy cost for distortions decreases greatly when the wavelength of the deformation is short compared to the magnetic penetration depth λ. We can construct expressions for the characteristic energies of the problem [Larkin (79)]. Following Koshelev and Kes [93], we define the various contributions of the vortex-vortex interactions:

$$\begin{aligned} U_{shear} &\sim c_{66}\left[\frac{\pi r_p}{a}\right]^2 a^2\Lambda \\ U_{tilt} &\sim c_{44}\left(\frac{\pi}{\Lambda}\right)\cdot\left[\frac{\pi r_p}{\Lambda}\right]^2 a^2\Lambda \ , \\ U_{comp} &\sim c_{11}\left(\frac{\pi}{a}\right)\cdot\left[\frac{\pi r_p}{\Lambda}\right]^2 a^2\Lambda \end{aligned} \qquad (5.8.)$$

where c_{66}, c_{44}, and c_{11} are the moduli of shear, tilt, and compression respectively, given in Ch. 2. The flux lattice spacing is a and r_p is the range of the pinning force, which Brandt [86a] gives quite generally for extended pins as ~ 0.195 a. These estimates are simply Hooke's law extended to an elastic medium (the vortex lattice) [Brandt (77b, 77a)], which contains the modulus times the square of the deformation (normalized to the appropriate maximum) multiplied by the volume over which the deformation occurs. Notice that the SVL imposes the evaluation of c_{44} and c_{11} at certain wavevectors: for c_{44}, the tilt distortions to form disks in the N layers and strings in the S layers have wavelengths comparable to the multilayer period Λ; for c_{11}, those distortions take place on a length scale comparable to the spacing between vortices. For simplicity we evaluate at a single k, which does not affect our results qualitatively [Koshelev (93)], though a wider range of k is involved ($k_0 - \Delta k < k < k_0 + \Delta k$, where k_0 is the central wavevector and Δk depends on the spatial extent of the deformation [Marion (76)]) .

We use the isotropic limits for the elastic moduli, rather than formulations which explicitly take account of the layered nature of our samples which have been developed by a number of workers [Koshelev (93), Sudbø (91), Kogan (89)]. The influence of anisotropies are important for $\Gamma^2 = M/m \gg 1$, where M is the effective mass perpendicular to the planes and m is the effective mass parallel to the planes. In the limit $\Gamma \rightarrow 1$, the full equations reduce to the isotropic result, as expected. Since all our samples are weakly anisotropic ($\Gamma \leq 1.2$, see Ch. 4.2.2.), we make the simplification of using the conventional moduli.

We start our estimate of the pinning energy by neglecting the extrinsic pinning of our multilayers and considering only the intrinsic pinning: $U_{pin} \sim f(\pi r_p)$, where f is the average pinning force exerted on the vortex lattice by an interface. We may model the field dependence of f by considering two factors: the reduction of the average force on the vortices at low fields because of their density ~ $1/a^2$ and the decrease of the pinning

potential ~ $|\Delta(r)|^2$ ~ (1-b) as $B \rightarrow H_{c2}$ [Koshelev (93), Brandt (86a), Kes (83)]. We modify the (1-b) term by replacing H_{c2} with H_{c2D}, to reflect the fact that $\Delta(r)$ has little variation across the layers when $T \rightarrow T_{3D\text{-}2D}$ (the stepwise vortex lattice disappears [Koorevaar (93), Nojima (93)] because $U_{pin} \rightarrow 0$). The characteristic pinning energy is then:

$$U_{pin} \sim 0.195\pi a(4f_L)w\frac{B}{H_{c2}}\left(1-\frac{B}{H_{c2D}}\right), \qquad (5.9.)$$

where f_L, the elementary pinning force per unit length, was defined in Eq. 5.3. and w is the width of our sample (~ 3 μm) along the field. We multiply f_L by 4 to normalize the scaled pinning force to the maximum measured value. (That is to say, the maximum of the function y = Cb(1-b) occurs at b = 1/2 and y = C/4.)

We plot the characteristic energies versus the field in Fig. 5.17. for sample parameters close to those of [20/10] at 4.2 K: H_{c2} = 8.5 T, H_{c2D} = 6.75 T, ξ = 6 nm, κ = 40, Λ = 30 nm. We see that U_{pin} is an order of magnitude greater than the elastic energies, except as $B \rightarrow 0$. For $B < 0.5$ T the compression energy exceeds the pinning energy. We have seen above that the formation of the SVL requires significant compression deformations of the straight vortex lattice; if $U_{comp} > U_{pin}$, the stepwise lattice cannot form and the total pinning is consequently weak. This is the heart of our interpretation of the peak effect—the field B_{min} characterizes the region where U_{comp} falls below U_{pin}, and the SVL begins to form. Once $U_{pin} \gg U_{comp}$, the vortex-vortex interactions play a limited role in determining the pinning forces on the vortex lattice. In this regime, B_{max} is naturally interpreted as the field at which f has a maximum. In our model, we used the natural scaling $f \sim B/H_{c2}(1\text{-}B/H_{c2D})$, which has a maximum at 1/2 H_{c2D}. This is close to our observed scaling of $B_{max} \sim 0.55\ H_{c2D}$. Koorevaar *et al.* [93] saw similar behavior of B_{max}.

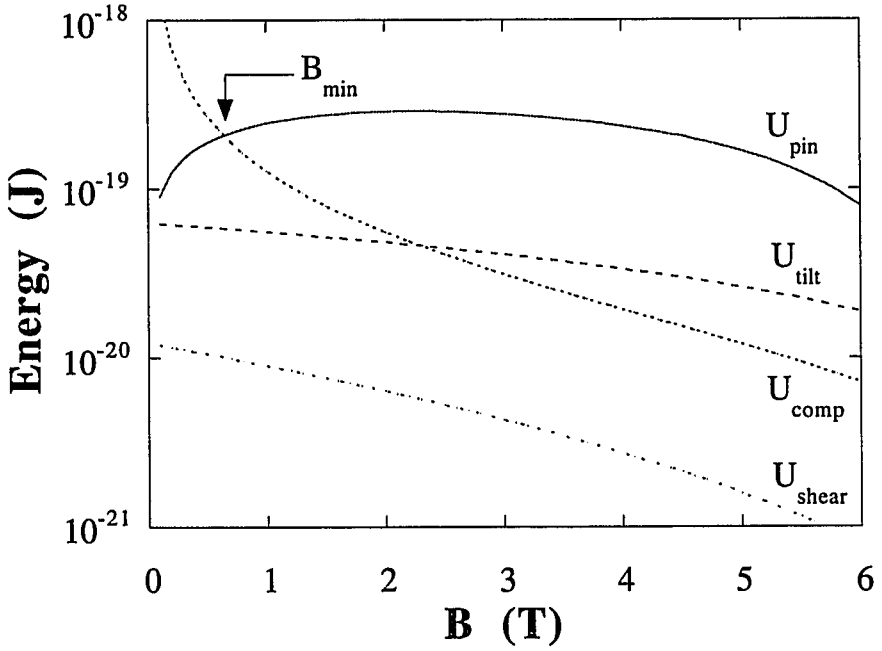

Figure 5.17. Calculated characteristic energies of the vortex-pin and vortex-vortex interactions for sample [20/10] at 4.2 K (H_{c2} = 8.5 T, H_{c2D} = 6.75 T, $\kappa \approx 40$, ξ = 6.2 nm, f_L = 7.34 μN/m). B_{min} occurs at or near the crossing of U_{pin} and U_{comp}.

5.5.3.2. Structural and Temperature Dependences of Characteristic Fields

We have already discussed the behavior of B_{max} above. B_{max} scales with $H_{c2D}(T)$—above H_{c2D} the Nb layers do not sustain appreciable superconductivity ($\Delta(r) \rightarrow 0$) and the S layers (in our case, $Nb_{0.37}Ti_{0.63}$) become decoupled from one another [Koorevaar (93), Takahashi (86b)]. The stepwise vortex lattice cannot exist if the entire sample is not superconducting. Equivalently, the pinning force of the interface, which drives the formation of the SVL, goes to zero when the layers decouple. Above H_{c2D}, the vortex lattice is better described by the 2D pancake model with magnetic coupling between the vortices in the S layers [Koorevaar (93), Koshelev (93), Clem (91)]. The structural dependence of B_{max} is explained naturally in this picture by noting that $H_{c2D} \sim 1/d_{Nb}$ (see Eq. 4.12.).

We can explain the observed dependence of B_{min} on $1/\Lambda$ in a straightforward manner. Let us consider multilayers with the same Nb thickness, hence the same interfacial pinning strength, but differing periods. The condition which defines B_{min} is $U_{comp}(B_{min}) \approx U_{pin}(B_{min})$. If we assume U_{pin} is approximately constant on some small interval of B, we may write:

$$U_{comp}(B_{\min}) = \frac{B_{\min}^2}{\left(1+\frac{\pi^2\lambda^2 B_{\min}}{\Phi_0}\right)\Lambda}\left[\frac{0.195\pi a(B_{\min})}{\Lambda}\right]^2\left[a(B_{\min})\right]^2\Lambda \sim \frac{1}{\left(1+\lambda^2 B_{\min}\right)\Lambda} \sim const \tag{5.10.}$$

from which we see that $B_{min}\Lambda \sim$ constant, since we expect λ to be nearly independent of Λ for $\Lambda \ll \lambda$.

The temperature dependence of B_{min} is also well-explained by our simple model. We plot the crossover between the pinning energy and the compression energy (B_{min}) for sample parameters close to those of [20/10] at three temperatures in Fig. 5.18. We have assumed GL dependences on temperature for quantities we have not measured directly, i.e. κ and λ. From the simulation, we find B_{min} at 4.2 K, 5.8 K, and 6.7 K as 0.65 T, 0.46 T, and 0.38 T respectively. Compare these to the actual values of B_{min} for sample [20/10] in Fig.5.8.: 1.0 T, 0.75 T, and 0.6 T. The agreement between the values and the functional dependence of B_{min} on temperature is very good.

The angular dependence of B_{min} is also simply explained. The compression energy associated with the formation of the SVL is roughly independent of the angle the applied field makes with the planes in our model (in reality, it probably decreases as $\theta \rightarrow$ 90°). Since $U_{comp} \sim$ constant, we need only consider the decrease of the pinning energy as θ increases away from 0°. If we look again at Fig. 5.18., we see for a fixed U_{comp} (say the 4.2 K data), that decreasing U_{pin} (indicated by the arrow) leads to B_{min} shifting to higher fields. Eventually, the pinning energy does not exceed U_{comp} and no peak effect is

observed. Qualitatively, this is what we observe in the experiment. However, we observe that B_{max} also shifts to higher fields as θ increases, even as the interfacial pinning energy is dropping. This is unexplained in our simple model, but may be due to the increasing strength of the extrinsic pinning centers (columnar grain boundaries, point defects, etc.) relative to the intrinsic pinning as $\theta \rightarrow 90°$.

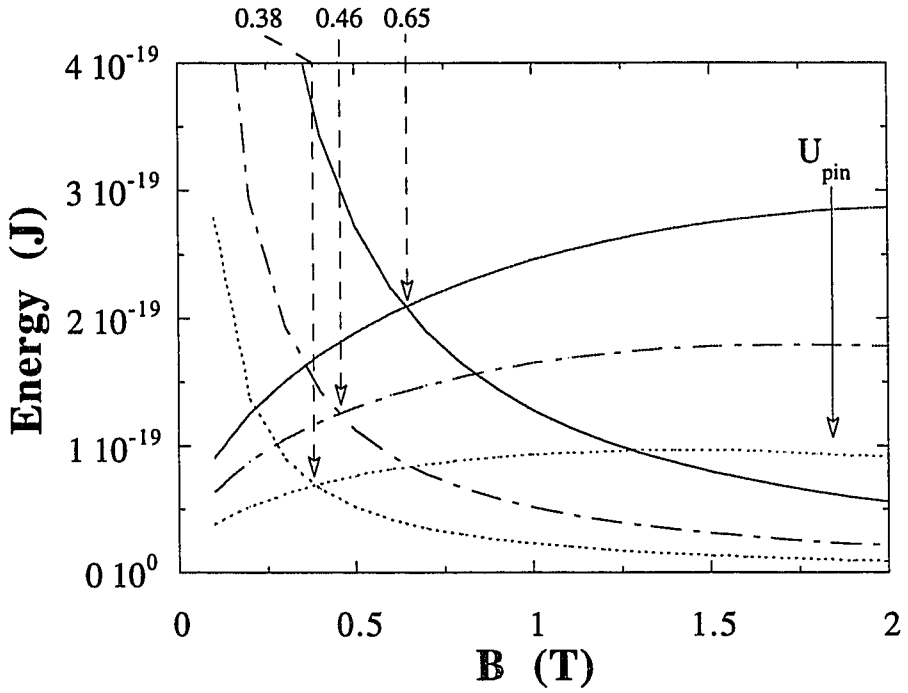

Figure 5.18. Calculated temperature dependence of $U_{pin}(B)$ and $U_{comp}(B)$ for [20/10] at 4.2 K (solid line), 5.80 K (dash-dotted line), and 6.71 K (dashed line). U_{pin} is marked by an arrow in the direction of increasing temperature. B_{min} at each temperature is marked by an arrow. The measured B_{min} are 1.0 T, 0.75 T, and 0.6 T respectively. Model parameters: 4.2 K (same as Fig. 5.17.), 5.80 K (H_{c2} = 6.3 T, H_{c2D} = 5.2 T, $\kappa \approx 53$, ξ = 7.2 nm, f_L = 3.85 μN/m), 6.71 K (H_{c2} = 5.0 T, H_{c2D} = 4.2 T, $\kappa \approx 69$, ξ = 8.1 nm, f_L = 1.83 μN/m).

5.5.4. Final Comments on the Peak Effect

5.5.4.1. The Phase Diagram of Metallic Multilayers

Given the results of our model above, we suggest a slight, but important, modification of the phase diagram proposed by Koorevaar and coworkers (see Fig. 5.15.): we use the field at the onset of the peak effect B_{min}, not the field of peak critical current density H^{max}, to characterize the crossover from a weakly-pinned straight vortex lattice (which Koorevaar *et al.* called the anisotropic Abrikosov lattice) to a strongly-pinned stepwise vortex lattice. The field of maximum pinning force density B_{max} is where the SVL is fully formed: each vortex is in the lowest energy configuration possible. Furthermore, we claim that what drives the peak effect is the competition between the known vortex-pin and vortex-vortex interactions—at low fields, the vortex-vortex interactions determine the pinning behavior, at higher fields, the vortex-pin interaction becomes dominant. Our proposed phase diagram is shown in Fig. 5.19.

5.5.4.2. Other Observations of Peak Effects

Peak effects are also seen in the transport properties of many other superconducting systems: naturally and artificially layered samples in parallel [Ling (91)] and *perpendicular* fields [Neerinck (91), Koorevaar (90)] and unlayered ones [Wördenweber (90), Kes (81), deSorbo (64), Autler (62)]. All of the above may be adequately explained in the collective pinning picture [Wördenweber (90), Mullock (85), Kes (81), Larkin (79)], which is applicable when the pinning is weak compared to the vortex-vortex interactions. Although our samples are clearly in the strong pinning regime, the underlying competition between the vortex-vortex and vortex-pin interactions which gives rise to the peak effect is the common mechanism which unites these very different cases of the peak effect with our own.

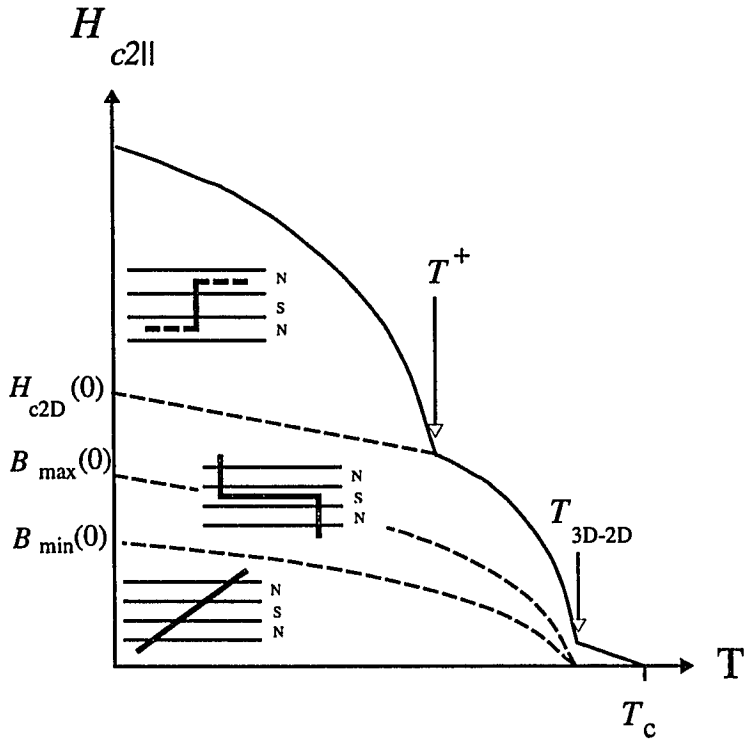

Figure 5.19. Our modified phase diagram for superconducting multilayers in near parallel magnetic fields (see Fig. 5.15.). B_{min} is the field which we choose to characterize the onset of the peak effect. There is, however, no sharp boundary between the anisotropic Abrikosov regime and the stepwise vortex lattice regime. B_{max} is the field at which the intrinsic pinning of the layers reaches its peak. Other quantities are as in Fig. 5.15.

Chapter 6. Conclusions

In this thesis, we have concerned ourselves with the superconducting properties of metallic multilayers composed of two superconductors, Nb and $Nb_{0.37}Ti_{0.63}$, primarily in magnetic fields oriented near parallel to the layers. The impetus for this work came from the desire to understand the physics governing vortex behavior in two-phase superconducting systems and with that knowledge to improve the performance of artificial pinning center wire.

6.1. Summary of Our Results

We have fabricated 11 period $Nb/Nb_{0.37}Ti_{0.63}$ multilayers with geometries analogous to those of APC wires [Motowidlo (92), Matsumoto (92)]. These materials [Obi (89), Karkut (88)] and geometries ($d_{NbTi} > \xi_{NbTi}, d_{Nb} < \xi_{Nb}$) [Aarts (90)] have not been closely examined for their basic superconducting properties. Their flux pinning properties have not been measured before our study. From our upper critical field measurements, we infer the first dimensional crossover (3D-to-2D) as temperature decreases below T_c of the pair potential $\Delta(r)$ predicted by Takahashi and Tachiki [86a] takes place for multilayers with d_{Nb} down to 4 nm. The second crossover (2D-to-3D) [Takahashi (86b)] may take place, but we have no unequivocal evidence for it. (Our multilayers are probably not anisotropic enough to observe the second crossover.) In our measurements of the critical currents, we have observed strong peak effects as a function of field (but not temperature), which occur in the range 0.2 to 0.5 H_{c2}. This type of peak effect in metallic multilayers has been seen by a number of others [Koorevaar (93), Nojima (93), Broussard (88), Raffy (81, 74b, 74a, 72)]. Their experimental evidence, as well as ours, points to the strong relationship between the peak effect and a change in configuration of the vortices

from an anisotropic Abrikosov lattice to a stepwise vortex lattice [Koorevaar (93), Tachiki (89b)].

We have extended and modified the understanding of the behavior of the vortex lattice in layered superconductors in two ways: by systematically measuring the peak pinning forces on the vortex lattice, we have shown that the pinning centers responsible for the peak effect in our MLs are the interfaces between the two superconductors [Takahashi (93), Stejic (93), Takahashi (89a), Mkrtchyan (73)]. Second, we propose a plausible mechanism which drives the crossover between vortex lattice configurations—the competition between the pinning energy and the elastic energy of the vortex lattice (specifically, the compression energy). Our simple model of this crossover provides semi-quantitative agreement with our data and makes clear the common physical link between peak effects observed in multilayers in near-parallel fields and those observed in other superconducting systems [Ling (91), Neerinck (91), Koorevaar (90), Wördenweber (90), Kes (81)]. All of these peak effects arise because of the competition between the vortex-pin and the vortex-vortex interactions and the onset of plastic deformation of the vortex lattice [Wördenweber (90), Larkin (79)].

6.2. Promise for APC

Among the original goals of this work was a determination whether thin film multilayers were a suitable model system to help guide wire makers in their quest for higher critical current densities. As we have seen, the behavior of superconducting MLs is quite complicated because of their quasi-2D nature: the dimensional crossover evidenced in the H_{c2} data and the peak effect in F_p, as well as the sheer magnitude of the pinning forces, are direct results of the strong periodicity along one dimension. For multilayers in near parallel fields, Nb remains superconducting to ~ H_{c2D} (which in our case may be a factor of 4 higher than the bulk H_{c2}) and $Nb_{0.37}Ti_{0.63}$ is the "pinner" layer for $B < H_{c2D}$. This is very different from the case of Nb island- and barrier-type APC conductors

[Cooley (93), Motowidlo (92), Motowidlo (90)], where the behavior of the Nb is bulk-like (H_{c2} ~ 1 T at 4.2 K). Because many APC wires do not have a strongly periodic layered structure, we must exercise caution when directly comparing ML results to wire results. However, Matsumoto and coworkers [94, 92] have produced APC wires made by stacking plates of Nb and NbTi inside a Cu tube—before the final draw, the microstructure of their single filaments looks very similar to that of a multilayer, though there is considerable disorder in the layering and the filaments are not aligned with each other. We believe our results on multilayers are most directly comparable to the results of Matsumoto *et al.* [92].

For a sample with a total filament width of 7.9 μm, d_{Nb} = 13.8 nm, and Λ = 27.7 nm, Matsumoto *et al.* obtained a maximum $F_p(B = 3\ \text{T}) = 22.2\ \text{GN/m}^3$. Because each filament in their wire is randomly oriented to the field, we must perform an angular average of our data to make a comparison. For sample [20/10], d_{Nb} = 10.4 nm, Λ = 30.5 nm, and the sample width = 4.50 μm. At $\theta = 5.4°$, $F_p(B_{max}) = 48.13\ \text{GN/m}^3$. To simplify this calculation, we assume that the pinning force density is given by Tachiki and Takahashi's [89b] result which describes the angular dependence of the pinning force on the vortex disks in the stepwise vortex lattice:

$$F_{avg} = \frac{2}{\pi}\int_0^{\pi/2} \frac{F_{p90°}}{\sqrt{\sin\theta}}d\theta = \frac{1}{\sqrt{\pi}}\frac{\Gamma(1/4)}{\Gamma(3/4)}F_{p90°} \approx 1.7F_{p90°} \approx 25\,GN/m^3, \qquad (6.1.)$$

where Γ is the gamma function. We have simply used our result at $\theta = 5.4°$ to estimate an appropriate $F_{p90°}$. The agreement between Matsumoto and coworkers' wire data and this estimate is surprisingly good. However, we have found (see Fig. 3.12. inset) that our $F_p(\theta)$ does not fall off as quickly as $1/\sin^{1/2}\theta$. The true angular average of our pinning force data for sample [20/10] is therefore higher, but no more than a factor of two. Our MLs may still be a good direct model system for their conductor.

Multilayers can still provide guidance for APC conductors that are not based on a layered approach; MLs can be used (with caution) to evaluate the pinning properties of specific materials (optimum dimensions, compositions, etc.) and their effect on H_{c2}. The peak effect data on $Nb_{0.37}Ti_{0.63}$/Ti in Appendix D shows that even "simple" superconductor/normal metal multilayers can have surprisingly complicated behavior.

The search for strong pinning boils down to the essential question: how can one maximize the effective volume of the pinning centers while not degrading the overall superconducting properties? The most straightforward approach to maximizing the pinning volume is to orient the pins along the direction of the field. This is the approach in multilayers and it has been shown to work for conventional heat-processed wire which was rolled to produce a flat tape [Cooley (91)]. However, this is not a generally useful solution because tapes and multilayers have strong pinning only in one direction—perpendicular to that direction, the pinning can be very weak [Cooley (91)]. The solution of Matsumoto and coworkers seems a good compromise, but it is by no means the only one. The other tack is to try to reproduce the conventional heat-processed NbTi microstructure (a high density of strong pinning material α-Ti [Meingast (89a)]) with improved materials and higher pinning volumes, which is essentially the island- and barrier-type APC approach. Very few materials and geometries have been successfully investigated and analyzed for use in APC conductors, and this is where multilayers might still be used to best effect.

Appendix A. Fabrication Schedule of Multilayers

A.1. Pre-Deposition

1) Clean 2" Si (100) wafer in TCA, acetone, and alcohol (methanol or isopropanol), 5 minutes each with ultrasonic agitation (US). DI rinse.

2) Start presputter: chamber Ar pressure 10 mTorr (conductance controller = 4.0, flow ~ 145 sccm), initial gun power 50 W DC or AC.

3) Ramp guns to full power (Nb: 100 W DC, NbTi: 300 W RF) at 50 W/minute (very conservative) and allow to equilibrate ~ 5 minutes. Keep STA 2 MAIN shutter closed (to prevent deposition on lamps), open individual gun shutters (to coat exposed surfaces with NbTi, a getter).

A.2. Deposition Rates

1) Load Si test piece with photoresist dots for liftoff/profilometry into load lock. Pump to 1 x 10^{-6} Torr. Close load lock cryo and open load lock to main chamber. Transfer to rotating arm. Rotate at ~ 30 rpm.

2) Deposit Nb 10 minutes at full power (100 W DC). Can turn down NbTi gun power to conserve target lifetime. Guns left on during entire predeposition (to avoid relighting).

3) Remove Si test piece from KJL, keep guns running with STA 2 MAIN closed.

4) Liftoff deposited film ~ 5 minutes in acetone US.

5) Measure deposited film thickness with DekTak 3030 profilometer. Average no less than 4 measurements.

6) Repeat 1) - 5) for NbTi

A.3. Multilayer Deposition

1) Set cycle timer to control Nb and NbTi gun shutters (Nb connected to pin #4, NbTi connected to #3). Measure actual times and adjust if necessary. To produce 10 period multilayer with buffer and cap layers, set output pulses = 6.

2) Load clean Si wafer onto rotating arm.

3) Turn on quartz lamp heater, TC #5 setpoint = 300 °C or TC #4 setpoint = 400 °C for true substrate T ≈ 255 °C. When heater PID parameters stable, turn on rotation ~ 30 rpm (before PID is stable, can blow main fuse by turning on rotation). Allow 15 minutes for substrate to come to temp. setpoint.

4) Ramp the guns to full power, if not there already. Open STA 2 MAIN.

5) Begin multilayer deposition: open Nb shutter and deposit 50 nm minus Nb layer thickness of buffer layer. Turn on cycle timer to start 11 cycles of Nb/NbTi.

6) Cycle timer leaves Nb shutter open at end of 11 cycles. When 50 nm cap layer has been deposited, close Nb shutter. Close STA 2 MAIN.

7) Ramp gun powers down to 50 W at 200 W/minute. Turn off guns. Turn off rotation. Shut off Ar gas flow. Open conductance controller. Turn off heater.

8) Remove sample to load lock. Cool for ~ 1.5 hours to near room temp.

A.4. Photolithography

If optical lithography mask JC1 is dirty:

1) Clean mask in TCA, acetone, methanol 5 minutes each. DI rinse.

2) Blow dry N_2.

Otherwise:

If multilayer sample has been outside KJL for more than a few hours:

1) Methanol or isopropanol rinse 1 minute. Spin dry.

2) Dehydration bake >100 °C for ~ 3 minutes

Otherwise:

3) Apply AZ 5218E. Wait 30 s (to promote adhesion). Spin at 4000 rpm 60 s. Resist thickness ~ 1.5 μm.

4) Bake on 90 °C hotplate 150 s.

5) Expose in hard contact mode 2.5 s (HTG mask aligner UV intensity ~ 9 mW/cm^2 at 365 nm).

6) Post exposure bake on hotplate 110 °C 90 s.

7) Flood exposure 52.5 s.

8) Develop in Microposit 351 developer mixed 1:5 with DI water ~ 20 s. Spin dry.

9) Hard bake 110 °C hotplate 5 minutes

A.5. Al Deposition and Liftoff

1) Start presputter: chamber Ar pressure 10 mTorr (conductance controller = 4.0, flow ~ 145 sccm), initial Al gun power 50 W DC.

2) Load patterned sample into load lock. Pump to 1 x 10^{-6} Torr. Close load lock cryo and open load lock to main chamber. Transfer to rotating arm. Transfer to J-arm.

3) Al gun power to 300 W DC ramped at 50 W/minute.

4) Swing J-arm over Al gun, open shutter to begin deposition of ~ 225 nm Al (1.5 min).

5) Close shutter. Gun power to 50 W at 200 W/minute. Gun off. Gas flow off.

6) Transfer sample to rotating arm, then to transfer arm, and into load lock.

7) Remove Al-coated wafer. Place in acetone ~ 30 minutes.

8) Use spray bottle of acetone to remove loose Al. Return to acetone ~ 1 hour.

9) Repeat 8) as necessary to produce 5-10 usable devices at a minimum.

10) DI rinse, spin dry.

A.6. Dicing

1) Spin AZ 1470 4000 rpm 60 s on device-side of wafer.

2) Mount on Tempress 601 dicing saw. Dice (cut depth ~ 0.005", speed = 10 Low, Si blade from Assembly Technologies). Break into individual chips.

3) Rinse chips in acetone, methanol, DI 1 minute each

A.7. Reactive Ion Etching

1) Pumpdown Cooke CV-300 to 1 x 10^{-5} Torr with O_2, SF_6, and manifold valves open.

2) Close SF_6 valve. Open capacitance manometer. O_2 preclean belljar: 10 mTorr, ~ 10 sccm, - 400 V_{dc}, ~ 50 W RF (regulate V_{dc}, not power), 5 minutes. Tuner positions: target = 5, J-load ~ 43, input tune ~ 11 o'clock. Close O_2 valve.

3) Open SF_6 valve. SF_6 preclean (not necessary as a cleaning, but needed to adjust tuning network, etc.): 4 mTorr, ~ 13 sccm, -250 V_{dc}, ~ 60 W RF, 5 minutes. Tuner positions:

target = 5, J-load ~ 35, input tune ~ 3 o'clock. Close SF_6 valve. Close manifold valve. Close capacitance manometer.

4) Vent belljar (N_2). Load chips midway between center and edge of electrode while venting.

5) Pump down to 1 x 10^{-5} Torr with SF_6 and manifold valves open.

6) Open cap. man. SF_6 etch, same parameters as 2). Typical etch time ~ 3 minutes. Shut off SF_6 flow. Close valves. Close cap. man.

7) Vent belljar. Check samples visually and with ohmmeter to ensure bare substrate exposed. If not fully etched, repeat from 4). Otherwise: rough pump belljar. Close off pumps.

A.8. Al Wet Etch

1) Paint AZ 1470 on contact pads with artist's brush.

2) Bake on hotplate 110 °C 5 minutes

3) Etch 225 nm Al in PAE ~ 20 minutes.

4) DI rinse 2 minutes, blow dry N_2.

Appendix B. Sample Parameters

Table B.1. Multilayer Properties[a]

Sample	Name	d_{Nb} (nm)	d_{NbTi} (nm)	Width (μm)	T_c (K)	$\xi_{90°}(0)$ (nm)	$\xi_{5°}(0)$ (nm)	$T_{3D\text{-}2D}$ (K)	$H_{c2D}(0)$ (T)
94-3-1	[20/4]	4.0	20.1	0.95	8.52	3.6	3.7	8.02	11.7
93-31-1	[21/6]	5.7	20.6	3.28	8.51	3.8	4.5	8.08	9.8
93-32-1	[21/8]	7.7	20.8	3.24	8.65	4.1	4.7	8.10	9.2
94-6B-1	[20/10]	10.4	20.1	4.50	9.10	n/a	4.6	8.65	8.8
94-7-1	[14/9]	9.0	14.2	4.33	8.41	n/a	5.3	7.43	9.8
94-8-1	[27/9]	8.8	26.9	4.92	8.65	n/a	5.3	b	b

[a] 94-5 was made explicitly for XRD characterization: 11 Λ 7 nm Nb/4 nm Ti w/ 5 nm Nb buffer and cap. Sample [10/19] (d_{NbTi} = 9.7 nm, d_{Nb} = 18.9 nm) was also characterized by XRD

[b] showed weak 3D-to-2D crossover

Table B.2. Single Film Properties

Sample	Name	thick (nm)	Width (μm)	T_c (K)	$H_{c2}(0)$ (T)	$\xi_{90°}(0)$ (nm)	κ	ρ_n (μΩcm)	RRR
93-26-2	NbTi	200	5.75	8.48	19	3.6	55	73.7	1.2
93-28-5	Nb	220	9.00	9.21	2.0	12.3	5.6	10.1	6.2

See chapters 3, 4, and 5 for more data and for details of measurements and calculations.

Appendix C. Temperature Correction

In our measurements of the critical temperatures, we found significant offsets from the expected values when the worm gear mechanism was connected to the sample stage (see Fig. 3.6.). This was the configuration for almost all our measurements, because we needed to control the sample orientation in the magnetic field. In particular, for measurements on our 200 nm thick Nb film, we found T_C = 9.8 K, which is well above the value for bulk Nb (T_C = 9.3 K) and the value of T_C of Nb films (9.2 K) produced under similar conditions [Kuwasawa (90)]. Subsequent measurements of bulk Nb standards (from Johnson-Mathey) and other Nb films produced at Yale [Gaidis (94)] showed this offset. Our measurements of T_C were reproducible and nonhysteretic. The thermometer calibration was checked a number of times over the course of this thesis: when immersed in a liquid He bath, it read the correct temperature.

The source of this offset is the cryostat design: no thermal isolation was provided between the Cu sample stage and the worm gear mechanism, which is stainless steel; in addition, the sample and thermometer are not thermally shorted to one another (see Fig. 3.6.). The thermometer and heater are both mounted on the same massive Cu block; the sample is connected to this block through its leads (which are wrapped near the leads for the thermometer) and the mechanical link between the Cu block and the Cu sample stage axle. A schematic of the thermal pathways at the bottom of the cryostat is presented in Fig. C.1. As a result, the sample stage and the thermometer are *not* at the same temperature because there is more cooling power to the sample than to the thermometer. The absolute difference between the thermometer temperature and the sample temperature decreases as the heater power is reduced. An electrical analog of this situation is illustrated schematically in Fig. C.2.

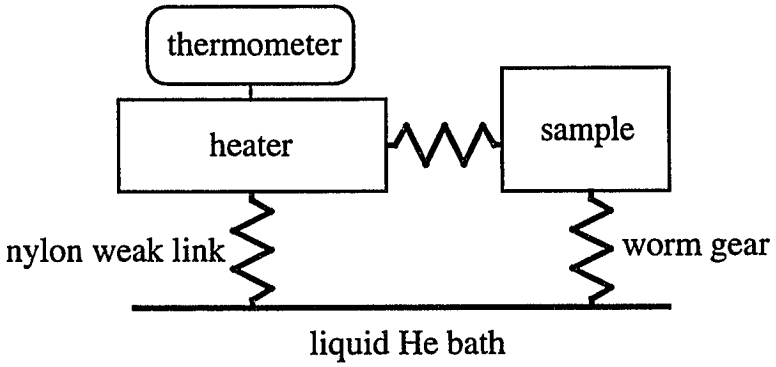

Figure C.1. Schematic of the thermal paths in our measurement of the sample temperature. The thermometer and heater are in close thermal contact with each other, but the sample is not in strong contact with them. There is also a path to the He bath through the worm gear mechanism.

We corrected our sample temperatures to account for the offset induced by the cooling through the worm gear. At liquid He temperature (4.2 K), the thermometer read 4.2 K. At the T_C of our Nb films (9.2 K), the thermometer read 9.8 K. These two points define the linear correction to the measured sample temperature above 4.2 K.

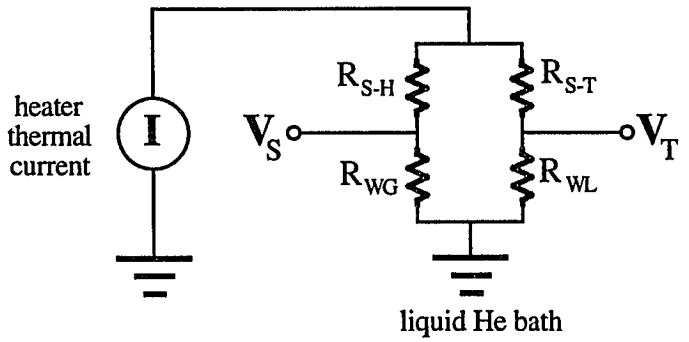

Figure C.2. Electrical analog of sample cooling. The heater power is represented as a thermal current. The temperature offset between the sample and thermometer is $\Delta T \equiv \Delta V = V_S - V_T$. There are thermal resistances between the sample and heater (R_{S-H}) and the sample and the thermometer (R_{S-T}). The heat paths from the sample to the liquid helium bath are through the worm gear (R_{WG}) and the nylon weak link (R_{WL}). If $R_{WG} = \infty$, then $\Delta T \equiv \Delta V = 0$ in equilibrium. If R_{WG} finite, then $\Delta T \neq 0$.

Appendix D. $Nb_{0.37}Ti_{0.63}$/Ti Multilayers

In the main, this thesis has been concerned with the influence of the multilayer structure on its pinning properties. A parameter which is equally important to the flux pinning properties is the choice of material that composes the multilayer itself; we made a number of $Nb_{0.37}Ti_{0.63}$/Ti multilayers with geometries similar to the $Nb_{0.37}Ti_{0.63}$/Nb MLs that we have studied in detail in Chapters 4 and 5. There geometries are summarized in Table D.1. Because of time constraints, only two $Nb_{0.37}Ti_{0.63}$/Ti samples were measured. Sam Hess measured $J_C(B)$ at 4.2 K and $H_{C2}(T)$ for samples 94-10 (21 nm $Nb_{0.37}Ti_{0.63}$/9 nm Ti) and 95-1 (19 nm $Nb_{0.37}Ti_{0.63}$/5 nm Ti). Nick Rizzo was kind enough to measure the angular dependence of J_C near $\theta = 0°$ for sample 95-1. Similarly to the $Nb_{0.37}Ti_{0.63}$/Nb samples, we will refer to our $Nb_{0.37}Ti_{0.63}$/Ti MLs by their layer thicknesses, surrounded by curly brackets. For example, sample 95-1 is {19/5}. Additionally, Dr. Dan Dietderich of LBL took TEM images of a $Nb_{0.37}Ti_{0.63}$/Ti sample deposited at room temperature. The data, while not complete, provide information important to the understanding of flux pinning in multilayers and APC wires.

Table D.1. $Nb_{0.37}Ti_{0.63}$/Ti multilayer parameters[a]

Sample	Name	d_{Ti} (nm)	d_{NbTi} (nm)	Width (μm)
94-9	Ti film	168	n/a	n/a
94-10	{21/9}	9.0	20.6	4.46
95-1	{19/5}	5.2	19.4	3.55
95-2	{20/13}	12.8	19.5	n/a
95-4	{20/9}	9.1	20.1	n/a

[a] 94-3 was made explicitly for TEM characterization: 11 Λ 20 nm NbTi/13 nm Ti w/ 50 nm Ti buffer and cap, deposited at ambient temperature.

D.1. Fabrication and Measurement

The fabrication methods for the $Nb_{0.37}Ti_{0.63}$/Ti MLs were kept as close as possible to those for the $Nb_{0.37}Ti_{0.63}$/Nb MLs (Chapter 3) to facilitate intercomparison. The Ti (99.99% pure Cu-backed target) was sputtered at the standard 10 mTorr at 200 W RF power from the gun at position D (see Fig. 3.1.) We achieved an average deposition rate of 0.11(3) nm/s. Every other parameter of the fabrication, from cleaning of the substrates to mounting in the cryostat, was nominally identical to those described in Chapter 3 and Appendix A. Likewise, the procedures for measuring J_C and T_C were nominally identical to those used for the $Nb_{0.37}Ti_{0.63}$/Nb samples.

Dr. Dan Dietderich of LBL took TEM images (see Ch. 3.6.3) of sample 95-3, a 19 nm $Nb_{0.37}Ti_{0.63}$/13 nm Ti multilayer which was deposited at room temperature (to minimize possible interdiffusion between the layers). As with the images of the $Nb_{0.37}Ti_{0.63}$/Nb samples, the direct measurement of the multilayer period (31.8 nm) is in excellent agreement with the inferred period from deposition rates (32.3 nm).

D. 2. Basic Superconducting Properties

The upper critical fields for $\theta = 5.4°$ of the two samples measured show the well-known 3D-to-2D dimensional crossover of the superconducting order parameter ψ in anisotropic layered superconductors [Obi (87), Takahashi (86a), Kanoda (85), Banerjee (84, 82), Ruggiero (82), Klemm (75)]. We have discussed this effect in Ch. 4.2.2. In this case, however, we have a superconductor/normal ML, not a dirty/clean superconductor ML as in $Nb_{0.37}Ti_{0.63}$/Nb. It is important to note this distinction, since the detailed behavior of the order parameter (hence the vortices) is very different in the two systems: in $Nb_{0.37}Ti_{0.63}$/Nb MLs, ψ may nucleate in either Nb or $Nb_{0.37}Ti_{0.63}$, since both are true superconductors; in $Nb_{0.37}Ti_{0.63}$/Ti, ψ may only nucleate in the $Nb_{0.37}Ti_{0.63}$, since Ti is nonsuperconducting (though subject to the proximity effect). We plot $H_{c2}(5.4°, T)$ of

{19/5} and {21/9} in Fig. D.1., along with the upper critical field of a thick (200 nm) film of $Nb_{0.37}Ti_{0.63}$ for comparison. We see that there is some suppression of the upper critical field compared to $Nb_{0.37}Ti_{0.63}$ at higher temperatures, but that the three curves meet near 6.5 K. We have also plotted a fit to Eq. 4.11. (quasi-2D behavior) for each of the multilayers. As with our $Nb_{0.37}Ti_{0.63}$/Nb MLs, the dimensional crossover takes place for $\xi(T_{3D\text{-}2D}) \sim 0.6\ \Lambda$. In Table D.2. we summarize the various superconducting parameters extracted from the data in Fig. D.1.

Table D.2. Superconducting properties of $Nb_{0.37}Ti_{0.63}$/Ti multilayers, $H_{c2}(5.4°)$.

Sample	T_c (K)	$-\left.\frac{dH_{c2}}{dT}\right\|_{T_c}$	$\xi_{GL}(0)$ (nm)	$T_{3D\text{-}2D}$ (K)	$H_{c2D}(0)$ (T)
94-10 {21/9}	7.89(5)	3.14(9)	3.6(2)	7.63(3)	13.26(41)
95-1 {19/5}	7.97(5)	3.12(15)	3.6(2)	7.57(3)	12.87(30)

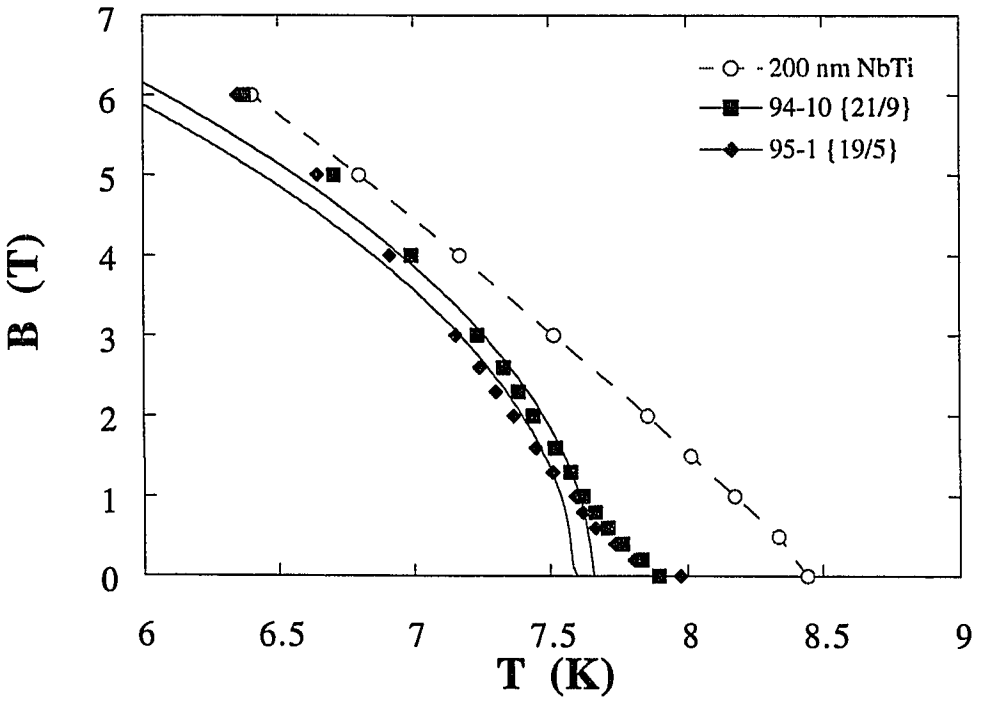

Figure D.1. $H_{c2}(T)$ at $\theta = 5.4°$ for $Nb_{0.37}Ti_{0.63}$/Ti multilayers {21/9} and {19/5} and a 200 nm thick film of $Nb_{0.37}Ti_{0.63}$. Also plotted are fits to the quasi-2D regions of the multilayer data.

D.3. Flux Pinning

The peak effect in $Nb_{0.37}Ti_{0.63}$/Nb MLs was described in Chapter 5. One of the conclusions that we drew from our analysis of the stepwise vortex lattice was that the peak in the pinning strength at intermediate fields would only be seen in a multilayer that was entirely superconducting, that is, strongly-coupled. We would not expect a system composed of weakly-coupled superconducting layers to have strong pinning—the vortex segments in the superconducting layers (known as vortex disks or pancakes [Koshelev (93), Clem (91), Tachiki (89b)]) are coupled to one another only by Josephson currents or, in the most anisotropic case, the interaction between their individual magnetic dipole moments. Since these interactions are weak, the pinning forces in the system would arise primarily from the extrinsic centers, such as grain boundaries. In a strongly-coupled system, the existence of a true vortex between the strongly superconducting layers allows the strong intrinsic pinning of the layers themselves to play the dominant role in determining the pinning behavior.

D.3.1. The Peak Effect and the Role of Coupling

It is therefore somewhat surprising that $Nb_{0.37}Ti_{0.63}$/Ti sample {19/5} exhibits a peak effect similar to that seen in the $Nb_{0.37}Ti_{0.63}$/Nb MLs. Naively, we would not have expected the proximity effect coupling between $Nb_{0.37}Ti_{0.63}$ layers through Ti to be so strong. However, recent theoretical work by Gurevich and Cooley [94] indicates that it is possible to sustain a vortex structure (albeit highly modified) across a nonsuperconducting "defect" in the case of strong Josephson coupling. They point out that bulk NbTi with thin α-Ti ribbons (with length scales comparable to our MLs) satisfies the requirements for such a system.

In Fig. D.2.a. we plot $J_C(5.4°, 4.2\ K, B)$ for sample {19/5} and it's closest $Nb_{0.37}Ti_{0.63}$/Nb analog, [21/6]. Except at low fields, the critical current density of {19/5}

is *higher* than that of [21/6]. In Fig. D.2.b. we plot the same quantity for {21/9} and [20/10]. Sample {21/9} shows no indication of a peak effect and its critical current density is lower than that of both {19/5} and [20/10]. The corresponding values of the pinning force density are plotted in Fig. D.3.a. and D.3.b. We have also indicated the characteristic fields B_{min} and B_{max} for {19/5} in Fig. D.3.a. Note that {19/5} has some additional structure in $J_C(B)$ before B_{min}, perhaps a secondary peak, though this feature is not evident in the plot of $F_p(B)$.

Stejic [93] presented calculations of the maximum elementary pinning force density per unit length f_L of both NbTi/Nb and NbTi/Ti layered structures (see Ch. 5.2.1.1.). His analysis predicts a higher elementary pinning force for Ti layers, as compared to Nb layers of the same thickness (see also Ch. 2.5.2.). Using Stejic's model, we find that the ratio of the maximum elementary pinning force density ($\approx$ Fp in this case) for sample {19/5} to [21/6] is ~ 2.5. The actual ratio of $F_p(B_{max})$ is 1.3, though at higher fields the ratio approaches 2. However, Stejic's model also predicts that the elementary pinning force should increase as d_{Ti} increases towards ~ 2 ξ_{NbTi} and then reach a plateau [Matsushita (83)]. Sample {21/9} (d_{Ti} ~ 2 ξ_{NbTi}) has a relatively low F_p compared to {19/5} or either of the $Nb_{0.37}Ti_{0.63}$/Nb samples, in contradiction of the model.

What is neglected in Stejic's model is the effect the exponential decay of proximity coupling with d_{Ti} [deGennes (64)] has on the vortex lattice. As the Josephson coupling drops exponentially, a point is reached when a vortex can no longer be maintained across the Ti layer [Gurevich (94)]—the vortices which spanned the sample become vortex disks in the NbTi layers, which are coupled only weakly [Clem (91)]. The total pinning force density in the pancake vortex lattice is smaller than that in the stepwise vortex lattice because all that impedes disk motion is extrinsic pinning—the intrinsic pinning is no longer involved. The proximity effect length K [deGennes (64)]

(which determines the exponential decay of the coupling) in Ti may be as short as 10 nm at 4.2 K, depending on the mean free path. With such a short K, the NbTi layers would quickly become decoupled with increasing d_{Ti}.

If we take the effects of decoupling into account, we can fit the data on samples {19/5} and {21/6} into the larger picture of the peak effect in anisotropic superconducting systems detailed in Chapter 5. For thin enough normal metal layers, such that the superconducting layers are strongly coupled [Gurevich (94)], the crossover between the anisotropic Abrikosov vortex lattice and the Stepwise Vortex lattice may take place [Koorevaar (93), Nojima (93)], as in {19/5}; as long as a true vortex structure can be maintained through the entire sample, the strong intrinsic pinning of the layers may play a part. Once the superconducting layers are not strongly coupled (which happens rapidly for short mean free path normal metals), vortices are no longer sustained between the superconducting layers—the intrinsic pinning is no longer effectual and the peak effect disappears, as in {21/9}. Without more samples and extensive measurements of $Nb_{0.37}Ti_{0.63}$/Ti MLs, we cannot make more quantitative explanations.

In the absense of layering and its attendent effects on the vortex lattice, it seems that Ti (with dimensions of order the coherence length in NbTi) is a better choice to obtain strong pinning at high fields than Nb. However, it is not clear that the strong reduction of T_C by the proximity effect will not offset the higher pinning forces obtainable with Ti. A more complete study of the flux pinning properties of the $Nb_{0.37}Ti_{0.63}$/Ti system is warranted.

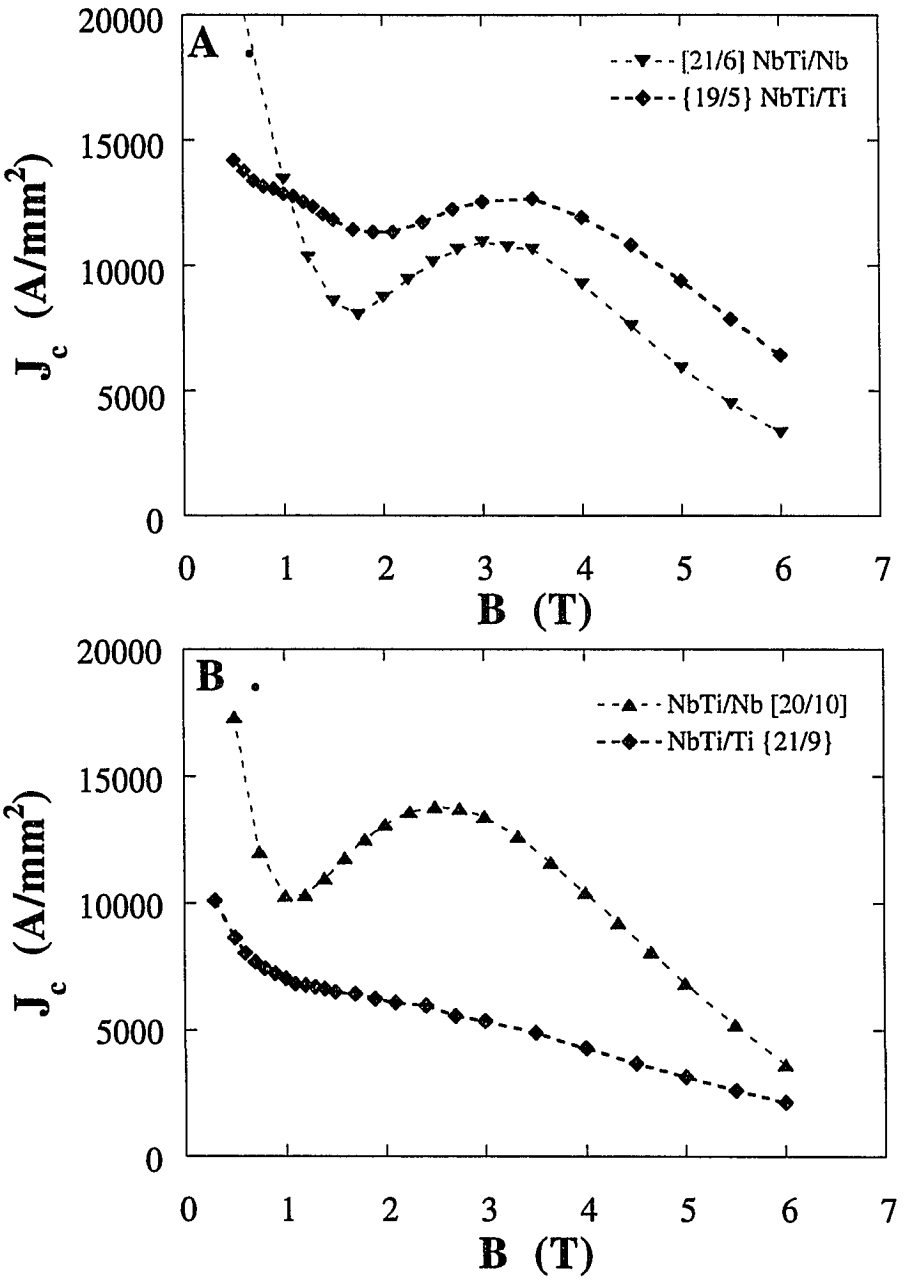

Figure D.2. J_C(5.4°, 4.2 K, B) for $Nb_{0.37}Ti_{0.63}$/Ti and $Nb_{0.37}Ti_{0.63}$/Nb multilayers. A) Samples [21/6] and {19/5}. B) Samples [20/10] and {21/9}. Note that the magnitude of the peak effect in $Nb_{0.37}Ti_{0.63}$/Nb samples is more pronounced with larger d_{Nb}, but in $Nb_{0.37}Ti_{0.63}$/Ti disappears with larger d_{Ti}.

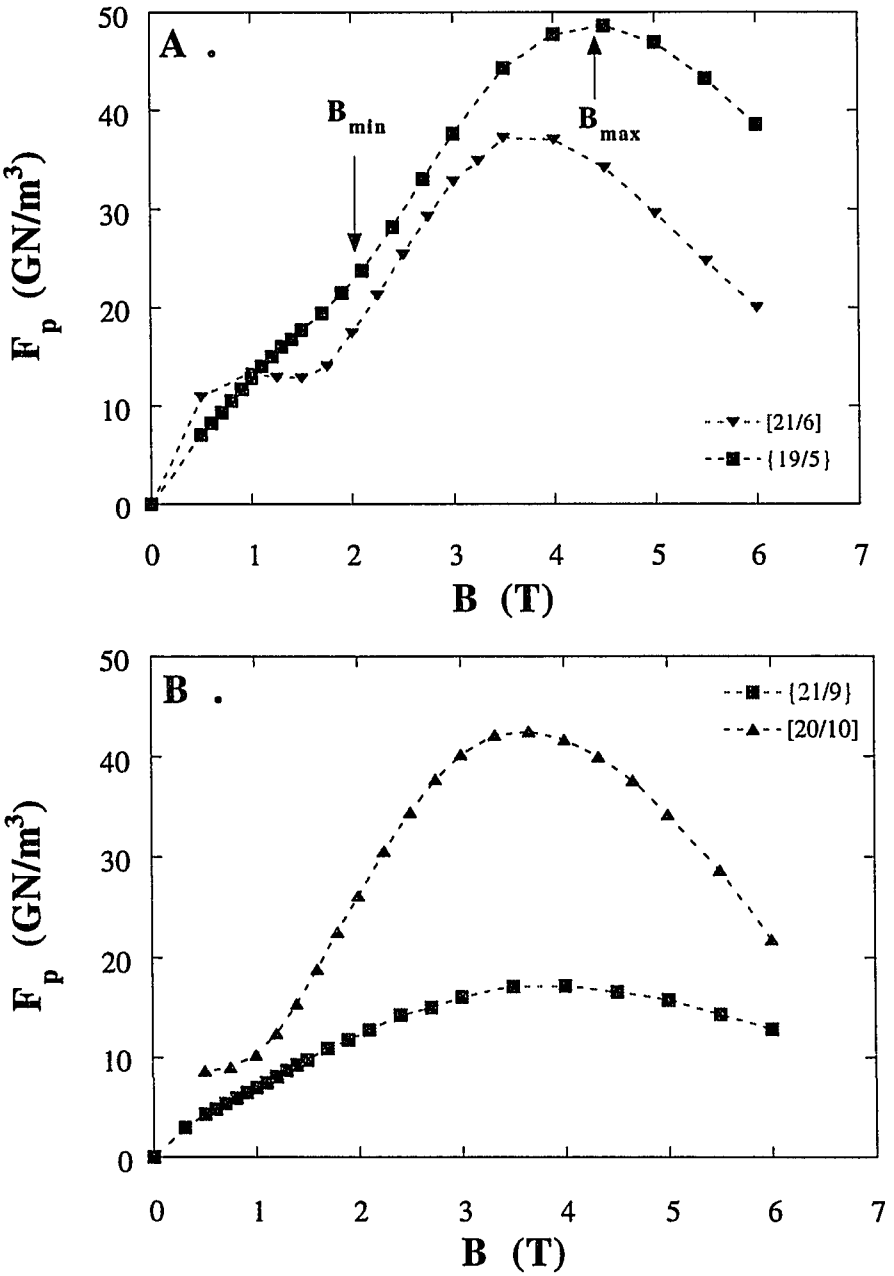

Figure D.3. F_p(5.4°, 4.2 K, B) for $Nb_{0.37}Ti_{0.63}$/Ti and $Nb_{0.37}Ti_{0.63}$/Nb multilayers. A) Samples [21/6] and {19/5}. B) Samples [20/10] and {21/9}. The characteristic fields are indicated for sample {19/5}. {21/9} shows no indication of a peak effect.

D.3.2. Angular Dependence of J_c Near $\theta = 0°$

As a complement to the measurements of the angular dependence of the critical current density of $Nb_{0.37}Ti_{0.63}$/Nb MLs (see Fig. 3.12.), we also measured it for sample {19/5}. In Fig. D.4. we plot $J_c(\theta)$ at 4.2 K and 5 T for {19/5} and [21/6]. Using the data for {19/5}, we estimate the uncertainty in critcal current density ΔJ_c caused by uncertainties in the angle θ to be ~ 10%, which is comparable to the estimate using the data for [21/6] (see Ch. 3.5.1.1.). The data were obtained by setting the stage at some large arbitrary angle away from parallel and rotating through the peak at 0°. The stage was then rotated back in the direction of its original position. The "flattening" of the curves away from the peak may be due in part to the effect of mechanical backlash in the worm gear mechanism: the stage may not be rotating as much per turn of the screw (see Fig. 3.6.) near the points where the direction of motion was reversed (near ± 15°).

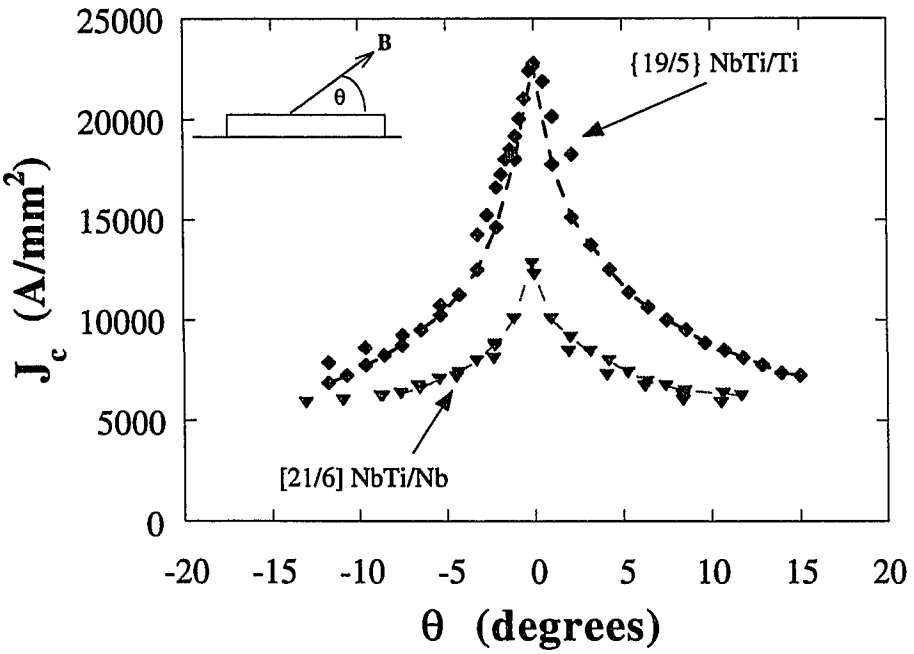

Figure D.4. $J_c(\theta)$ for θ near parallel at 4.2 K and 5 T for {19/5} and [21/6]. Data have been shifted so that the maximum of J_c occurs at $\theta = 0°$.

References

Aarts, J., K.-J. de Korver, and P. H. Kes, "Dimensionality crossovers in the parallel critical fields of $Nb/Nb_{0.6}Zr_{0.4}$ multilayers," Europhys. Lett., vol. 12, pp. 447-452, 1990.

Abrikosov, A. A., "On the magnetic properties of superconductors of the second group," Sov. Phys. JETP, vol. 5, pp. 1174-1182, 1957.

Ahuja, R. and H. L. Fraser, "Structure and mechanical properties of nanolaminated Ti-Al thin films," J. of Metals, pp. 35-39, Oct. 1994.

Amos, R. S., P. E. Breyer, H. H. Huang, and A. W. Lichtenberger, "Stress and source conditions of DC magnetron sputtered Nb films," to appear in IEEE Trans. Appl. Supercond., vol. 5, 1995.

Anderson, W. R., D. R. Lombardi, R. G. Wheeler, and T. -P. Ma, "Determination of Si/SiO_2 interface roughness using weak localization," IEEE Elec. Dev. Lett., vol. 14, pp. 351-353, 1993.

Ashcroft, N. W. and N. D. Mermin, *Solid State Physics*, (Holt, Rinehart and Winston, Inc., Orlando, FL), pp. 826, 1976

Ashkin, M. and J. R. Gavaler, "The upper critical field of NbN film," J. Appl. Phys., vol. 49, pp. 2449-2451, 1978.

Ashkin, M., J. R. Gavaler, J. J. Greggi, and M. DeCroux, "The upper critical field of NbN films. II.," J. Appl. Phys., vol. 55, pp. 1044-1048, 1984.

Autler, S. H., E. S. Rosenblum, and K. H. Gooen, "High field superconductivity in Nb," Phys. Rev. Lett., vol. 9, pp. 489-493, 1962.

Banerjee, I., "Superconductivity in Nb/Cu Superlattices," Northwestern University thesis, unpublished, 1982.

Banerjee, I. and I. K. Schuller, "Transition temperature and critical fields of Nb/Cu superlattices," J. Low Temp. Phys., vol. 54, pp. 501-518, 1984.

Bardeen, J., L. N. Cooper, and J. R. Schrieffer, "Theory of superconductivity," Phys. Rev., vol. 108, pp. 1175-1204, 1957.

Beasley, M. R., in *Inhomogeneous Superconductors*, ed. D. V. Gubser, T. L. Francavilla, J. R. Leibowitz, and S. A. Wolf (AIP, New York), pp. 186, 1980.

Bouchier, D., G. Gautherin, B. Agius, and S. Rigo, "Investigation of ion-beam-sputtered Nb-Ti thin films by complementary use of backscattering and nuclear-reaction microanalysis," J. Appl. Phys., vol. 49, pp. 5896-5902, 1978.

Brandt, E. H. "Elastic energy of the vortex state in type II superconductors. II. Low inductions," J. Low Temp. Phys., vol. 5/6, pp. 735-753, 1977b.

Brandt, E. H. "Range and strength of pins collectively interacting with the flux-line lattice in type-II superconductors," Phys. Rev. Lett., vol. 57, pp. 1347-1350, 1986a.

Brandt, E. H. "Elastic and plastic properties of the flux-line lattice in type-II superconductors," Phys. Rev. B, vol. 34, pp. 6514-6517, 1986b.

Broussard, P. R., and T. H. Geballe, "Critical fields of Nb-Ta multilayers," Phys. Rev. B, vol. 35, pp. 1664-1668, 1987.

Campbell, A. M. and J. E. Evetts, Adv. Phys., vol. 21, pp. 1191, 1972.

Chapman, B., *Glow Discharge Processes* (John Wiley & Sons, New York, pp. 406), 1980.

Chen, B., "Plasma processes for VLSI pattern transfer," Yale University thesis, unpublished, 1990.

Chen, J. H., "Proximity effect in zero field with the Landau-Ginzburg equation. II," Phys. Rev. B, vol. 42, pp. 3957-3959, 1990.

Clem, J. R., "Two-dimensional vortices in a stack of thin superconducting films: a model for high-temperature superconducting multilayers," Phys. Rev. B, vol. 43, pp. 7837-7846, 1991.

Collings, E. W., *A Sourcebook of Titanium Alloy Superconductivity* (Plenum Press, New York), pp. 216-313, 1983.

Collings, E. W., *Applied Superconductivity, Metallurgy, and Physics of Titanium Alloys* (2 volumes, Plenum Press, New York), 1986.

Cooley, L. D., "The scaling rule and fluxon core pinning in a high field superconductor with artificially introduced pins," Ph.D. thesis, University of Wisconsin-Madison, unpublished, 1993.

deGennes, P. G., "Boundary effects in superconductors," Rev. Mod. Phys., vol. 36, pp. 225-237, 1964.

deSorbo, W., "The peak effect in substitutional and interstitial solid solutions of high field superconductors," Rev. Mod. Phys., vol. 36, pp. 90-94, 1964.

Dorofejev, G. L. *et al.*, "Current-carrying capacity of superconductors with artificial pinning centers," *Proceedings of the 9th International Conference on Magnet Technology*, ed. C. Marinucci and P. Weymuth (Swiss Institute for Nuclear Research, Switzerland), pp. 564-566, 1985.

Edgecumbe, J., L. G. Rosner, and D. E. Anderson, "Preparation and properties of thin-film hard superconductors," J. Appl. Phys., vol. 35, pp. 2198-2202, 1964.

Ekin, J. E., J. Appl. Phys., vol. 49, p. 3406, 1978.

Face, D. W., "Quantum limited detection and noise in superconducting tunnel junction mixers," Yale University thesis, unpublished, 1987.

Fantner, E. J., Appl. Phys. Lett., vol. 47, p. 803, 1985.

Feigel'man, M. V., V. B. Geshkenbein, A. I. Larkin, and V. M. Vinokur, "Theory of collective creep," Phys. Rev. Lett., vol. 63, pp. 2303-2306, 1989.

Fischer, R. A., *The Design of Experiments*, (Oliver and Boyd, London, pp. 236), 1942.

Fujii, Y. *et al.*, J. Phys. Soc. Japan, vol. 55, p. 251, 1986.

Gaidis, M. C., "Superconducting Tunnel Junctions as Single Photon X-Ray Detectors," Yale University thesis, unpublished, 1994.

Ginzburg, V. L. and L. D. Landau, Zh. Eksperim. i Teor. Fiz., vol. 20, p. 1064, 1950.

Gor'kov, L. P., "Microscopic derivation of the Ginzburg-Landau equations in the theory of superconductivity," Zh. Eksperim. i Teor. Fiz., vol. 36, pp. 1918-1923, 1959. (English translation: Sov. Phys. JETP, vol. 36, pp. 1364-1367, 1959.)

Gor'kov, L. P., "Theory of superconducting alloys in a strong magnetic field near the critical temperature," Zh. Eksperim. i Teor. Fiz., vol. 37, pp. 1407-1416, 1959. (English translation: Sov. Phys. JETP, vol. 37, pp. 998-1004, 1960.)

Gurevich, A. and L. D. Cooley, "Anisotropic flux pinning in a network of planar defects," Phys. Rev. B, vol. 50, pp. 13 563-13 576, 1994.

Hirsch, P., A. Howie, R. Nicholson, D. W. Pashley, and M. J. Whelan, *Electron Microscopy of Thin Crystals* (Robt. E. Krieger Publishing Co., Malabar, FL), pp. 563, 1977.

Y. Iye, "Anisotropic transport properties of high T_C oxides," Int. J. Mod. Phys., vol. 3, pp. 367-388, 1989.

Jin, B. Y. *et al.*, "Superconducting properties fo layered $Nb_{0.53}Ti_{0.47}$/Ge structures prepared by dc sputtering," J. Appl. Phys., vol. 53, p. 2443-2549, 1985.

Jin, B. Y. and J. B. Ketterson, "Artificial metallic superlattices," Adv. in Phys., vol. 38, pp. 191-366, 1989.

Karkut, M. G. *et al.*, "Anomalous upper critical fields of superconducting multilayers: verification of the Takahashi-Tachiki effect," Phys. Rev. Lett., vol. 60, pp. 1751-1754, 1988.

Kes, P. H. and C. C. Tsuei, "Two-dimensional collective flux pinning, defects, and structural relaxation in amorphous superconducting films," Phys. Rev. B, vol. 28, pp. 5126-5139, 1983.

Klemm, R. A., A. Luther, and M. R. Beasley, "Theory of the upper critical field in layered superconductors," Phys. Rev. B, vol. 12, pp. 877-891, 1975.

Klepper, S. J., "Sensitivity of Quantum Electron Conductance to Elastic Scatterers and to Spin-Orbit Scattering in Gallium Arsenide Heterostructures," Yale University thesis, unpublished, 1991.

Kogan, V. G. and L. J. Campbell, "Elastic properties of flux lattices in anisotropic high-T_c superconductors," Phys. Rev. Lett., vol. 62, pp. 1552-1555, 1989.

Koorevaar, P., W. Maj, P. H. Kes, and J. Aarts, "Vortex-lattice transition in superconducting NbZr/Nb multilayers," Phys. Rev. B, vol. 47, pp. 934-943, 1993.

Kramer, E. J. and H. C. Freyhardt, "The proximity effect in flux pinning," J. Appl. Phys., vol. 51, pp. 4930-4938, 1980.

Kumar, D., M. G. Blamire, A. M. Campbell, "Critical current of high-quality NbTa thin films and heterostructures," Physica B, vol. 194-196, pp. 1855-1856, 1994

Kuroda, K. and M. Yuda, "Niobium-stress influence on Nb/Al-oxide/Nb Josephson junctions," J. Appl. Phys., vol. 45, pp. 387-396, 1977.

Kuwasawa, Y., U. Hayano, T. Tosaka, S. Nakano, and S. Matuda, "Observation of anomalous transition in the upper critical fields of Nb/$Nb_{0.5}Zr_{0.5}$ multilayers," Physica C, vol. 165, pp. 173-178, 1990.

Kwok, W. W. *et al.*, "Direct observation of intrinsic pinning by layered structure in single-crystal $YBa_2Cu_3O_{7-\delta}$," Phys. Rev. Lett., vol. 67, pp. 390-393, 1991.

Labusch, R. "Calculation of the critical field gradient in type II superconductors," Cryst. Lattice Defects, vol. 1, pp. 1-16, 1969.

Larbalestier, D. C., and A. W. West, Acta Metall., vol. 32, p. 1871, 1984

Larbalestier, D. C. and M. P. Maley, "Conductors from superconductors: low-temperature and new high-temperature superconducting conductors," MRS Bulletin, pp. 50-56, August 1993.

Larkin, A. I. and Yu. N. Ovchinnikov, "Flux pinning in type II superconductors," J. Low Temp. Phys., vol. 34, pp. 409-428, 1979.

Lawrence, W. and S. Doniach, in *Proceedings of the Twelfth International Conference on Low Temperature Physics*, (ed. E. Kanda, Academic Press of Japan, Kyoto), p. 361, 1971.

Ling, X. S. and J. I. Budnick, "A.C. susceptability studies of type-II superconductors: vortex dynamics," in *Magnetic Susceptability of Superconductors and Other Spin Systems*, (ed. R. A. Hein *et al.*, Plenum Press, New York), pp. 377-388, 1991.

Ling, X. S. *et al.*, "Fluctuation effects on a strongly pinned vortex lattice in a thin type-II superconducting wire," Phys. Rev. Lett., vol. 74, pp. 805-808, 1995.

Lowe, W. P. and T. H. Geballe, "NbZr multilayers. I. Structure and superconductivity," Phys. Rev. B, vol. 29, pp. 4961-4968, 1984.

Maj, W. and J. Aarts, "Outer layers determine the parallel critical field of a superconducting multilayer," Phys. Rev. B, vol. 44, pp. 7745-7748, 1991.

Matsumoto, K. *et al.*, "Flux pinning characteristics of Nb artificial pins with ribbon-shape in Nb-46.5 wt% Ti superconductors," Supercond. Sci. Tech., vol. 5, pp. 684-689, 1992.

Matsumoto, K. *et al.*, "Enhanced Jc properties in superconducting NbTi composites by introducing Nb artificial pins with a layered structure," Appl. Phys. Lett., vol. 64, pp. 115-117, 1994.

Matsushita, T., "Elementary pinning force of normal precipitates in a superconductor," J. Appl. Phys., vol. 54, pp. 281-288, 1983.

McCambridge, J. D., *et al.*, "Flux pinning in NbTi/Nb multilayers," to appear in IEEE Trans. Appl. Supercond., 1995.

Meingast, C., M. Daeumling, P. J. Lee, and D. C. Larbalestier, "Proximity effect reduction of the critical temperature in two-phase Nb-Ti superconductors," Appl. Phys. Lett., vol. 51, pp. 688-689, 1987.

Meingast, C., P. J. Lee, and D. C. Larbalestier, "Quantitative description of a high J_c NbTi superconductor during its final optimization strain: I. Microstructure, T_c, H_{c2}, and resistivity," J. Appl. Phys., vol. 66, pp. 5962-5970, 1989a.

Meingast, C. and D. C. Larbalestier, "Quantitative description of a very high critical current density Nb-Ti superconductor during its final optimization strain. II. Flux pinning mechanisms," J. Appl. Phys., vol. 66, pp. 5971-5983, 1989b.

Mkrtchyan, F. B., E. A. Shakirzyanova, E. A. Shapoval, and V. V. Shmidt, "Interaction between a vortex and the boundary between two superconductors," Zh. Eksp. Teor. Fiz., vol. 63, pp. 667-669, 1972. (Sov. Phys. JETP, vol. 36, pp. 352-353, 1973).

Moffat, D. L., Ph.D. thesis, University of Wisconsin-Madison, unpublished, 1985.

Motowidlo, L. R., B. A. Zeitlin, M. S. Walker, and P. Haldar, "Multifilament NbTi with artificial pinning centers: the effect of alloy and pin material on the superconducting properties," Appl. Phys. Lett., vol. 61, pp. 991-993, 1992.

Muller, R. S. and T. I. Kamins, *Device Electronics for Integrated Circuits*, (John Wiley and Sons, New York, pp. 324), 1986.

Mullock, S. J. and J. E. Evetts, "Collective flux pinning in a defective flux vortex lattice," J. Appl. Phys., vol. 57, pp. 2588-2592, 1985.

Neerinck, D. *et al.*, "Transition in the flux lattice of artificially layered superconductors," Phys. Rev. Lett., vol. 67, pp. 2577-2580, 1991.

Nojima, T., M. Kinoshita, S. Nakano, and Y. Kuwasawa, "Transport critical current density and dimensional crossover in superconducting NbZr/Nb multilayers," Physica C, vol. 206, pp. 387-392, 1993.

Obi, Y., M. Ikebe, Y. Muto, and H. Fujimori, "Upper critical fields of NbTi based multilayered materials," Jap. J. Appl. Phys., vol. 26-3, pp. 1445-1446, 1987.

Qian, Y. J., J. Q. Zheng, B. K. Sarma, H. Q. Yang, J. B. Ketterson, and J. E. Hilliard, "Critical field measurements in Nb-Ti composition-modulated alloys," J. Low Temp. Phys., vol. 3/4, pp. 279-294, 1982.

Raffy, H., J. C. Renard, and E. Guyon, "Critical currents and pinning effect in superconducting alloy films spatially modulated in concentration," Sol. State Comm., vol. 11, pp. 1679-1682, 1972

Raffy, H., E. Guyon, et J. C. Renard, "Courants critiques d'alliages supraconducteurs de concentration modulee spatialement I—effet de la periode," Solid State Comm., vol. 14, pp. 427-429, 1974a.

Raffy, H., E. Guyon, et J. C. Renard, "Courants critiques d'alliages supraconducteurs a concentration modulee spatialement II—effet de la temperature," Solid State Comm., vol. 14, pp. 431-433, 1974b.

Raffy, H. and E. Guyon, "Dependence of critical current and field of periodically modulated superconducting alloys on modulation amplitude," Physica, vol. 108B, pp. 947-948, 1981.

Rugar, D. and P. Hansma, "Atomic force microscopy," Phys. Today, pp. 23-29, Oct. 1990.

Ruggiero, S. T., T. W. Barbee, Jr., and M. R. Beasley, "Superconductivity in quasi-two-dimensional layered composites," Phys. Rev. Lett., vol. 45, pp. 1299, 1980.

Ruggiero, S. T., "Layered Superconducting Composites," Stanford University thesis, unpublished, 1981.

Ruggiero, S. T., T. W. Barbee, Jr., and M. R. Beasley, "Superconducting properties of Nb/Ge metal semiconductor multilayers," Phys. Rev. B., vol. 26, pp. 4894-4908, 1982.

Saint-James, D. and P. G. deGennes, "Onset of superconductivity in decreasing fields," Phys. Lett., vol. 7, pp. 306-308, 1963.

Shapira, Y. and L. J. Neuringer, "Upper critical fields of Nb-Ti alloys—evidence for the influence of Pauli paramagnetism," Phys. Rev. A, vol. 140, pp. 1638-1644, 1965.

Spitzer, H. J., "Preparation and superconducting properties of thin films of some binary transition metal alloy systems," J. Vac. Sci. Tech., vol. 8, pp. 184-187, 1971.

Steinberg, R. N., "Synthesis and Characterization of Yttrium-Barium-Copper-Oxide Thin Films," Yale University thesis, unpublished, 1992.

Stejic, G., L. D. Cooley, R. Joynt, D. C. Larbalestier, and S. Takacs, "Numerical calculation of flux pinning by α-Ti precipitates in Nb-Ti," Supercond. Sci. Tech., vol. 5, pp. S97, 1992.

Stejic, G., "The mean-field flux pinning theory," University of Wisconsin-Madison thesis, unpublished, 1993.

Stejic, G. *et al.*, "Effect of geometry on the critical currents of thin films," Phys. Rev. B, vol. 49, pp. 1274-1288, 1994.

Sudbø, A. and E. H. Brandt, "Flux-line tilt moduli in anisotropic superconductors," Phys. Rev. Lett., vol. 66, pp. 1781-1784, 1991.

Tachiki, M. and S. Takahashi, "Strong vortex pinning mechanism in high-T_c oxide superconductors," Sol. State Comm., vol. 70, pp. 291-295, 1989a.

Tachiki, M. and S. Takahashi, "Anisotropy of critical current in layered oxide superconductors," Sol. State Comm., vol. 72, pp. 1083-1086, 1989b.

Tachiki, M., S. Takahashi, and K. Sunaga, "Driving and pinning forces acting on vortices in layered superconductors," Phys. Rev. B., vol. 47, pp. 6095-6105, 1993.

Taillard, R., J. Foct, C. E. Bruzek, and Hoang-Gia-Ky, "Mechanisms of formation of intermetallic compounds at the interfaces of niobium-shielded filaments," IEEE Trans. Appl. Supercond., vol. 3, pp. 1346-1349, 1993.

Takahashi, S. and M. Tachiki, "Theory of the upper critical field of superconducting superlattices," Phys. Rev. B, vol. 33, pp. 4620-4631, 1986a.

Takahashi, S. and M. Tachiki, "New phase diagram in superconducting superlattices," Phys. Rev. B, vol. 34, pp. 3162-3164, 1986b.

Tinkham, M., *Introduction to Superconductivity* (Robt. E. Krieger Publishing, Malabar, FL), pp. 296, 1980.

Thuneberg, E. V., J. Kurkijärvi, and D. Rainer, "Pinning of a vortex line to a small defect in superconductors," Phys. Rev. Lett., vol. 48, pp. 1853-1856, 1982.

Thuneberg, E. V., J. Kurkijärvi, and D. Rainer, "Elementary-flux-pinning potential in type-II superconductors," Phys. Rev. B, vol. 29, pp. 3913-3923, 1984.

Van Duzer, T. and C. W. Turner, *Principles of Superconductive Devices and Circuits* (Elsevier North Holland, Inc., NY), pp. 369, 1981.

Werthamer, N. R., "Theory of the superconducting transition temperature and energy gap function of superposed metal films," Phys. Rev., vol. 132, pp. 2440-2445, 1963.

Werthamer, N. R., E. Helfand, and P. C. Hohenberg, "Temperature and purity dependence of the superconducting critical field, H_{c2}. III. Electron spin and spin-orbit effects," Phys. Rev., vol. 147, pp. 295-302, 1966.

White, W. R., A. Kapitulnik, and M. R. Beasley, "Model system for vortex motion in coupled two-dimensional type-II superconductors," Phys. Rev. Lett., vol. 66, pp. 2826-2829, 1991.

Wickramasinghe, H. K., "Scanned-probe microscopies," Sci. Am., pp. 98-105, Oct. 1989.

Wördenweber, R. and P. H. Kes, "Dimensional crossover in flux pinning," Phys. Rev. B, vol. 34, pp. 494-497, 1986.